Probing Light-Matter Interactions between Plasmonic Nanoantennas and Single Emitters: Polarization and Localization

by

Tiancheng Zuo

A dissertation submitted in partial fulfillment
of the requirements for the degree of
Doctor of Philosophy
(Chemistry)
at the University of Michigan
2020

Doctoral Committee:

Associate Professor Julie S. Biteen, Chair
Professor Steven Cundiff
Professor Theodore Goodson III
Professor Nils Walter

Tiancheng Zuo

curlyzuo@umich.edu

ORCID iD: 0000-0003-1278-1820

I would like to dedicate this Thesis to my late grandfathers: Weimin Lin and Zongliang Zuo, who passed away during the final year of my PhD journey.

ACKNOWLEDGEMENTS

The work presented in thesis would have been impossible without the help and support from many people.

First of all, I would like to thank my advisor Professor Julie Biteen. I have learned so much from Professor Biteen both in science and in leadership. Thank you for always believing in me. Thank you for your consistent patience in mentoring me through out the 5 years. I really appreciate and look up to your dedication and professionalism. I would also like to thank my wonderful lab members for making the office feel like home. I specially thank Ben Isaacoff and Steven Lee who were not only my mentors but my close friends. I also want to thank Josh and Hannah for bringing so much laughter to the lab.

This thesis is a result of a series of collaborations. I specially thank my collaborators Harrison Goldwyn and Professor David Masiello. Thank you for all the insightful conversations we had. I want to thank my mentee Kaitlyn who shows great enthusiasm and dedication towards science.

I thank all my friends who have brought so much pleasant and joy to my PhD journey. Especially, I want to thank Chengcheng, Junqi, Junjie, Shiba, Nhat, April, Hannah, Ricardo, Sarah, Mohan and Max. Being far away from home, you guys were like family to me.

Finally, I would never gotten here without the support from my family. I can't say thank you enough to my parents Wen Zuo and Lan Lin, who taught me how to be a good person and supported me to pursue my dream in the United States. Wherever I go, I know you guys are always there with me. I can not express how blessed I am to have the companionship of my partner Jane. Thank you for always being by my side.

TABLE OF CONTENTS

LIST OF FIGURES

Figure

LIST OF ABBREVIATIONS

EBL electron-beam lithography

EMCCD electron multiplying charge-coupled device

FDTD finite difference time domain

LSPR localized surface plasmon resonance

LSP localized surface plasmon

NA numerical aperture

PAINT points accumulation for imaging in nanoscale topography

PALM photoactivated localization microscopy

PSF point spread function

SEM scanning electron microscope

SOFI super-resolution optical fluctuation imaging

SPP surface plasmon polariton

STORM stochastic optical reconstruction microscopy

dSTORM direct stochastic optical reconstruction microscopy

GSD ground state depletion microscopy

SPP surface plasmon polaritons

PBD polarizing beam displacer

ABSTRACT

Single-molecule super-resolution imaging enables optical microscopy to study features of nanometer size. It has been widely used in bioimaging. Plasmonic nanoantennas couple the far field to the near field by converting propagating waves to localized fields. Plasmonic nanoantennas enhance applications from biosensing to light-emitting devices and Raman spectroscopy. Combining single-molecule imaging and plasmonic nanoantennas not only enables plasmon enhanced super-resolution imaging but also provides a unique method to study the light-matter interaction between single molecules and plasmonic nanoantennas. In this thesis, I focus on studying the emission coupling between single emitters and plasmonic particles. Chapter I details the background of single-molecule fluorescence imaging, some fundamental physics behind plasmonic nanoantennas and some nanofabrication techniques used in this thesis. In Chapter II, I discuss my application of single-molecule polarization resolved microscopy to study the emission polarization change of isolated fluorescent emitters with different colors upon coupling to gold nanorods. With the support of simulations, I show that the emission polarization from the coupled system rotates toward the direction of the dominant nanoantenna-localized surface plasmon mode. I also present a reduced-order analytical model that was informed by my experiments to explain the emission polarization modification. The model attributes this emission polarization distribution to both far-field interference and resonant coupling between the molecular dipole and the nanorod plasmon modes.

To study emission localization modification (the mislocalization effect), in Chapter III, I use the super-resolution imaging method of direct stochastic optical reconstruction mi-

croscopy (dSTORM) to image the coupling of single emitters to gold nanodisks. I demonstrate that mislocalization is the result of fluorescence emission coupling, whereas fluorescence enhancement is the result of both absorption and emission coupling. I also discuss how the analytical model is developed further to recover the orientation and localization of a single emitter in the simulation. I show that this model fitting outperforms the standard Gaussian fitting significantly.

In addition to the study of organic fluorescent molecules, I use quantum dots (semiconductor nanocrystals, QDs) for super-resolution imaging in Chapter IV. I present the methods that I developed to adapt our organic dye experiments for QDs. I discuss the possibility of using QDs and silver nanoparticles to achieve plasmon enhanced fluorescence without emission coupling. I also characterize by two-channel single-molecule hyperspectral imaging to the spectral shift (bluing) of single QDs upon photooxidation and I discuss how a proximal gold nanoparticle affects the bluing.

Lastly, in Chapter V, I present a relevant future direction for doing single-QD imaging with aluminum nanoparticles. It provides a possible approach to achieving plasmon enhanced super-resolution imaging with reduced mislocalization.

The work presented in this thesis improves our understanding of the light-matter interactions between plasmonic nanoantennas and single emitters. It also advances the application of plasmon enhanced super-resolution microscopy.

CHAPTER I

Introduction

1.1 Fluorescence

[1]Fluorescence occurs pretty commonly in our daily life. It has been widely used as a readout for bioimaging and sensing. It enables people to see the structures of biological systems, to observe biological activities and to unveil biological mechanisms. Besides fluorescence emission intensity, many other things can be used as fluorescence readouts, such as emission polarization, emission color (spectrum), and emission direction. However, it is not fully understood how the fluorescence emission is changed by coupling to plasmonic nanoantennas. In this thesis I use single-molecule and single-particle experiments to understand how an optical nanoantenna, which concentrates the local field thus affecting fluorescence. To help explain how plasmonic nanoantennas affect fluorescence, I will start with some underlying principles of fluorescence.

1.1.1 Fluorescence excitation and emission

Molecules that display fluorescence, such as large conjugated aromatic molecules, quantum dots etc., are called fluorophores. Quinine, often used to impart bitterness to tonic water, is a common fluorophore. The earliest observation of quinine fluorescing in

[1]Sec. 1.3 is from Zuo, Goldwyn *et al.* [1] and the first draft was written by my co-author Harrison Goldwyn.

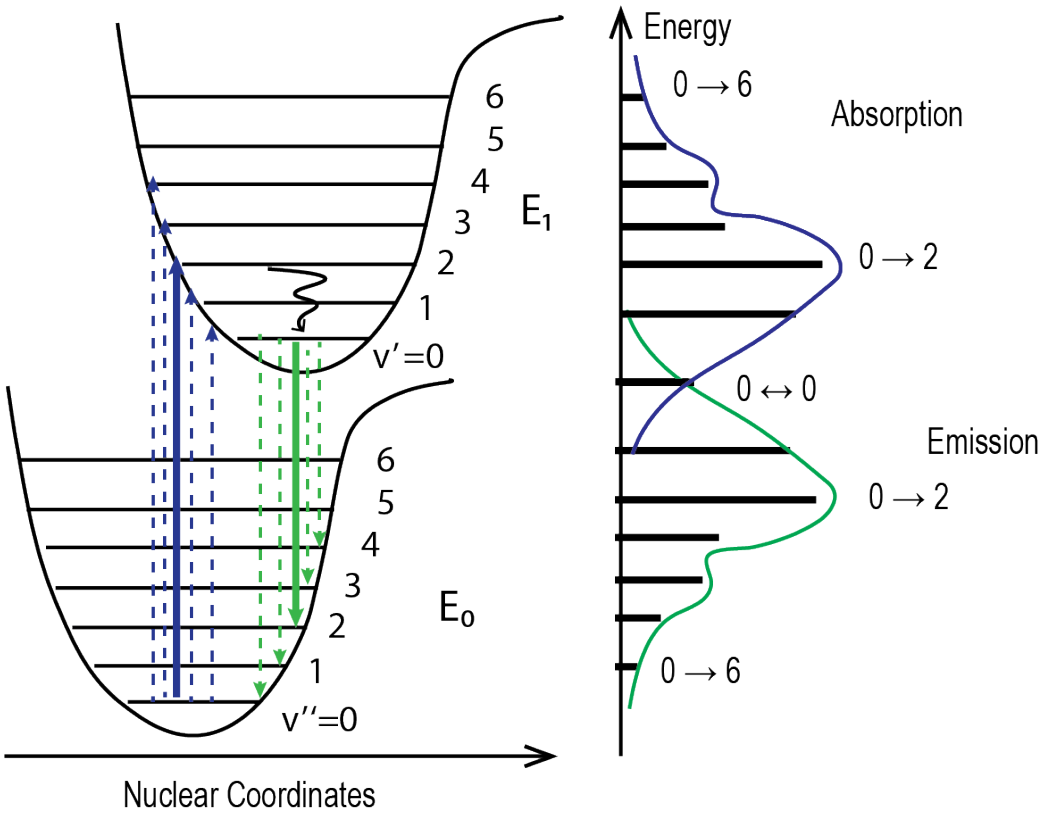

Figure 1.1: **Energy diagram and absorption and emission spectra.** The left side is the Frank-Condon principle energy diagram. Blue arrows indicate absorption from the lowest level in the ground electronic state E_0 to the vibrational energy level in the excited state E_1. The green arrows denote the decay from the lowest level in the excited state to the ground state. The right shift of shape between E_0 and E_1 shows the change in nuclear positions. The right side of this figure is the schematic representation of the absorption and emission spectra corresponding to the energy diagram on the left, showed by blue and green curves respectively. Courtesy of Kena-Cohen [3].

solution was reported by Sir John Frederick in 1845 [2]. To understand how fluorophores such as quinine can glow, let's take a look at a simplified Franck-Condon principle energy diagram (Fig. 1.1). The Frank-Condon principle is a rule in quantum chemistry to describe the intensities of vibronic transitions. Upon excitation of the molecule, if the incident energy matches the difference between the vibronic energy levels between the ground and the excited electronic states, the electron will be excited to the excited states (blue arrows in Fig. 1.1). Then, according to Kasha's rule (black curly arrow in Fig. 1.1), the molecule will thermally relax to the lowest level of excited electronic state. Finally it decays back to

the ground electronic states via photon emission (green arrows in Fig. 1.1). Because of this non-radiative relaxation from higher vibrational levels to the lowest level in the excited states and because of the Franck-Condon principle, the electron excitation happens much faster than the timescale of a nuclear vibration, the emission energy will be lower than the absorption energy. This energy shift is shown on the right side in Fig. 1.1, showed by blue and green curves respectively. This shift between the absorption and emission spectra is also called the Stokes Shift. The distribution in the spectra is due to the probabilities of the different transitions. Electronic transitions occur on a much smaller time scale than the nuclear motions, i.e. electrons get excited/decay much faster than bonds can vibrate. Thus, according to the Franck-Condon principle, change between vibrational energy levels is more likely when the nuclear positions of the two levels are the same. In this figure, for example, transitions between $v' = 0$ and $v" = 2$ (solid blue and green arrows) are favored over the other possible transitions and therefore the intensities of those transitions are the highest. The symmetry between the absorption and emission spectra is due to the similar shape of the ground and excited states. The narrow black line spectrum can only be observed in the gas phase. The curved spectra that we get in the solution is due inhomogeneous broadening resulting from the interaction of electrons with the phonons in the liquid [2, 4].

1.1.2 Fluorescence anisotropy

In the previous section, I talked about the process of fluorescence in terms of energy level transitions. Here, I will have discuss the molecular rotational movement during absorption and emission. Molecular rotation changes the emission polarization. The change of polarization in the emission is described as fluorescence anisotropy. Fluorescence anisotropy is important because it is caused not only by the rotational motion of the molecules but also by coupling to optical nanoantennas, which will be introduced in Chapter II.

Aromatic fluorophores, which have a certain preferred direction of electron oscillations (i.e., a permanent dipole moment) depending on the molecular structure, can be treated as a radiating dipole upon excitation. Ground state molecules are randomly oriented in a homogeneous solution. If polarized light is used to excite the molecules, the sub-population of the molecules that align with the incident light is more likely to be excited. Hence, the orientation distribution of excited state molecules will peak at the orientation of the incident light. The lifetime of the excited state is around 5-10 nanoseconds allowing many forms of depolarization before the molecules decay back to ground state such as rotational diffusion. The dependence of anisotropy on molecule motions has led to numerous applications in biochemical research such as studying the viscosity of the solutions or measuring the binding constants of reactions [5,6]. In the next chapter, I will discuss how I apply fluorescence anisotropy as a readout to the study of the interaction between fluorophores and optical nanoantenna.

To quantify fluorescence anisotropy, let's now consider a molecule (radiating dipole) in the Cartesian coordinate system as shown in Fig. 1.2 with incident light polarized parallel

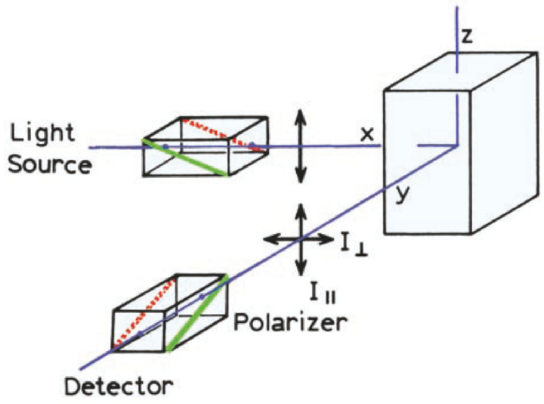

Figure 1.2: **Fluorescence anisotropy measurement [5].** The two boxes with red and green lines are polarizers. The black arrows show polarization of the light. When the polarizer at the emission side is also parallel to incident light, the detected fluorescent intensity is called I_p. Conversely, when the polarizer is perpendicular to the incident light, the intensity detected is denoted as I_s. Copyright ©Springer Science

to the z-axis. When the polarizer at the emission side is also parallel to incident light, the detected fluorescent intensity is called I_p. Conversely, when the polarizer is perpendicular to the incident light, the intensity is denoted as I_s. So in Fig. 1.2, $I_p = I_z$ and $I_s = I_x$. If we assume the dipole has z-axis symmetry then $I_s = I_y$. Anisotropy can be defined as:

$$r = \frac{I_p - I_s}{I_p + 2I_s} \tag{1.1}$$

The denominator term represents the total energy which is the sum of I_x, I_y and I_z. With z-axis symmetry, it can be rewritten to $I_p + 2I_s$.

1.2 Microscopy techniques

Microscopy is a widely used technique for imaging. Depending on the wavelength of the electromagnetic spectrum used for imaging, two common types of microscopy are optical and electron microscopy. Another big category is scanning probe microscopy which includes atomic force microscopy and scanning tunneling microscopy. Fluorescence which occurs in the visible range of electromagnetic spectrum has been used heavily on optical microscopy to generate better contrast and resolution. In this thesis, I use an optical microscope to understand the interaction between fluorescence emitters and optical antennas. I will go in depth into the fundamentals of optical microscopy in this section.

1.2.1 Optical microscopy

In order to see any features in a sample, contrast needs to be created during illumination or upon emission. Depending on the methods to introduce contrast, common methods include to bright field illumination, dark-field illumination, polarized light illumination and phase contrast illumination.

Bright field illumination is used in the upright microscopes Fig. 1.3. Sample illumina-

tion is through transmitted (green line in Fig. 1.3) or reflected white light (yellow light in Fig. 1.3). Depending on the samples, it sometimes creates relatively low contrast due the fact that the background light is also being collected in the same time as the signal.

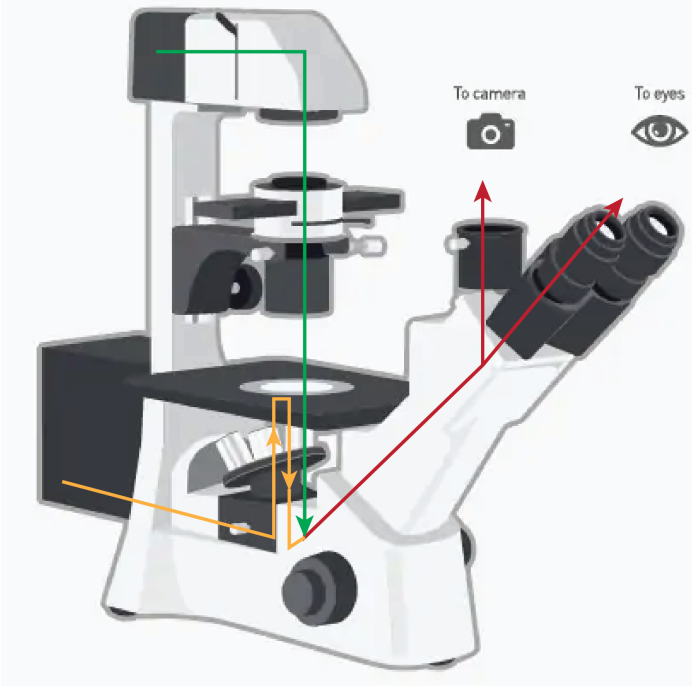

Figure 1.3: **Upright microscope.** A cartoon of a upright microscope. Green and yellow lines are the transmitted and reflected light path respectively. Red line shows the common light path the light goes through. Copyright ©ThermoFisher

Dark-field illumination setup is similar to transmitted bright field illumination, except that the direct light is blocked when it passes through dark-field condenser before it hits the sample plane. At the place where there is no sample present, the incident light comes across the sample plane at large angles and misses the low numerical aperture (NA) objective. This large angle illumination is introduced by a dark-field condenser. Only the light scattered by the sample is collected by the objective. Dark-field illumination is often used in inverted microscopes with light illuminating from the top then collected by the objective after. This largely reduced background enables us to characterize less absorbing features such as scattering of nanoparticles which will be mentioned in the later chapters.

Polarized light illumination is also similar to bright field illumination expect that the

incident white light is polarized instead of unpolarized light. Contrast is created when features have preference in reflecting light with different polarizations. There are other more complex techniques that take advantage of polarization such as differential interference contrast microscopy [7]. Differential interference contrast microscopy is widely used in single particle tracking in cells [8, 9] as it is highly selective and noninvasive.

Lastly, phase contrast illumination is a common technique we use in our lab. This technique differentiates between structures by exploiting the difference in the refractive index of different parts in the sample even when there is no difference in absorption. This simple technique can be easily realized in bright field illumination inverted microscope by adding a phase condenser and a phase objective. These two pieces together introduces a phase shift between the light direct from the light source and the light scattered by the sample. Thus, phase contrast microscopy is great for imaging colorless/transparent samples and it is commonly to be used in bio labs for imaging whole cells.

Consider using a microscope to image a light emitting point source. When light passes through an aperture in the objective, due to the diffraction of the light [10], it will appear as a diffracted pattern rather than an infinitly small point on the image plane. The image has the functional form of an Airy disk. We also call it a point spread function (PSF) because it is the image of a point convolved with the microscope optics (Fig. 1.4a) [11]. The resolving power between two PSFs is often described by the Abbe diffraction limit which is defined as

$$d = \frac{\lambda}{2NA} \tag{1.2}$$

where λ is the emission light wavelength and NA is the numerical aperture of the objective which is a dimensionless number defines the range of angles over which the light can pass through an objective. For example, if the optical microscope emits light with wavelength λ=600 nm and has an objective with NA=1, then the resolving power for this microscope is 300 nm. In other words, two PSFs are considered resolvable in this microscope, if the distance between them is smaller than 300 nm.

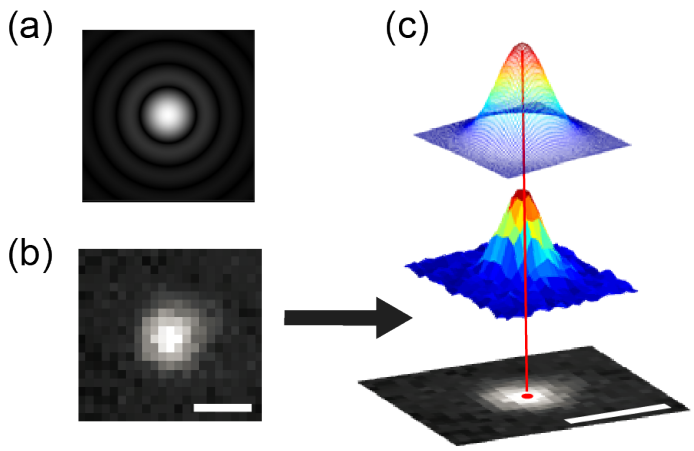

Figure 1.4: **Airy disk and Gaussian fitting**(a) 2D view of a Airy disk. (b) Grey scale image of single emitter seen on a camera. (c) The intensity profile of (b) is fit to a 2D Gaussian to more precisely locate the center. The scale bars in (b) and (c) are 500 nm. (c) adapted from Tuson *et al.* [12].

1.2.2 Single-molecule fluorescence microscopy and super-resolution imaging

As I mentioned in the end of last section, the resolution of a typical optical microscope is around 300 nm. Unfortunately, most of the biological objects in the cell are smaller than that scale which makes it difficult to use conventional optical microscope to observe biological systems especially the activities inside the cells. In this section, I will talk about how I can combine fluorescence with optical microscopy to achieve super-resolution imaging.

Combining fluorescence with optical microscopy is another way to further largely reduce the background noise and increase contrast. As we discussed in Sec. 1.1, fluorescent emission has lower energy than the absorption (Stokes shift). Therefore, we can filter out the incident light, leaving only the fluorescent light coming from the sample to be collected by the detectors with right filters at emission end of the microscope. A proper single wavelength light source such as laser is needed to excite the sample which contains certain fluorophores. In this fashion, the background noise introduced by the incident light is largely reduced. Having a low-background (high-contrast) technique enables singe-molecule detection. Therefore one can detect the movement of a single protein inside a cell with fluorescent labels. In the past two decades, many microscopy techniques

have been applied to single-molecule imaging. These techniques are but not limited to: epifluorescence microscopy [13], confocal microscopy [14], total internal reflection fluorescence microscopy [13], highly inclined and laminated optical sheet [15], two-photon excitation microscopy [16], light sheet fluorescence microscopy [17, 18], tilted light sheet microscopy [19], dual-objective microscopy [20] and cryogenic fluorescence microscopy [21, 22].

The images obtained from those techniques are still diffraction limited. In order to obtain sub-diffraction limited images, data processing methods need to be introduced. Knowing that the PSF of a single emitter is well approximated by a Gaussian function, we can then fit the PSF to a 2D Gaussian model to more precisely locate the center (Fig. 1.4c). This PSF fitting enables us to localize molecules with ~30 nm precision which is around 10 times below diffraction limit. The more photons we collect, the better resolution we can achieve [23]. PSF engineering has taken this fitting to the next step in recent years. PSF engineering is a new technique using meta lenses to change the shape of a PSF in order to obtain information more than just the in-plane position. The double-helix point spread function [24] for example, encodes the 3D position information of a single emitter in a 2D epifluorescence image.

In order to use the PSF fitting technique to locate single molecules, we must ensure that under each diffraction-limited spot, there is only one molecule emitting at a time. These super-resolution approaches include: points accumulation for imaging in nanoscale topography (PAINT) [25], stochastic optical reconstruction microscopy (STORM) [26], direct stochastic optical reconstruction microscopy (dSTORM) [27], photoactivated localization microscopy (PALM) [28, 29], ground state depletion microscopy (GSD) [30], super-resolution optical fluctuation imaging (SOFI) [31] and so on. They combine with the microscopy techniques mentioned above to ultimately achieve super resolution imaging. PAINT and dSTORM are the ones used in my research which will be introduced Chapter II and III respectively.

Due to the great achievements mentioned above and so many others, optical microscopy can now achieve nanometer scale resolution. To honor this work, the 2014 Nobel Prize in Chemistry was awarded to Eric Betzig, Stefan W. Hell and William E. Morener who independently pioneered different techniques for super-resolved fluorescence microscopy.

1.3 Plasmonic nanoantenna

[2]Let's now switch gears to talk about the plasmonic nanoantenna, another important part of my thesis. Plasmonics entails the study and application of plasmons, the oscillation of free electrons in conductors. Antennas have been described by Novotny and coworkers:

> is a device designed to efficiently convert free-propagating optical radiation to localized energy, and *vice versa* [32].

plasmonic nanoantennas are nm-scale antennas made from plasmonic nanoparticles [32–40]. Plasmonic nanoantennas can be used to enhance the fluorescence intensity of single emitters [41–43]. As I mentioned in Sec. 1.2.2, the localization precision in single molecule imaging is inversely proportional to the totally number of collected photons. Therefore, plasmonic nanoantennas can increase the resolution by enhancing the fluorescence. However, the way plasmonic nanoantenna alters fluorescence is not fully understood. In this thesis, Goldwyn and I create an analytical model to explain and predict coupling between the antenna and fluorescence in order to understand the interaction better and make it a good candidate for enhancing fluorescent imaging.

In this section, I will briefly explain some fundamental equations behind plasmonic particles, serving as a foundation for the analytical model which will be introduced in Chapter II and Chapter III.

[2]This section is from Zuo, Goldwyn *et al.* [1] and the first draft was written by my co-author Harrison Goldwyn.

1.3.1 Drude model of the metal permittivity

The permittivity or dielectric function $\epsilon(\omega)$ encodes the material's inherent frequency dependent optical response. The simplest model for $\epsilon(\omega)$ of a metal is related to Paul Drude's 1900 model of electrical conduction. Here, we follow the derivation in Jackson [44] that starts with a more general model for an insulating material. In this case the optically active electrons are considered bound, but we will later free each electron from its respective nucleus to model the conduction electrons in a metal.

We start by describing the classical motion of a single electron with charge $-e$ and mass m harmonically bound to some atomic nucleus and under influence of an external electric field $\mathbf{E}$.

$$m[\ddot{\mathbf{x}} + \gamma\dot{\mathbf{x}}] = -e\mathbf{E}e^{-i\omega t}, \tag{1.3}$$

where γ quantifies the phenomenological damping which may be due to radiation, electron-nuclear scattering, or electron-electron scattering , ω is the frequency of external light field and $\mathbf{x}$ is the electron position. In order to better describe the motion of noble metals, eg. Au, Ag, Cu, an additional term $\omega_0^2\mathbf{x}$ is needed here to account for the interband transition:

$$m[\ddot{\mathbf{x}} + \gamma\dot{\mathbf{x}} + \omega_0^2\mathbf{x}] = -e\mathbf{E}e^{-i\omega t}, \tag{1.4}$$

If the incident field varies harmonically with frequency in time ω as $e^{-i\omega t}$, the dipole $\mathbf{p}$ contributed by one electron can be written:

$$\mathbf{p} = -e\mathbf{x} = \frac{e^2}{m}\frac{\mathbf{E}}{\omega_0^2 - \omega^2 - i\omega\gamma}. \tag{1.5}$$

If we then suppose that our material consists of N molecules/nuclei per unit volume each with Z electrons, each with their own binding frequency ω_j and damping γ_j, the dipole per molecule is defined:

$$\mathbf{p}_{\text{mol}} = \sum_j^Z \frac{e^2}{m}\frac{\mathbf{E}}{\omega_j^2 - \omega^2 - i\omega\gamma_j}. \tag{1.6}$$

Then the polarization density becomes,

$$\mathbf{P} = \frac{\mathbf{p}_{\text{mol}}}{V_{\text{mol}}} = N \sum_{j}^{Z} \frac{e^2}{m} \frac{\mathbf{E}}{\omega_j^2 - \omega^2 - i\omega\gamma_j}, \tag{1.7}$$

which is often written in terms of an oscillator strength f_j, characterizing the number of electrons per molecule with the same resonance frequency and damping.

The polarization density $\mathbf{P}$ is related to the permittivity ϵ through the susceptibility χ, which is the constant of proportionality between the electric field $\mathbf{E}$ and induced polarization $\mathbf{P} = \chi\mathbf{E}$. The permittivity is defined as the constant of proportionality between the electric field and the displacement field, which arises in constructing the macroscopic Maxwell's equations, displacement field $\mathbf{D} = \epsilon\mathbf{E} = \mathbf{E} + 4\pi\mathbf{P}$. Combining these expressions allows us to define the electric permittivity:

$$\epsilon = 1 + 4\pi\chi \tag{1.8}$$

$$= 1 + 4\pi N \sum_{j}^{Z} \frac{e^2}{m} \frac{1}{\omega_j^2 - \omega^2 - i\omega\gamma_j}. \tag{1.9}$$

This dielectric function of frequency is simply a collection of Lorentz oscillators.

The Drude dielectric function is obtained by freeing the electrons from their respective nuclei, accomplished by taking their resonance frequencies $\omega_j \to 0$ and all $\gamma_j \to \gamma$ to represent the scattering rate of free electrons against the background nuclear lattice. Defining the plasma frequency $\omega_p \equiv \frac{NZe^2}{m\epsilon_0}$ to be the characteristic response of the free electron gas, the *Drude dielectric function* can be written:

$$\epsilon(\omega) = \epsilon_\infty - \frac{\omega_p^2}{\omega^2 + i\omega\gamma}, \tag{1.10}$$

where a phenomenological high frequency limit ϵ_∞ helps account for the low-energy tails of higher energy bound-electron excitations that are not explicitly modeled but do contribute slightly to the optical response of gold which much of this thesis is focused.

1.3.2 Localized surface plasmon resonances

The collective oscillations of free electrons in metals is called plasma oscillation [45]. This oscillation can propagate at the interface between metal and dielectric, evanescently confined in the direction normal to propagation which is called a surface plasmon polaritons (SPP). External light cannot directly excite a SPP, instead phase-matching techniques are needed [45, 46]. When the oscillation is confined to a metal particle with the size smaller than the wavelength, a resonance called the localized surface plasmon resonance (LSPR) arises (Fig. 1.5). Here the term plasmon refers to the quantum of this oscil-

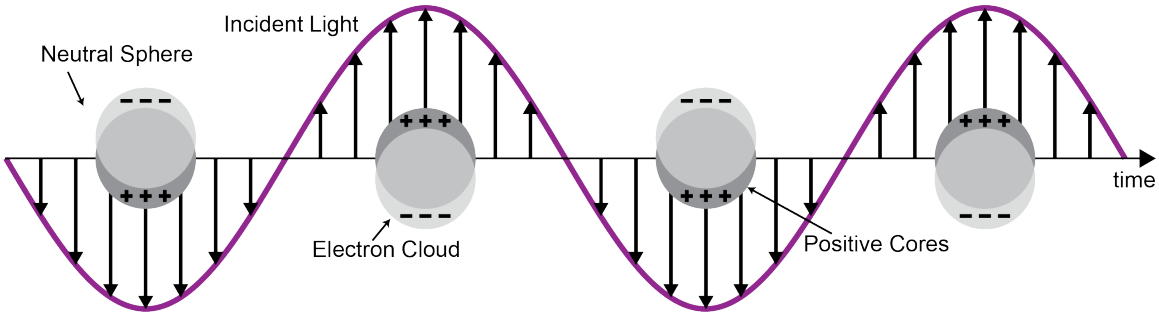

Figure 1.5: **Plasmon induced in a metal particle by light** Adapted from [38].

lation. Unlike bulk SPPs, LSPRs can be excited directly by external light (Fig. 1.5) because the sub-wavelength particle size means that the momentum matching conditions are relaxed. The associated fields are also confined to a much smaller volume and hence, are more intense. For gold and silver nanoparticles, the LSPR frequency is within the visible range of the electromagnetic spectrum which makes them good candidates for optical nanoantennas.

The interaction between nanoparticle and electromagnetic field can be analyzed using a quasi-static approximation where the size of a particle is much smaller than the incident wavelength, $a \ll \lambda$. Let's start by defining the polarizability of a small nanosphere with radius a. In this approximation, Maxwell's equations, which govern electrodynamics, reduce to Poisson's equation for the electrostatic potential Φ. In an isotropic linear medium

defined by the relative electric permittivity ϵ,

$$\nabla^2\Phi = 4\pi\frac{\rho}{\epsilon} \tag{1.11}$$

in Gaussian (or CGS) units, where ρ is the charge density. To define the polarizability, we ask for the field induced by polarization of the particle given a spatially constant field in a non-absorbing medium with dielectric constant ϵ_b. Placing the particle at the coordinate origin, we may define the incident field E_0 in spherical coordinates as:

$$\lim_{r\to\infty}\Phi = -E_0 r\cos\theta = -E_0 z. \tag{1.12}$$

In order to solve for the potential induced by this field, the free charge in Eq. 1.11 is $\rho = 0$ everywhere. The potential inside and outside the particle must obey the boundary conditions:

$$\Phi_{\text{in}}|_S = \Phi_{\text{out}}|_S, \qquad \epsilon\left.\frac{\mathrm{d}\Phi_{\text{in}}}{\mathrm{d}n}\right|_S = \epsilon_b\left.\frac{\mathrm{d}\Phi_{\text{out}}}{\mathrm{d}n}\right|_S, \tag{1.13}$$

at the surface of the particle, in terms of the coordinate normal to the surface defined by unit vector $\mathbf{n} = n\hat{n}$.

The above differential equation and boundary conditions can be solved analytically for the case of a perfectly spherical particle. Thus, for a nanosphere with radius a, the potential inside and out can be shown to be:

$$\Phi_{\text{in}} = -\frac{3\epsilon_b}{\epsilon + 2\epsilon_b}E_0 r\cos\theta, \tag{1.14}$$

$$\Phi_{\text{out}} = -E_0 r\cos\theta + a^3\frac{\epsilon - \epsilon_b}{\epsilon + 2\epsilon_b}\frac{\cos\theta}{r^2}E_0, \tag{1.15}$$

by matching coefficients of the spherical harmonic expansion. The potential outside the sphere Φ_{out} is found to be that of the incident field plus the potential of an ideal point

dipole:

$$\Phi_p = \frac{p\cos\theta}{\epsilon_b r^2} = \frac{\mathbf{p}\cdot\mathbf{r}}{\epsilon_b r^3} \tag{1.16}$$

with dipole moment[3],

$$\mathbf{p} = a^3\epsilon_b\frac{\epsilon-\epsilon_b}{\epsilon+2\epsilon_b}\mathbf{E}_0. \tag{1.17}$$

Defining the polarizability α to be the constant of proportionality between the incident field and the induced dipole,

$$\mathbf{p} = \alpha\epsilon_b\mathbf{E}_0, \tag{1.18}$$

$$\alpha = a^3\frac{\epsilon-\epsilon_b}{\epsilon+2\epsilon_b}. \tag{1.19}$$

Thus, for a small nanosphere under the quasi-static approximation, the polarizability has a resonance when $\epsilon + 2\epsilon_b$ researches minimum. Because the medium is non-absorbing, $\mathrm{Im}(\epsilon) = 0$, this minimum is satisfied when

$$\mathrm{Re}(\epsilon) = -2\epsilon_b. \tag{1.20}$$

This condition is also called the Fröhlich condition. Under the Fröhlich condition, besides polarization, the absorption and scattering efficiency are also consequently enhanced which are easier to measure optically. For instance, the scattering spectrum of a nanoparticle can be easily obtained using dark-field microscopy which is mentioned in Sec. 1.2.1. According to Eq. 1.20 refractive index ϵ_b change of the environment directly shifts the resonance of the embedded plasmonic nanoparticles. Hence, sensing the changes of refractive index is one of the most important applications of plasmonic nanoparticles [33,38,47–51]. For gold and silver nanoparticles, the resonance falls into the visible and IR region of the spectrum which therefore have been widely studied in the context of fluorescence.

[3]We are using Gaussian Units here. If we were in SI units, we need to multiply by the term $4\pi\epsilon_0$ as seen in many textbooks [45,46].

A similar procedure leads to the polarizability of a prolate spheroid which is obtained from an ellipse rotating along its major axis. In this case, the polarizability is not isotropic, and Eq. 1.18 must be written $\mathbf{p} = \boldsymbol{\alpha}\cdot\mathbf{E}$. The dyadic polarizability is diagonal in the Cartesian basis with unit vectors aligned with the prolate spheroid's principal axes. If the long semi-radius is aligned along $\hat{e}_x$,

$$\boldsymbol{\alpha}^{\mathrm{QS}} = \begin{pmatrix} \alpha_a^{\mathrm{QS}} & 0 & 0 \\ 0 & \alpha_b^{\mathrm{QS}} & 0 \\ 0 & 0 & \alpha_b^{\mathrm{QS}} \end{pmatrix} \tag{1.21}$$

where α_a is the polarizability along the long axis of the spheroid with semi-radius a and α_b is polarizability of the degenerate short axis with semi-radius b. With total volume $V = \frac{4\pi}{3}ab^2$, the principal components of the polarizability are:

$$\alpha_i^{\mathrm{QS}} = \frac{V}{4\pi}\frac{\epsilon - \epsilon_b}{1 + L_i(\epsilon - \epsilon_b)}. \tag{1.22}$$

The geometric factors L_i are defined by,

$$L_a = \frac{1 - e^2}{e^3}(-1 + \frac{1}{2e}\ln\frac{1+e}{1-e}), \tag{1.23}$$

$$L_b = \frac{1 - L_a}{2}, \tag{1.24}$$

where $e^2 = 1 - \frac{a^2}{b^2}$ is the eccentricity.

The quasi-static approximation provides a good model for the plasmonic response of noble metal nanoparticles, but does not show quantitative agreement with experiment for metal particles larger than $\sim$ 100 nm in size. For the highly symmetric particles like the spheroid, the full electrodynamic optical response consistent with Maxwell's equations can be written in analytic form using a modified Mie theory [47]. What results from this procedure are the scattered fields expressed as series expansions in vectorized spherical harmonics, which obscure the dynamics of the plasmon resonance. A compromise between the transparent *quasi-static approximation* and rigorous scattering theory can be

had by expanding the Mie coefficient describing dipole scattering about small wavenumber k and obtaining corrections to the quasistatic result. In terms of the components of the quasi-static polarizability $\alpha^{\mathrm{QS}}(\omega)$ defined in Eq. 1.22, the polarizability in the modified long-wavelength approximation is obtained by expanding each Bessel function inside the Mie coefficient to third order in k:

$$\alpha_i^{\mathrm{ML}}(\omega)\frac{\alpha_i^{\mathrm{QS}}(\omega)}{1-\frac{k^2}{l_E}D_i\alpha_i^{\mathrm{QS}}(\omega)-i\frac{2k^3}{3}\alpha_i^{\mathrm{QS}}(\omega)}, \tag{1.25}$$

for incident light polarized along the ith principal axis of the spheroid. The newly introduced geometric factors D_i are:

$$D_a=\frac{3}{4}\left(\frac{1+e^2}{1-e^2}L_a+1\right), \tag{1.26}$$

$$D_b=\left(\frac{3}{e}\operatorname{arctanh}e-D_a\right)\frac{a}{2b}. \tag{1.27}$$

Here we only expand the Bessel function to a third order in k. Theoretically, the higher order it goes, the better the modelling results is. However, for the purpose of the researching in this thesis, we found that third order is sufficient.

1.4 Optical lithography and electron-beam lithography

Nanolithography is the science of etching, writing or printing to modify material with features under 100 nm. Because of its precise control, it serves as a powerful tool for material science research that requires control in nanometer scales such as nanophotonics, biomedical engineering and nanocircuits. Electron-beam lithography (EBL) is one of the nanolithography methods used in Chapter III.

Optical lithography refers to a printing process that uses visible or ultraviolet light to form patterns on the photoresist which is used in Chapter II. The pattern is written onto the wafer surface using a light source and a photo mask. There are three types of printing:

contact, proximity, and projection printing. No matter which type of print method is used, the writing resolution suffers from near-field or far-field diffraction to some degree. The resolution one can get from a typical optical lithography is around 0.25 microns. Fig. 1.6a shows the schematic of a typical projection printing optical lithography process. A photosensitive polymer also called photoresist is coated onto a substrate. By illuminating the coated substrate through a mask, different parts of the substrate will be exposed to the light depending on the pattern of the mask. Upon exposure, the photoresist can became either more soluble which is called positive resist or less soluble which is called negative resist. With a positive tone resist like PMMA, the exposed parts will be washed away in the developer solution, leaving the unexposed part on the substrate. At this point, the major part of optical lithography is basically done. Different sample designs would require different paths afterwards, such as etching and evaporation. Fig. 1.6a shows the metal evaporation process following the lithography. Electron beam evaporation allows one to evaporate uniform thin layer of metal on to a substrate with nanometer precision. Then metal layer on top of the photoresist is peeled off when the photoresist is washed away during lift-off step, however, the metal layer directly on the substrate remains. Fig. 1.6c shows gold coordinates on a coverslip made by this process. The mask is reusable which improves the sample fabrication time.

Electron-beam lithography (EBL) on the other hand uses electron beams to write on the resist following a programmable pattern. As shown in Fig. 1.6b, the process of EBL is similar to optical lithography except that there is no mask involved and the writing source is the electron beam. EBL enables higher resolution writing than optical printing as optical printing suffers from the diffraction of light. Additionally, EBL requires the sample to be conductive whereas it is not necessary in optical lithography, which limits its application. One way to get around this limitation is by putting a conductive coating onto the non-conductive sample such as a glass coverslip, then etching or washing it away before developing. Once the e-beam sample is developed it can be treated the same way

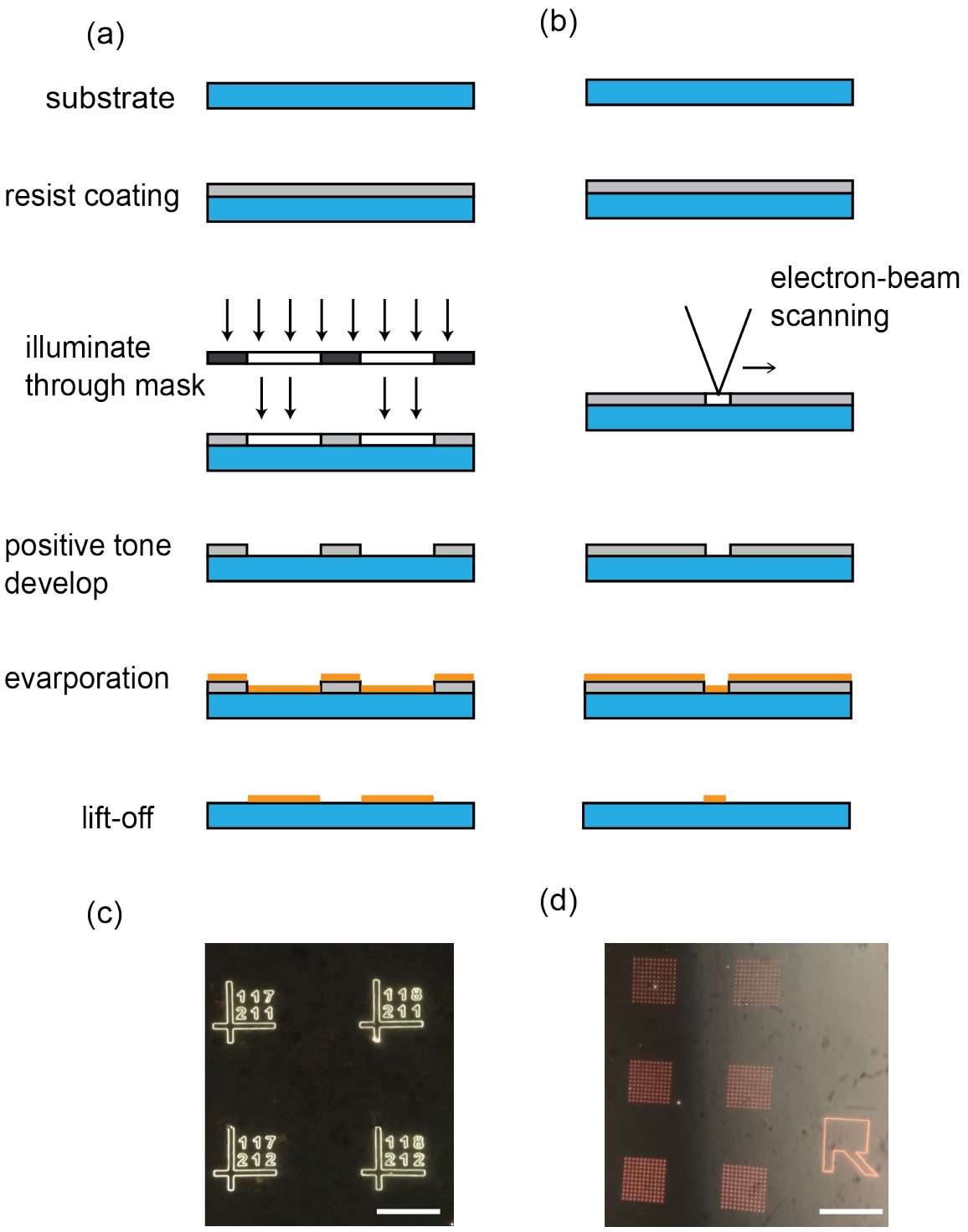

Figure 1.6: **Optical and electron-beam lithography processes.** (a) Optical lithography process. (b) Electron-beam lithography process. (c) Dark field image of gold grids on a coverslip made by optical lithography. (d) Dark field image of gold nanodisks written on a coverslip by EBL. The scale bars here are 10 μm.

as an optical lithography sample. Fig. 1.6d shows arrays of gold disks made by EBL which enables precise control on the shape and size of the disks, so I can fine tune the LSPR frequency of these nanodisks. These gold disks will be used in the Chapter III as plasmonic nanoantennas to study the emission coupling between antennas and single emitters.

1.5 Thesis outline

This thesis aims to understand how plasmonic nanoantennas affect fluorescent emission on the single-molecule level. In Chapter II, I investigate the polarization changes that result from plasmon-coupled emission by measuring the emission polarization of single dye molecules coupled to individual plasmonic Au nanorods. In Chapter II, by correlating the single-molecule emission polarization angle with the nanorod orientation and fluorescence wavelength, Goldwyn[4] and I discovered that the molecular emission polarization is significantly rotated towards the orientation of the nanoantenna's dominant plasmon mode, and we observed that this polarization rotation, or "mispolarization", can be as large as 90°. I used single-molecule polarization-resolved microscopy to measure the polarization angle distribution for two different dyes, one red dye, Cy5.5 (λ_{max} = 710 nm) and one bluer dye, Cy3 (λ_{max} = 570 nm) and I found that mispolarization occurs upon resonant plasmon-coupled fluorescence emission. Our electromagnetic simulations of the plasmon-coupled single-molecule emission polarization were consistent with these experimental observations. To elucidate these experimental and numerical trends, we developed a reduced-order analytical model that demonstrates explicitly how the change in emission polarization depends on both the far-field interference of the coherent emission from both molecular and plasmonic antennas as well as the near-field dynamics of the coupled system.

In Chapter III, I describe how I extended our research from emission polarization to

[4]I performed the experimental part and simulation. Goldwyn designed and developed the analytical model so as in Chapter III

emission localization. Goldwyn and I carried the analytical model further to not only elucidate the emission coupling but also to recover the true position and orientation of a coupled single emitter. We simulated the emission coupling between the dipoles and Au nanorod and we calculated the emission polarization and position based on our model and Gaussian fitting which is the conventional way to calculate those two properties. We then compared these calculated emission polarization and emission localization to the results coming from fitting the simulated emission to the analytical model. We found that the model was able to recover both the true polarization and position with far fewer than the two conventional methods. In the experiment, I designed and made a device that allowed us to obtain both the apparent emission position and the actual radio distance of the single emitter to the nanoantenna. I used dsDNA which is rigid on the scale of tens of nm, to precisely position the dyes. Knowing the ground truth of the dye location will allow us to ultimately apply our analytical model to the experimental data in the near future. Supported by simulations, I demonstrate that mislocalization is the result of fluorescence emission coupling whereas fluorescence enhancement is the result of both absorption and emission coupling.

In Chapter IV, I propose using QD and silver nanoparticles to achieve plasmon enhanced fluorescence without emission coupling. I use two-channel super-resolution imaging to characterize the intensity and spectral change of quantum dots upon coupling to plasmonic nanoparticles. I show that the average emission time of coupled QDs is similar to the non-coupled QDs but has a smaller standard deviation. The characterization will enable plasmon enhanced single quantum dot labeling to be used in bioimaging. Finally, in Chapter V, I propose a future direction of doing single-QD imaging with aluminum nanoparticles via DNA-PAINT technique. It provides a possible approach to achieve plasmon enhanced super-resolution imaging with reduced mislocalization.

Overall, this thesis focuses on emission coupling between plasmonic nanoantennas and single molecules. Both experimental and theoretical study of emission polarization

and localization are carried out in this thesis. The results will shine some light on the light-matter interaction between plasmonic nanoantennas and single molecules and leads to better plasmon-enhanced fluorescent application.

CHAPTER II

Rotation of Single-Molecule Emission Polarization by Plasmonic Nanorods

The work presented in the chapter has been published in

Tiancheng Zuo, Harrison J. Goldwyn, Benjamin P. Isaacoff, David J. Masiello, Julie S. Biteen. "Rotation of Single-Molecule Emission Polarization by Plasmonic Nanorods". *The Journal of Physical Chemistry Letters*,**10**,5047-5054 (2019). DOI: 10.1021/acs.jpclett.9b02270

Author contributions

TZ designed and carried out the experiments, analyzed data, and performed time-domain electromagnetic simulations with help from JSB. HJG developed and implemented the analytical model and performed frequency-domain electromagnetic simulations with help from DJM. BPI set up the time-domain electromagnetic simulations. TZ and HJG wrote the paper. All authors discussed the results and analysis, developed conclusions, and edited the paper.

2.1 Abstract

The strong light-matter interactions between dyes and plasmonic nanoantennas enable the study of fundamental molecular-optical processes. Here, we overcome conventional limitations with high-throughput single-molecule polarization-resolved microscopy to measure dye emission polarization modifications upon near-field coupling to a gold nanorod. We determine that the emission polarization distribution is not only rotated toward the nanorod's dominant localized surface plasmon mode as expected, but is also unintuitively broadened. With a reduced-order analytical model, we elucidate how this distribution broadening depends upon both far-field interference and off-resonant coupling between the molecular dipole and the nanorod transverse plasmon mode. Experiments and modeling reveal that a nearby plasmonic nanoantenna affects dye emission polarization through a multicolor process, even when the orthogonal plasmon modes are separated by approximately three times the dye emission linewidth. Beyond advancing our understanding of plasmon-coupled emission modifications, this work promises to improve high-sensitivity single-molecule fluorescence imaging, biosensing, and spectral engineering.

2.2 Introduction

Nanoantennas couple the far field to the near field by converting propagating waves to localized fields [34]. Understanding and measuring how optical nanoantennas couple to their local environment is a critical step toward controlling and enhancing near-field properties for applications as diverse as biosensors [33, 52], light-emitting devices [53, 54], surface-enhanced Raman spectroscopy [55, 56], and super-resolution microscopy [41–43, 57]. Noble metal nanoparticles respond strongly to light and are efficient nanoantennas. Upon optical excitation, localized surface plasmons–collective oscillations of the metal conduction-band electrons-are created at the nanoparticle surface and concentrate

radiation into intense near fields through which optical processes in the surrounding local environment can be enhanced.

One intriguing near-field effect of plasmonic nanoparticles is their ability to interact with nearby fluorescent dye molecules. Reported experimental and theoretical studies of the coupling of single dye molecules with metal nanoparticles have described how these nanoantennas modify the rate [42, 58–63], spatial distribution [43, 64, 65], spectrum [60], and polarization [41,66–71] of fluorescence emission. Single-molecule experiments, which avoid ensemble averaging [43], have further shown that single-molecule fluorescence emission is re-directed by a plasmonic nanoantenna [72], and recent theory has proposed that this so-called mislocalization can be attributed to the superposition and interference of the molecule and nanoantenna far-field emission as well as to the near-field coupling between the two emitters [65, 73]. In general, the excitation and decay of coupled fluorescent molecules and nanoantennas can be treated as separate processes as there is no coherence between plasmon-coupled molecular absorption and emission [60, 74] and experiments have shown that emission mislocalization is independent from enhanced absorption [72, 75].

Despite these research activities, the interaction between nanoantennas and nearby molecules is still not fully understood. Previous studies have demonstrated that emission polarization of a single emitter can be modified by the orientation of a nearby asymmetric nanoantenna such as a nanorod or Yagi-Uda antenna [67, 69, 71]. Here, we extend these previous studies by using points accumulation for imaging in nanoscale topography (PAINT) experiments [25,41,76,77], a microscopy technique mentioned in Sec. 1.2.1, to sample thousands of molecules that transiently adsorb on the coverslip near each antenna. We also explicitly subtract the contribution of plasmonic particle photoluminescence [78], and develop novel understanding of how this dye-nanoantenna coupling influences the polarization of emitted light by combining single-molecule experiments with a reduced-order analytical model. The model results not only agree with simulation and provide a

faster route to polarization prediction, but elucidate the mechanisms underlying emission polarization modification from a coupled dye-antenna system by isolating effects from the nanoantenna's two orthogonal dipole plasmon modes. The model also reveals the contributions to emission polarization from near-field coupling and far-field interference, both of which vary differently with dye-nanoantenna position and orientation.

More specifically, we investigate the polarization changes that result from plasmon-coupled emission by measuring the emission polarization of single dye molecules coupled to individual plasmonic nanorods. By correlating the single-molecule emission polarization angle with the nanorod orientation and fluorescence wavelength, we observe that the molecular emission polarization is significantly rotated toward the angle of the nanoantenna dominant plasmon mode as previously reported [66–71], and can be as large as 90°. We use single-molecule polarization-resolved microscopy to measure the angle distribution of this "mispolarization" for two different dyes-one red, Cy5.5 ($\lambda_{max} = 710\,nm$) and one bluer, Cy3 ($\lambda_{max} = 570\,nm$), and we find that measurable mispolarization occurs even when off resonance from the plasmon. This emission effect is therefore different from the fluorescence intensity and fluorescence emission spectrum, which are affected by both plasmon-coupled absorption and plasmon-coupled fluorescence emission [72].

2.3 Experimental results and discussions

2.3.1 Single-molecule polarization-resolved microscopy

To measure the emission polarization of single dye molecules coupled to gold nanorods, we achieve a sparse distribution of fluorescent molecule detections by placing a drop of nanomolar dye solution over a nanorod-coated coverslip (Fig. 2.1a). In this PAINT experiment [25,41,76,77], most molecules diffuse rapidly in solution and are not detected by the camera (at 10 frames/s); only those molecules that transiently adsorb on the coverslip are captured by the camera. The high magnification of the microscope (160 nm/imaging pixel)

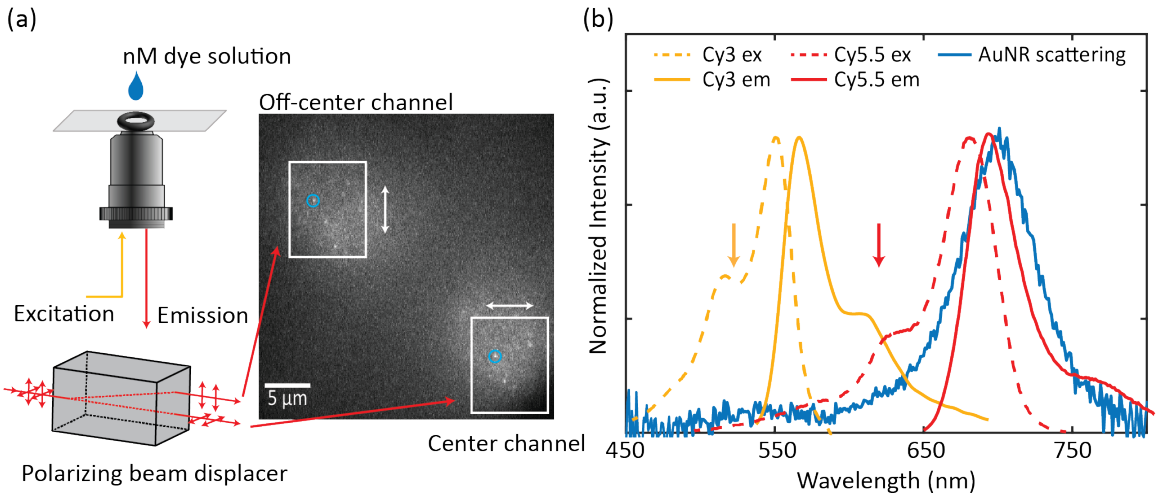

Figure 2.1: **Experimental setup and spectral design.** Experimental setup and spectral design. (a) Single-molecule polarization-resolved microscopy experiment setup. A low-concentration dye solution is excited by circularly polarized laser illumination (yellow). A polarizing beam displacer PBD separates the emission (red) into two orthogonally polarized output channels (white boxes; the white arrows indicate the polarization direction). The cyan circles indicate the same molecule detected in both channels. (b) Dark-field scattering spectrum of an isolated nanorod immobilized on a coverslip (blue); Cy3.5 fluorescence excitation and emission spectra (yellow dashed and solid lines, respectively); Cy5.5 fluorescence excitation and emission spectra (red dashed and solid lines, respectively). Yellow and red arrows indicate the excitation wavelengths for Cy3 and Cy5.5 respectively.

and low concentration of dye molecules enable us to characterize one molecule at a time. A PBD in the emission pathway of our single-molecule microscope (Fig. 2.1a) separates the emission into two orthogonally polarized output beams, which are then offset from one another and projected onto the camera (white "Center channel" and "Off-center channel" boxes in Fig. 2.1a). In this two-channel, one-camera setup, the emission from each single dye molecule appears in two channels (e.g. cyan circles in Fig. 2.1a), but the intensity is different in each channel. The apparent emission polarization angle, $\phi_{apparent}$, of each fluorescent molecule and photoluminescent nanorod is thus related to the intensity ratio recorded in these two channels according to:

$$\phi_{apparent} = tan^{-1}\sqrt{\frac{I_{off-center}}{I_{center}}}, \tag{2.1}$$

where I_{center} and $I_{off-center}$ are the detected intensities in the center and off-center images, respectively, integrated over a diffraction-limited area. This expression maps all angles into the first quadrant (between 0 and 90°) because phase information is lost from both field components.

Single-molecule polarization-resolved microscopy measures the average emission polarization in the image plane, which corresponds to the physical dipole orientation for isolated single emitters (dye molecules or nanorods) lying flat on the microscope coverslip. The dark-field scattering of the nanorod is strongly polarized along the nanorod longitudinal axis and is consistent with the nanorod having a larger polarizability along its long axis [60, 79, 80]. This angle is measured with respect to the PBD axis. In these microscopy experiments, the large numerical aperture (NA) objective produces some intensity cross-talk between the channels. This cross-talk is demonstrated in full-field electromagnetic simulations in Fig. 2.2. Though the molecules in this experiment can be approximately

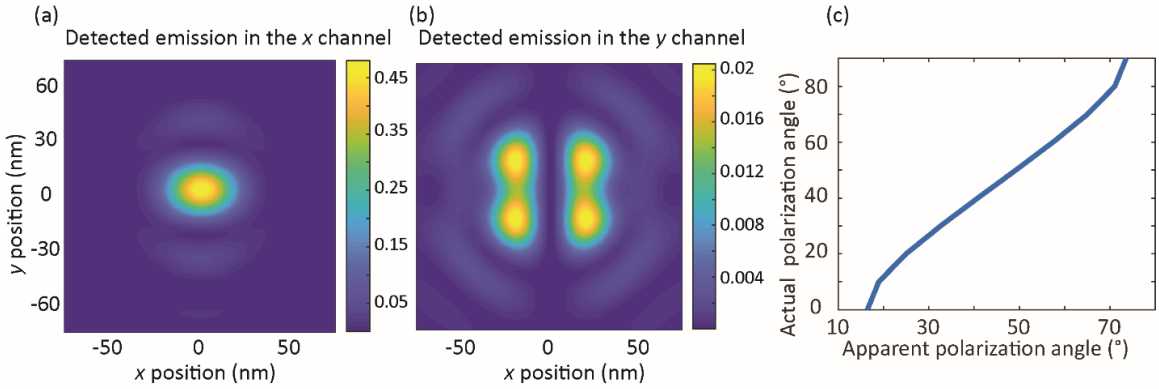

Figure 2.2: **Far field projection of simulated dipole and cross-talk.** (a) Far-field intensity map detected in the x polarization channel of dipole radiation which is polarized along x axis direction. (b) Far-field intensity map detected in the y polarization channel of a dipole radiation which polarizes along x axis direction. (c) Mapping of apparent emission polarization angle, which is calculated from simulation results by using Eq. 2.3.1, to the actual emission polarization angle, which is the simulation input angle.

considered perfect dipoles, they are detected in the far field after radiation through a high numerical aperture microscope objective. This geometric consideration leads to signal in

the perpendicular channel even for a molecule oriented perfectly along one axis. For example, we simulated a single dipole emitter in water on a glass coverslip with polarization along the x axis, most of the intensity is detected in the x channel (Fig. 2.2a), but the intensity in the perpendicular channel is not zero; rather the y-channel intensity (Fig. 2.2b) is 13% of the intensity in the x channel. This mismatch between the calculated emission polarization angle and actual emission polarization angle is seen in Fig. 2.2c. This map is used to recover the actual angles in the finite difference time domain (FDTD) simulations (Fig. 3.2a). The experimental results shown in Fig. 2.3 were not corrected by using this table as the error introduced in the background subtraction makes the apparent angle and actual angle not a one-to-one relationship any more.

We use the two-channel experiment to investigate how detuning the dye emission spectrum from the nanorod localized surface plasmon (LSP) spectrum affects the emission polarization from the coupled dye-nanorod system. For gold nanorods, the single-nanorod PL polarization has been found to closely resemble the dominant, longitudinal LSP mode, observed in dark-field scattering [81, 82]. The fluorescence emission spectrum of the red dye Cy5.5 (Fig. 2.1b; solid red line) overlaps with the nanorod longitudinal LSP scattering resonance (Fig. 2.1b; blue line). The intensity of the longitudinal LSP mode, which peaks at 700 nm, is much stronger than transverse mode, which peaks at 560 nm (Fig. 2.1b; blue line). Therefore, by exciting the dye with a 635-nm laser, whose wavelength is far detuned from the nanorod LSP resonance (Fig. 2.1b; red arrow), we avoid fluorescence absorption enhancement to isolate the effects of coupling in the fluorescence emission. As a control experiment, similar measurements were performed with the red dye Cy3 whose emission and excitation peaks are both far detuned from the longitudinal LSP resonance (Fig. 2.1b; yellow lines).

2.3.2 Detection of plasmon-induced emission polarization rotation from resonantly coupled dye molecules

Detection of plasmon-induced emission polarization rotation from resonantly coupled dye molecules. We selected a group of seven nanorods with different orientations determined by 2.3.1 and measured the fluorescence polarization of single Cy5.5 molecules near each nanorod. The dark-field scattering spectra and relative angles of those nanorods are displayed in Fig. 2.5. Each system was rotated three times to sample 21 different nanorod orientations relative to the PBD axis. Simulation and model results show that molecules located more than 150 nm from the center of the nearest nanorod experience negligible mispolarization or mislocalization, and therefore these molecules experience no significant plasmonic interaction [77]. We refer to molecules located more than 400 nm from the nanorod centers as "Off-nanorod" and molecules located within 120 nm of the nanorod centers "On-nanorod" molecules. Intermediate molecules were not considered to allow differentiation between the two populations.

For the Off-nanorod molecules, the distribution of emission polarizations measured for the Off-nanorod Cy5.5 dyes (Fig. 2.3.2a) peaks at 45°. Since the molecules adsorb non-specifically to the surface with no known favored orientation, purely z-oriented emitters would contribute equally in the x and y channels, leading to an artificially enhanced 45° population. Moreover, this symmetrically peaked distribution is also attributed to artifacts introduced in background-subtraction that systematically invalidate data points at low or high angles due to signal-to-noise constraints. Additionally, even in the absence of noise, the polarization cross-talk generated by the high NA objective bounds the angle domain to $\sim 17° - 73°$. A quantitative analysis of these artifacts is presented with simulated single-molecule data in Fig. 2.4.

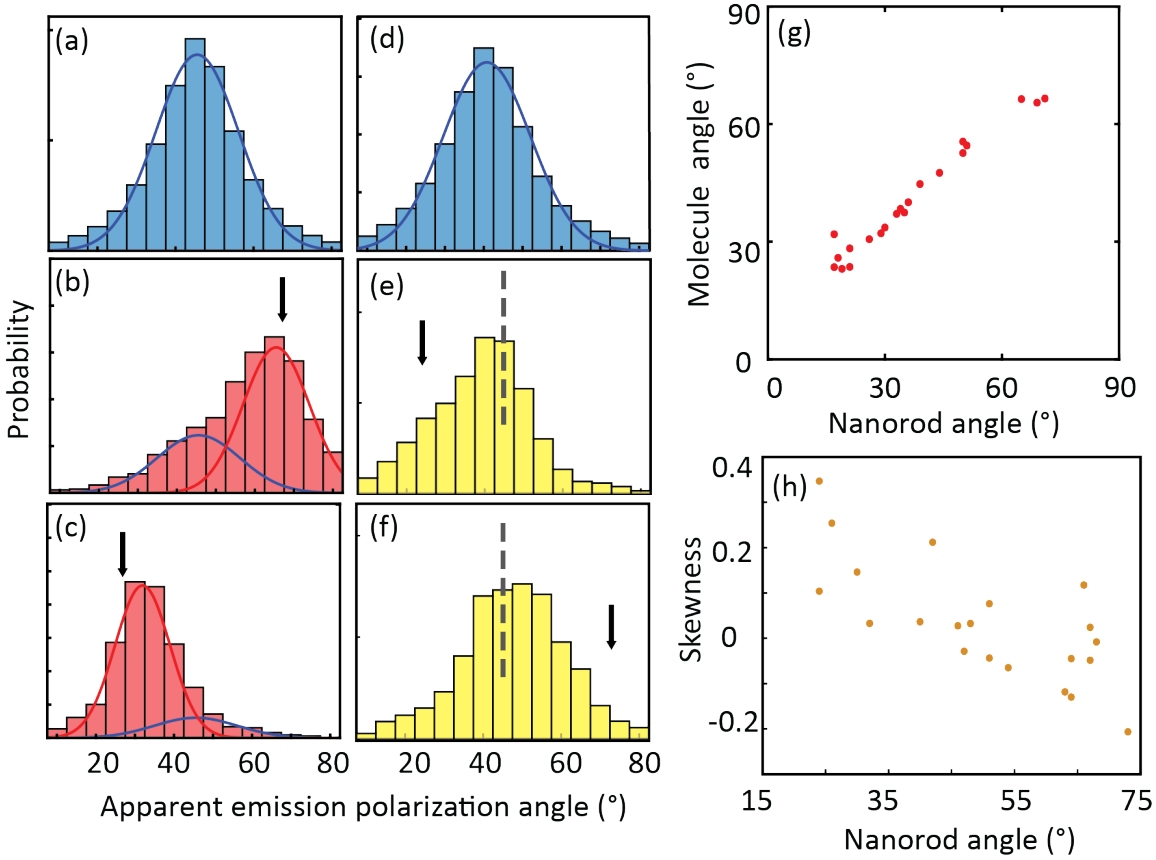

Figure 2.3: **Characterization of Cy5.5 and Cy3 molecule apparent polarization angles,** $\phi_{apparent}$. (a, d) Emission polarization angle distributions of Off-nanorod Cy5.5 and Off-nanorod Cy3 single molecules, respectively, and Gaussian curve fits. (b, c) Emission polarization angle of On-nanorod Cy5.5 single molecules. (e, f) Emission polarization angle of On-nanorod Cy3 single molecules. Each histogram in (a-f) collects the apparent emission polarization angles of 2,000 - 6,000 single molecules. The black arrows in b, c, e, and f indicate the measured orientation angle of the nanorod. The vertical dashed lines in e and f indicate 45°. The histograms in b, c, e, and f are fit to the sum of two Gaussian curves: the blue one has center and width corresponding to the blue curve in a or d, and the red one is not constrained. (g) Measured Cy5.5 average polarization angles vs. nanorod orientation angle. Each point comes from the peak of a red curve as in b and c. (h) Skewness of the measured Cy3 molecule emission polarization angle distribution vs. nanorod orientation angle.

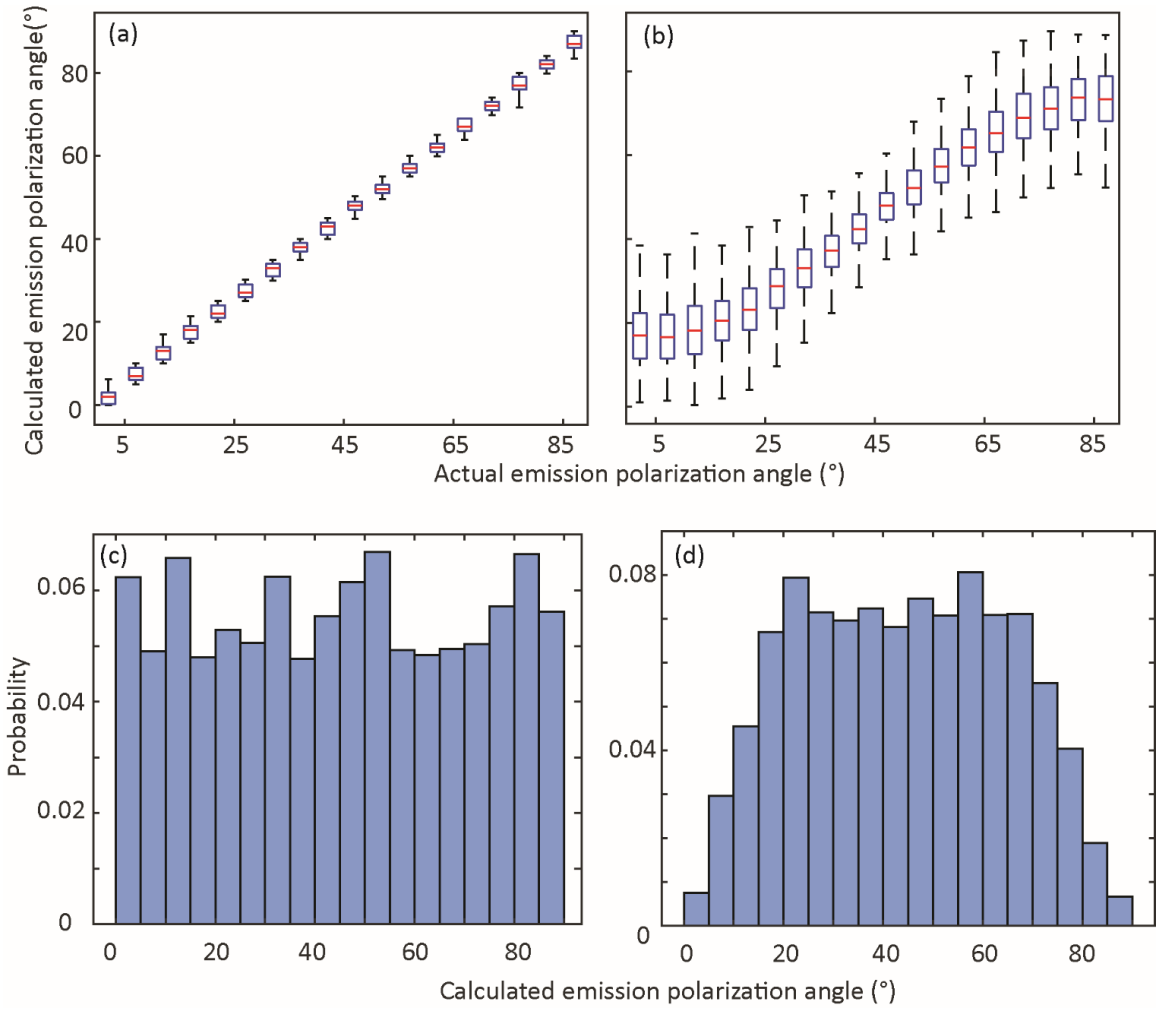

Figure 2.4: **Correspondence between the calculated and actual emission polarization angle.** Correspondence between the emission polarization calculated from Eq. 2.3.1 and the actual emission polarization angle input into simulations for (a) simulated no background noise movies and (b) simulated movies with background noise. On each histogram box, the central mark indicates the median, and the bottom and top edges of the box indicate the 25th and 75th percentiles, respectively. The whiskers extend to the most extreme data points not considered outliers. Distribution of calculated emission polarization angle for (c) simulated no background noise movies and (d) simulated movies with background noise.

In the simulations here, the fluorescence intensity of each molecule was drawn from a Gaussian distribution of molecule brightnesses, and the emission polarization of each molecule was drawn from a flat distribution. In movies with background noise, we incorporated shot noise (Poissonian probability distribution) into these simulations to attain a signal-to-noise ratio that matches the experiments. In the absence of noise, the angles calculated by Eq. 2.3.1 correspond well to the actual input angle (Fig. 2.4a). Hence, in the absence of noise, the distribution of calculated molecule emission polarization angles matches the flat distribution input into the simulation (Fig. 2.4c). However, when background shot noise is added, Fig. 2.4b shows that the error in determination of the angle increases appreciably. In particular, the estimated angle of dipoles oriented far from 45° is biased toward 45°. This error results from the background noise subtraction necessary to process single-molecule experiments. This bias toward 45° at the center of the estimated emission polarization distribution (Fig. 2.4d). We also investigated whether this peak is due to a physical rotation of the molecules on the coverslip surface, but we found no significant time-dependent broadening of the distribution within the imaging frame integration time of the experiment, 100 ms/frame (Fig. 2.6), which supports the assumption of each molecule having a well-defined dipole moment orientation.

For the On-nanorod molecules, Fig. 2.3b-c shows the distributions of measured polarizations for On-nanorod Cy5.5 molecules, in which the nanorod longitudinal axis is oriented at 67° and 28°, respectively (black arrows). Though the physical orientation of the Cy5.5 molecules here is random as in the Off-nanorod case (Fig. 2.3a), the polarization distributions in Fig. 2.3b and c are shifted away from the 45° peak in Fig. 2.3a, and toward the nanorod orientation. The distributions of the On-nanorod Cy5.5 molecules of all 21 nanorod orientations are given in Fig. 2.7.

The On-nanorod distributions (Fig. 2.3b-c, Fig. 2.7) still include some molecules very weakly coupled to the nanorod due to the dependence of coupling both on separation and orientation [73]. To quantify the On-nanorod distribution shifts, we fit the emission

polarization distribution to the sum of two Gaussian distributions: the blue curves in Fig. 2.3b-c, and Fig. 2.7 have center and width corresponding to the blue fit in Fig. 2.3a, and the red curves are the $\phi_{apparent}$ distribution of the truly coupled On-nanorod Cy5.5 molecules. The peak angles of these 21 red curves are compared to the nanorod longitudinal axis orientation in Fig. 2.3g. In Fig. 2.3g, it is evident that the molecular $\phi_{apparent}$ has a bias toward the nanorod longitudinal axis, in agreement with the simulation (Fig. 2.8). Furthermore, resonant coupling to the nanorod leads to an average 2-fold enhancement in PL intensity; this enhancement is greatest when $\phi_{apparent}$ is aligned with the nanorod angle (Fig. 2.9).

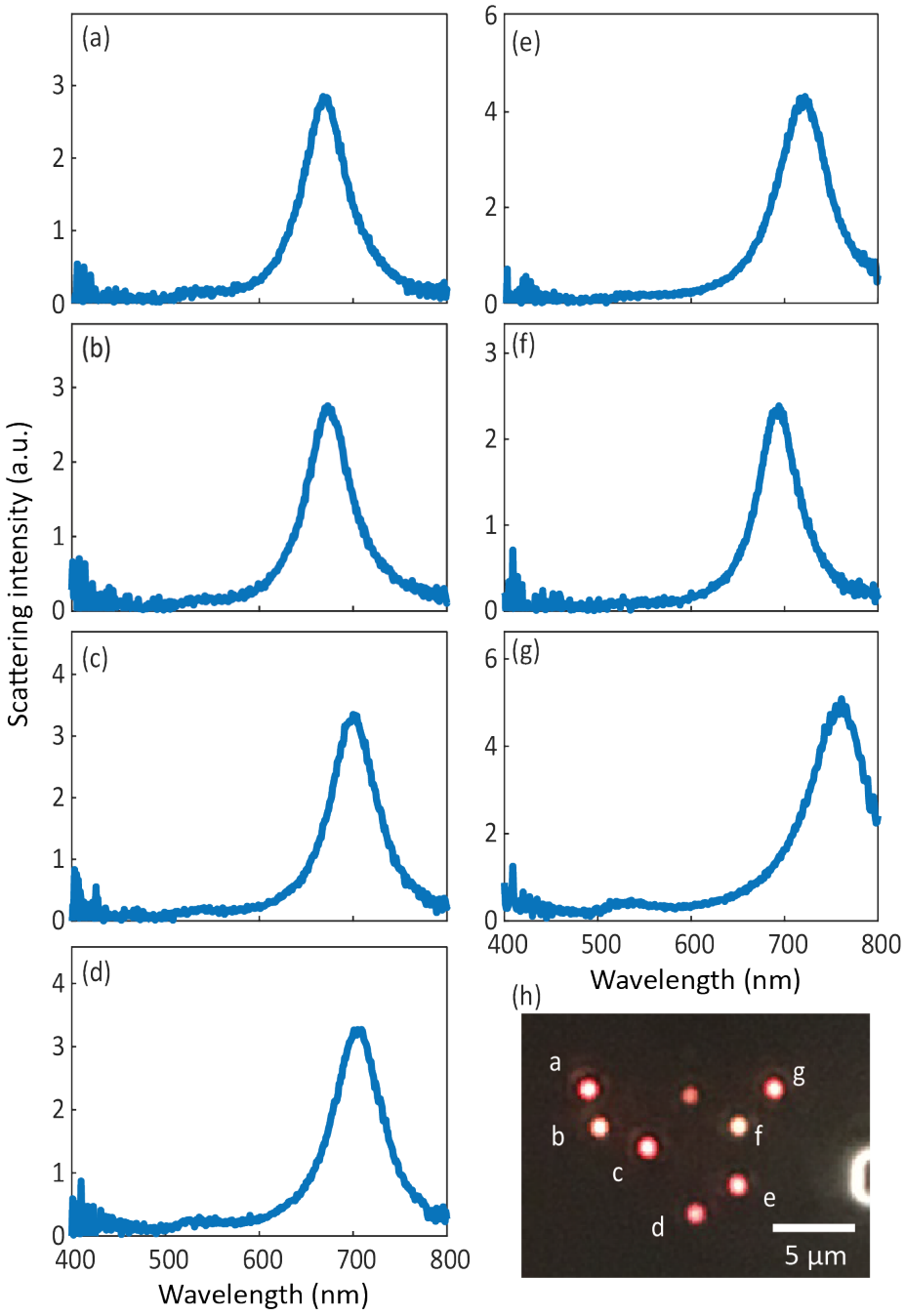

Figure 2.5: **Dark-field spectra of nanorods used in Cy5.5 experiment.** (a-g) Dark-field scattering spectra of the seven nanorods used for Cy5.5 single-molecule polarization-resolved microscopy. (h) Dark-field image of those seven nanorods (red dots). The bright feature at the right side is part of the labeled grid, which allows individual nanoparticles to easily be located. The initial orientations of the seven nanorods are: 69°, 51°, 44°, 71°, 50°, 30°, and 17°, respectively.

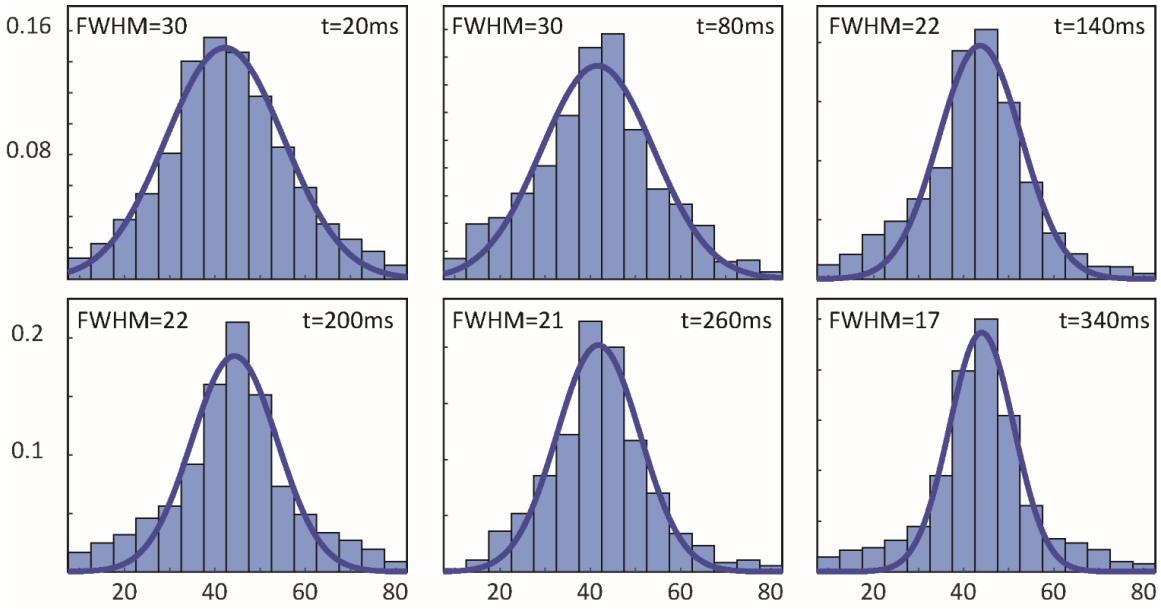

Figure 2.6: **Cy5.5 molecule emission polarization distribution with different integration time.** Emission polarization distribution for PAINT experiment of Cy5.5 molecules adsorbing transiently on a coverslip without nanorods. The integration time, t, was varied from 20 - 340 ms as indicated. The distributions were then each fit to a normal distribution (blue lines); the full width at half max (FWHM) for each curve is listed in each panel. As the frame integration time increases, the FWHM decreases, which indicates that some rotation of the molecules on the surface occurs, but that this rotation is limited in our experiments.

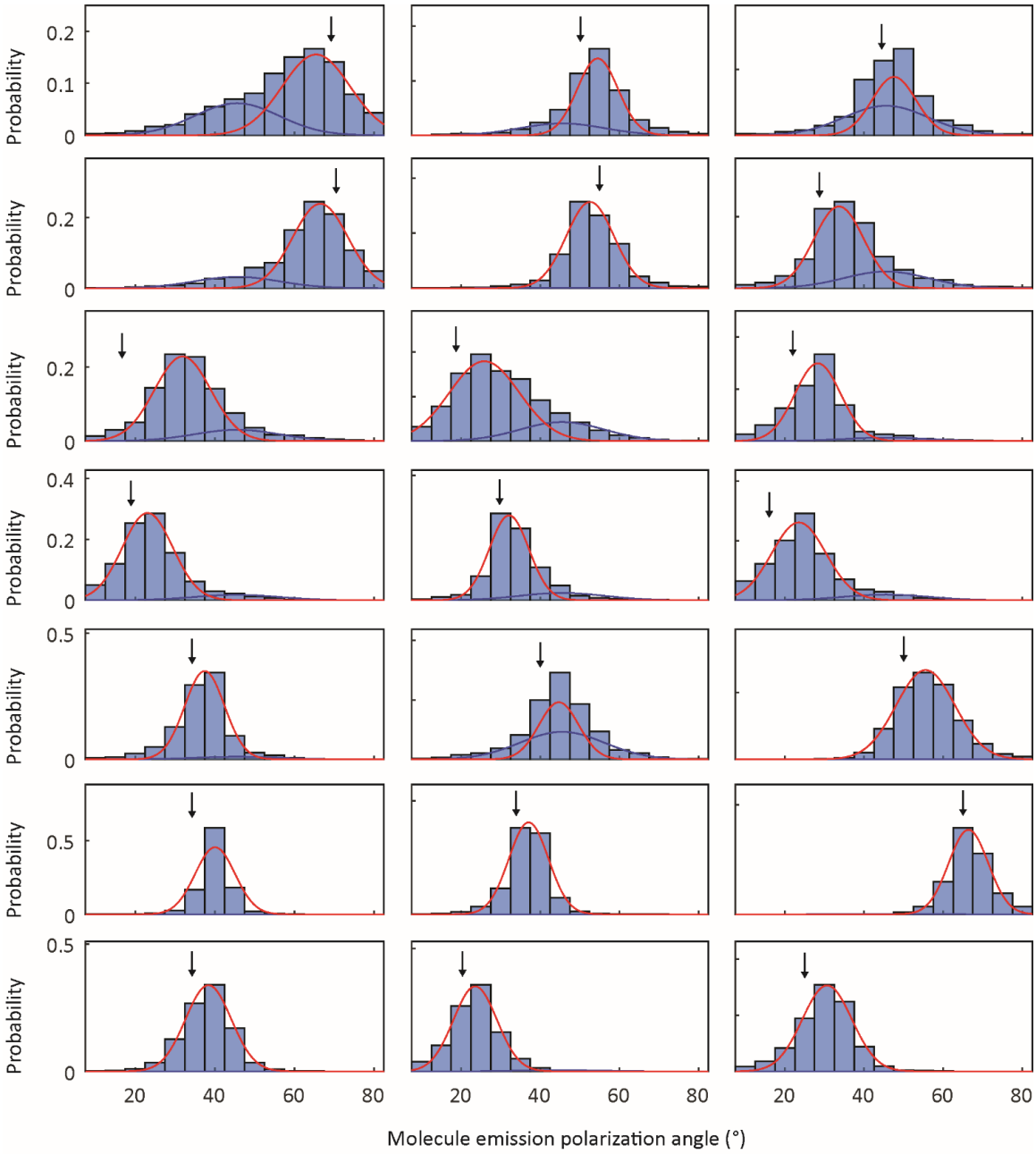

Figure 2.7: **On-gold Cy5.5 measured emission polarization angle distributions.** Measured emission polarization angle distributions of all Cy5.5 molecules detected near nanorods. The 21 panels show all 21 experimental configurations (7 nanorods x 3 rotations). The black arrow in each panel indicates the measured orientation of the nanorod in that experiment. Each distribution is fit to the sum of two Gaussian curves: the blue curves have center and width corresponding to the measured emission polarization angles of the Off-nanorod molecules (Fig. 2.3a), and the red curves therefore show the apparent emission polarization angle distribution of the On-nanorod molecules. The 1st and 7th panels correspond to Fig. 2.3b and c, respectively. Each histogram collects the apparent emission polarization angles of 2,000 - 6,000 single molecules.

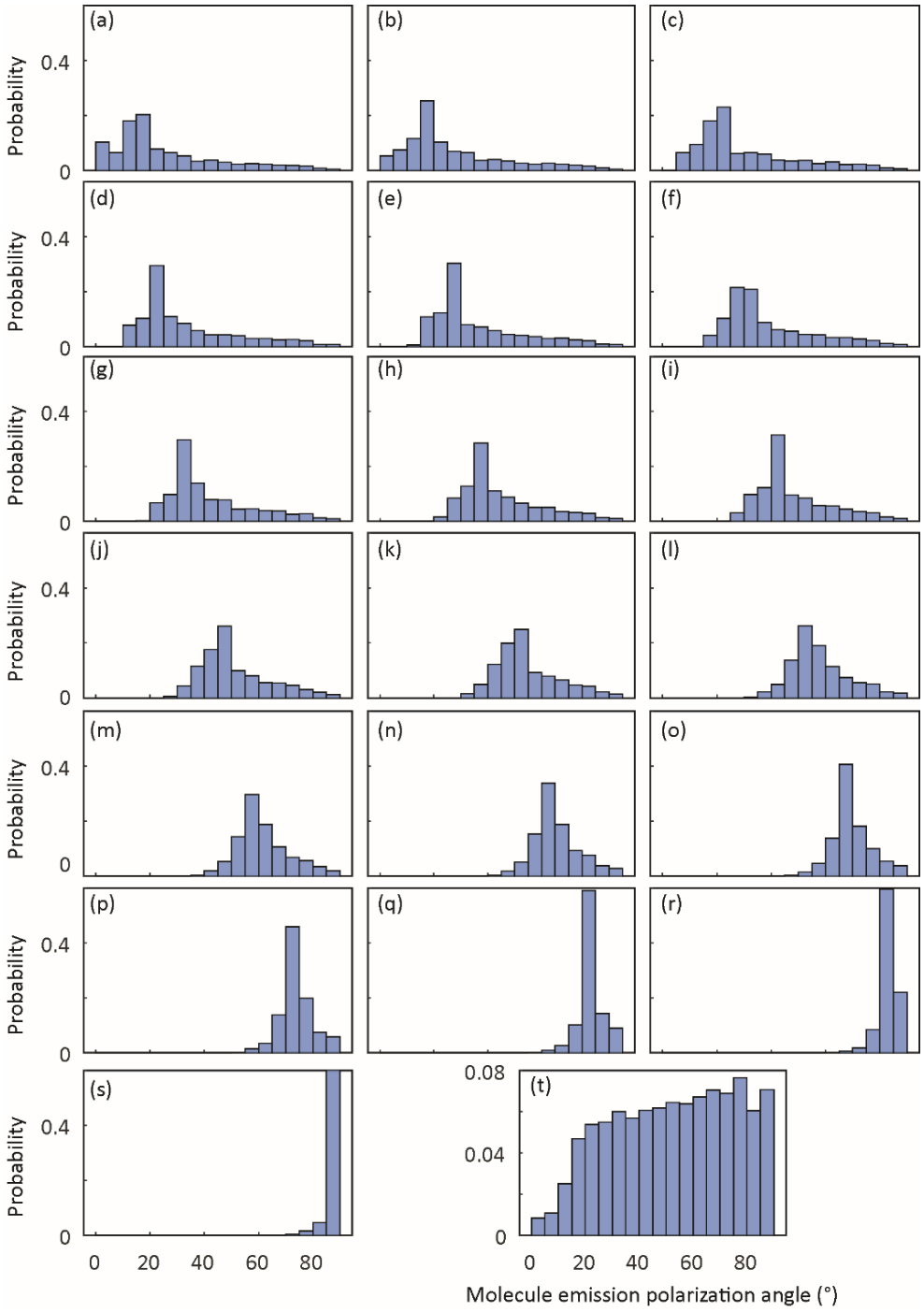

Figure 2.8: **Apparent emission polarization distributions of simulated 700-nm wavelength dipoles.** Apparent emission polarization distributions of simulated 700-nm wavelength dipoles around a nanorod oriented at 90° generated according to the "Modeling the Apparent Emission Polarization" section in the main text Methods. (a) - (s) show the histograms for dipole orientations from 0° to 90° spaced by 5°. For an example, panel (a) is the apparent emission polarization distribution of dipoles oriented at 0° and (b) is the distribution of dipoles oriented at 5°. Panel (t) provides the sum of panels (a) - (s).

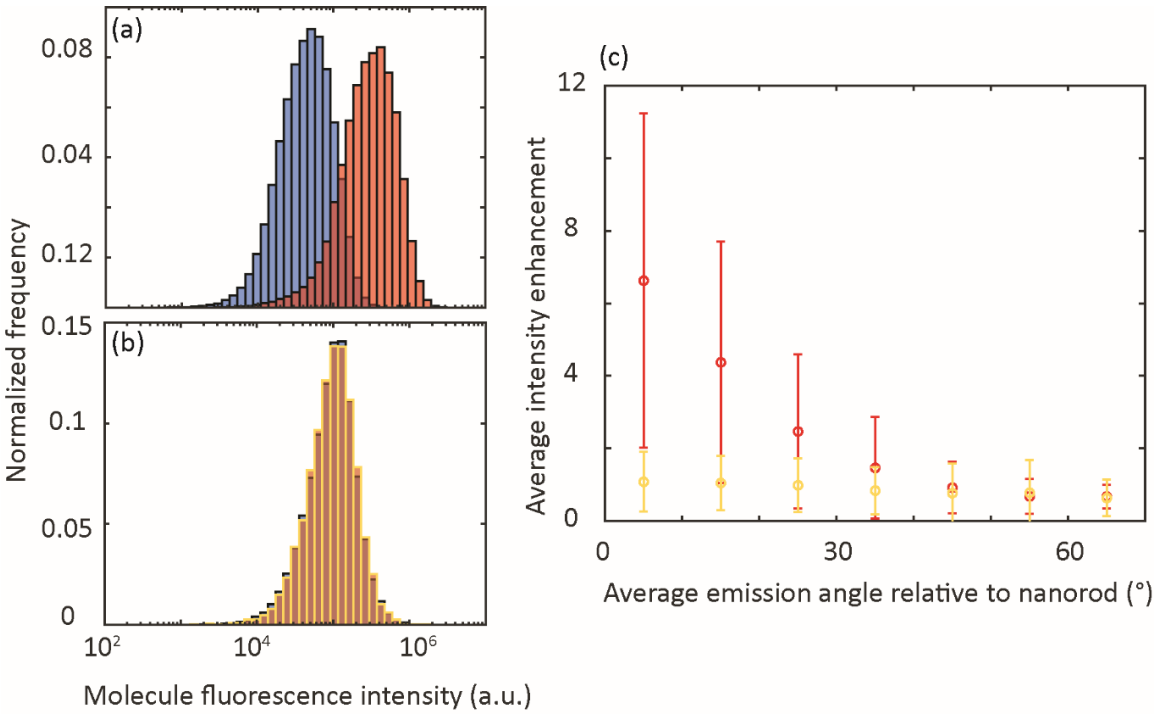

Figure 2.9: **Relation between emission enhancement and emission polarization.** (a, b) Normalized frequency distribution of single-molecule fluorescence intensities (counts detected per 100 ms imaging frame) of Cy5.5 and Cy3 molecules, respectively. (a) Red: On-nanorod Cy5.5,blue: Off-nanorod Cy5.5. (b) Yellow: On-nanorod Cy3,blue: Off-nanorod Cy3. (c) Average fluorescence enhancement vs. On-nanorod emission polarization angles (relative to nanorod scattering angle). The enhancement factor is defined as the ratio of the mean intensities of On-nanorod molecules and the mean intensities of Off-nanorod molecules, which are located between 400 nm and 700 nm away from the nanorod (red: Cy5.5; yellow: Cy3). On average, a 2-fold enhancement is observed for coupled Cy5.5 molecules with both excitation and emission spectra overlapping the nanoantenna scattering spectrum (panel a), whereas no obvious enhancement is shown for weakly coupled Cy3 molecules (panel b) as neither the excitation nor the emission is co-resonant with the plasmonic nanoantenna. For strongly coupled Cy5.5, the greatest enhancement is observed when $\phi_{apparent}$ is aligned to the nanoantenna LSPR, and the enhancement decreases as the $\phi_{apparent}$ rotates away from the nanorod longitudinal axis (panel c red). On the other hand, this emission polarization-dependent enhancement is not observed in the weakly coupled Cy3 case, in which the average enhancement is near unity for all polarization angles (panel c, yellow).

2.3.3 Polarization-sensitive detection of off-resonance molecular emission

As a control experiment, we investigated the single-molecule polarization of Cy3 molecules. Off-nanorod Cy3 molecules also appear to adsorb on the coverslip surface without preferred orientation, based on their $\phi_{apparent}$ distribution that peaks at 45° (Fig. 2.3d). Even in this off-resonance case, the On-nanorod polarization angle distributions are shifted away from the 45° peak (dashed lines in Fig. 2.3e-f) and toward the nanorod orientation (black arrows in Fig. 2.3e-f). For instance, the nanorod aligned at 25° in Fig. 2.3e shifts the distribution to the left relative to 45° and the nanorod aligned at 74° in Fig. 2.3f shifts the distribution to the right of 45°. The dark-field scattering spectra and relative angles of the nanorods are given in Fig. 2.10 and the full set of polarization distributions is given in Fig. 2.11. Interestingly, though the Cy3 spectrum is significantly detuned from the longitudinal LSP mode of the nanorod (Fig. 2.3b), the emission polarization rotates in the direction of the much stronger longitudinal mode. Still, this coupling is much weaker than that observed for the resonantly coupled Cy5.5 molecules. Thus, we characterize the shift by calculating the skewness of the polarization distributions: Fig. 2.3e shows a positively skewed distribution and the Fig. 2.3f distribution has a negative skewness. In Fig. 2.3h, the skewness from Cy3 emission polarization distributions for all 21 nanorod orientations is compared to the nanorod longitudinal axis orientation. There is a strong negative linear correlation between skewness and nanorod orientation (Pearson's correlation coefficient = -0.74, p-value = 0.0001). Even in this off-resonant coupling, the longitudinal nanorod LSP mode modifies the Cy3 emission polarization. This observation is consistent with simulation (Fig. 2.12). Accordingly, no obvious fluorescence enhancement is found for On-nanorod Cy3 (Fig. 2.9).

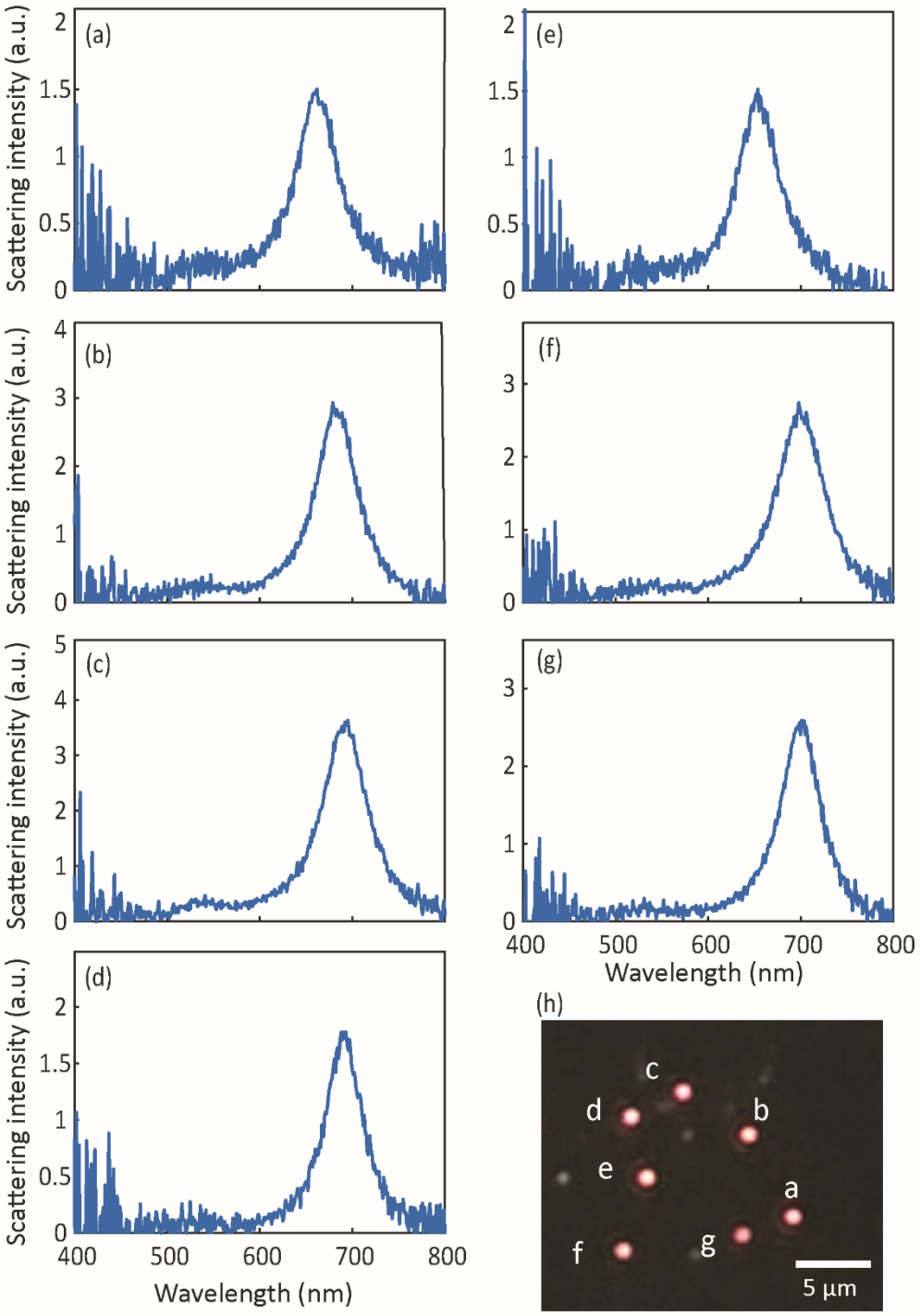

Figure 2.10: **Dark-field spectra of nanorods used in Cy3 experiment.** (a-g) Dark-field scattering spectra of the seven nanorods used for Cy3 single-molecule polarization-resolved microscopy. (h) Dark-field image of those seven nanorods (red dots). The initial orientations of the seven nanorods are: 73°, 26°, 67°, 40°, 32°, 30°, and 24°, respectively.

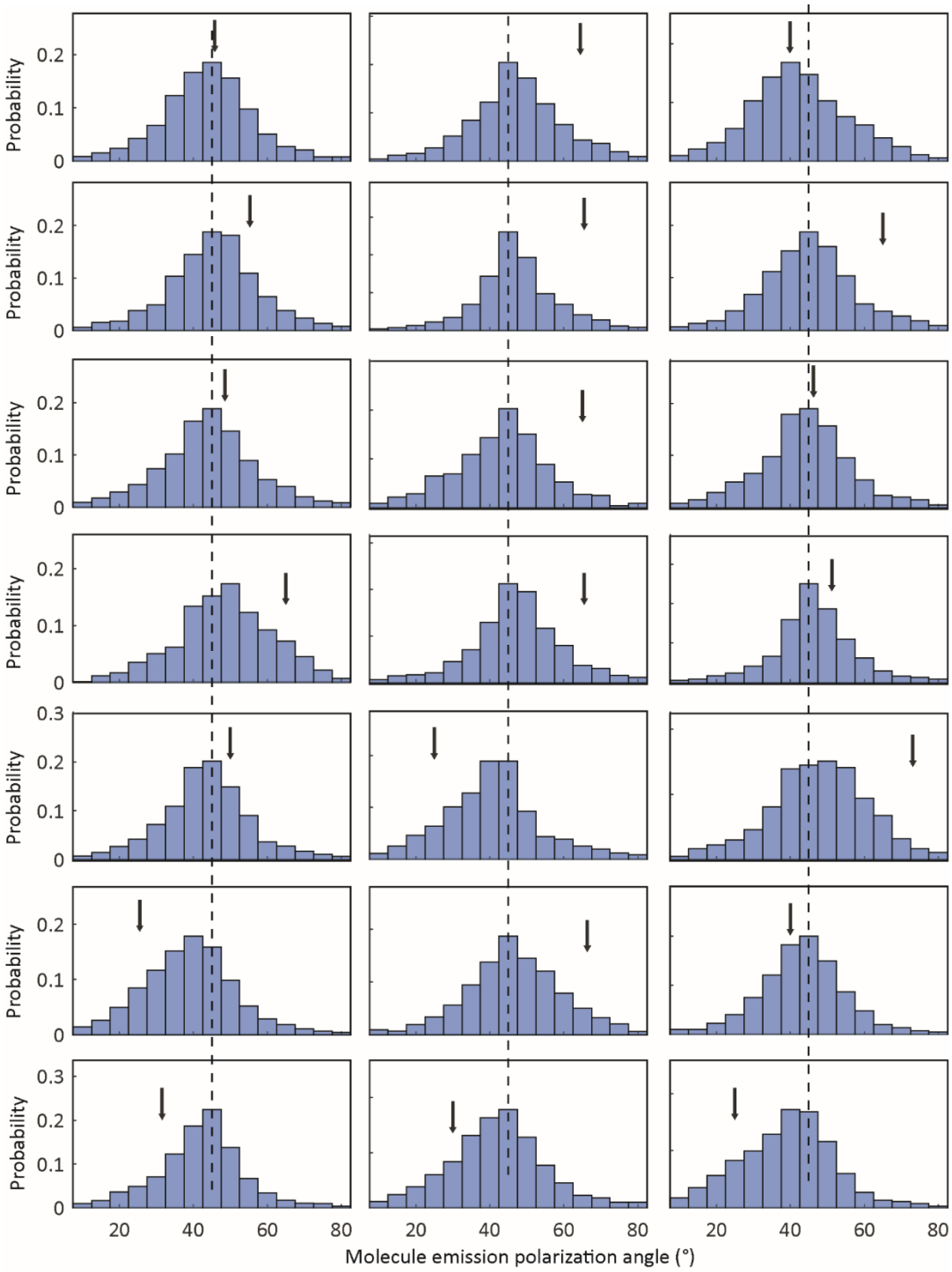

Figure 2.11: **Relation between emission enhancement and emission polarization.** Emission polarization angle of On-nanorod Cy3 single molecules from all 21 experiments. Black arrow in each sub plot indicates the apparent emission polarization angle of a nanorod. The vertical dashed lines are at 45 degrees. Each histogram collects the apparent emission polarization angles of 2,000 - 6,000 single molecules.

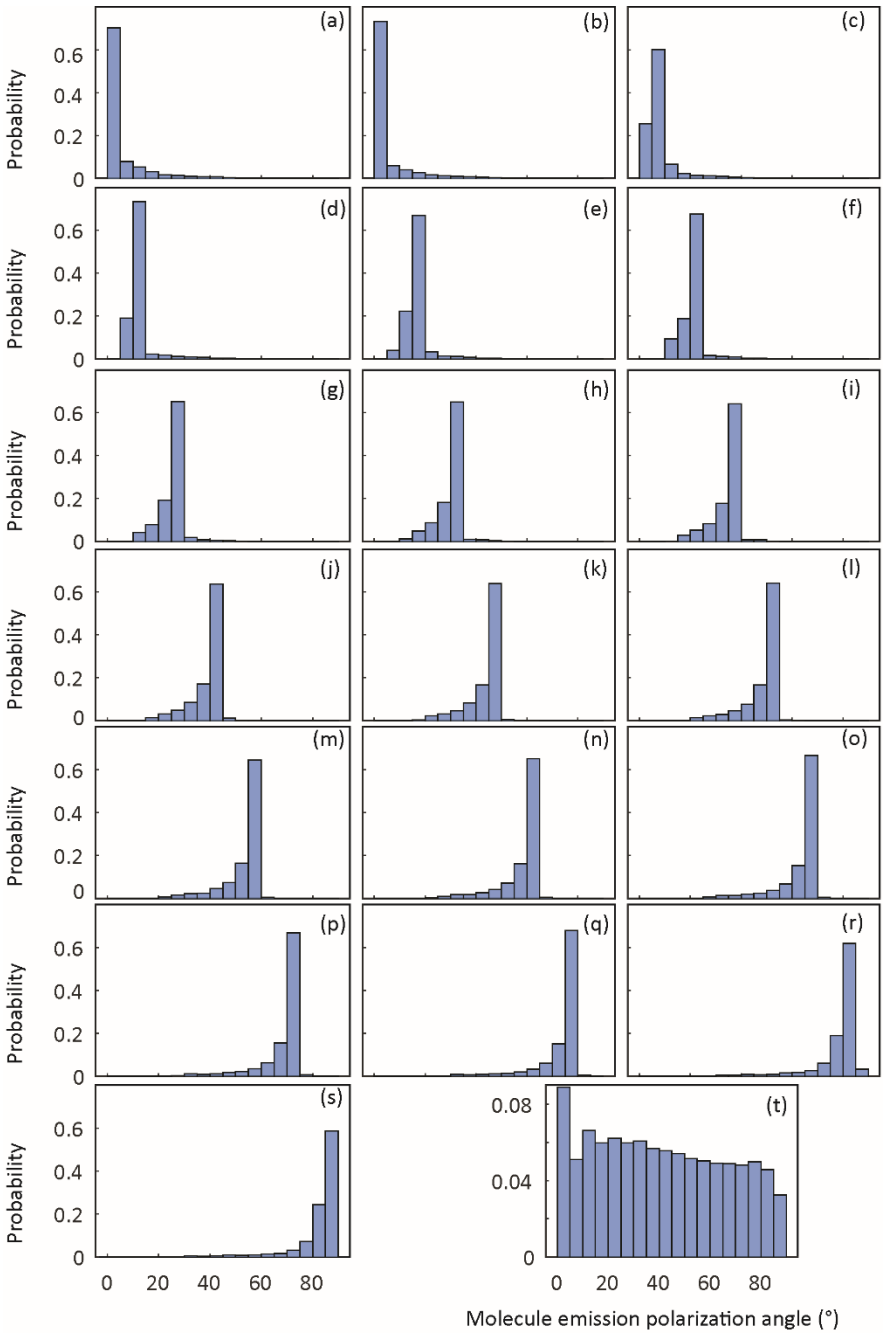

Figure 2.12: **Apparent emission polarization distributions of simulated 560-nm wavelength dipoles.** Apparent emission polarization distributions of simulated 560-nm wavelength dipoles around a nanorod oriented at 90° generated according to the "Modeling the Apparent Emission Polarization" section in the main text Methods. (a)-(s) show the histograms for dipole orientations from 0° to 90° spaced by 5°. For an example, panel (a) is the apparent emission polarization distribution of dipoles oriented at 0° and (b) is the distribution of dipoles oriented at 5°. Panel (t) provides the sum of panels (a)-(s).

2.4 Analytical model

2.4.1 Coupled dipole interaction model

Because the true location and orientation of individual molecules are obscured by plasmon coupling and the interference of emitted or scattered fields, current experiments are unable to relate these effects to the configuration-dependent interaction between molecule and plasmonic nanorod. We therefore turn to a simple analytical model of both the near-field interaction and far-field radiative emission to elucidate the essential details [61, 73]. The fluorescence emission from the coupled molecule and nanorod is attributed to two electric dipoles interacting and radiating into the far field. For justification, it is well known that plasmonic nanoparticles behave as polarizable point dipoles in the long-wavelength limit. This condition holds even under excitation from a nearby molecule at separations outside the region of fluorescence quenching [63]. At a particular oscillator frequency, electric dipoles can be described as linearly proportional to the total field at their location excluding their own field. For the molecule's emissive transition dipole moment (labeled $\mathbf{p}_0$) and dipole plasmon induced in the nanoparticle (labeled $\mathbf{p}_1$), the dipole magnitudes, phases and orientations must satisfy the following coupled equations for the complex vectors:

$$\mathbf{p}_0 = \boldsymbol{\alpha}_0 \left[\mathbf{E}_1(\mathbf{x}_0) + \mathbf{E}_F\right] \tag{2.2}$$

$$\mathbf{p}_1 = \boldsymbol{\alpha}_1 \mathbf{E}_0(\mathbf{x}_1) \tag{2.3}$$

where the dipoles, linear polarizabilities α_i, and fields are all evaluated at the frequency ω and the inner product is implied by neighboring tensors in boldface. The fields $\mathbf{E}_i(\mathbf{x}_j) = \mathbf{G}(\mathbf{x}_i, \mathbf{x}_j) \cdot \mathbf{p}_i$ are the classical oscillating dipole fields generated by the ith dipole at the

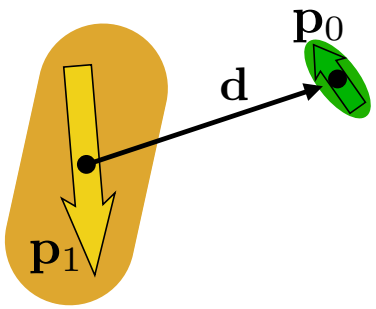

Figure 2.13: **Two coupled dipoles.** Diagram of two coupled dipoles and separation vector $\mathbf{d} = d\hat{d} = \mathbf{x}_1 - \mathbf{x}_0$.

location of the jth dipole defined in terms of the tensor [83]:

$$\mathbf{G}(\mathbf{d}) = \left[\left(3\hat{d}\hat{d} - \mathbf{1}\right)\left(\frac{1}{d^3} - \frac{ik}{d^2}\right) - \left(\hat{d}\hat{d} - \mathbf{1}\right)\frac{k^2}{d}\right] e^{ikd}, \tag{2.4}$$

which relays the dipole field from the dipole location $\mathbf{x}_i$ to another point $\mathbf{x}_j$. The separation vector $\mathbf{d} = d\hat{d} = \mathbf{x}_1 - \mathbf{x}_0$ defines the separation between the molecule and centroid of the plasmonic nanorod (Fig. 2.4.1). The fictitious harmonic field $\mathbf{E}_F = E_0\hat{e}_x e^{-i\omega t}$ driving only the molecule dipole forces the dipoles to oscillate harmonically and represents the continuous population of the emissive state by absorption of the real excitation field and subsequent vibrational relaxation characteristic of fluorescence.

Since the coupled dipole equations are linear, both dipoles will oscillate at the frequency ω, which can be thought of as a single Fourier component of the coupled fluorescence emission spectrum. To simplify analysis, we will take ω to be the resonance maximum in the uncoupled molecule's emission spectrum and will demonstrate that this single-color model approximates the character of the multicolor images collected experimentally. The governing dynamical equations for the dipole moments can then be solved

to yield the dipole moments:

$$\begin{cases} \mathbf{p}_0 = \left[\mathbf{1} - \boldsymbol{\alpha}_1 \mathbf{G}(\mathbf{x}_1, \mathbf{x}_0)\boldsymbol{\alpha}_0 \mathbf{G}(\mathbf{x}_0, \mathbf{x}_1)\right]^{-1} \boldsymbol{\alpha}_0 \mathbf{E}_F \\ \mathbf{p}_1 = \boldsymbol{\alpha}_1 \mathbf{G}(\mathbf{x}_1, \mathbf{x}_0)\mathbf{p}_0 \end{cases} \tag{2.5}$$

and the indirectly driven plasmon dipole becomes,

$$\mathbf{p}_1 = \boldsymbol{\alpha}_1 \mathbf{G}(\mathbf{x}_1, \mathbf{x}_0)\mathbf{p}_0 \tag{2.6a}$$

$$= \boldsymbol{\alpha}_1 \mathbf{G}(\mathbf{x}_1, \mathbf{x}_0)\boldsymbol{\alpha}_0[\mathbf{E}_F(\mathbf{x}_0) + \mathbf{E}_1(\mathbf{x}_0)] \tag{2.6b}$$

$$= \boldsymbol{\alpha}_1 \mathbf{G}(\mathbf{x}_1, \mathbf{x}_0)\boldsymbol{\alpha}_0[\mathbf{E}_F(\mathbf{x}_0) + \mathbf{G}(\mathbf{x}_0, \mathbf{x}_1)\mathbf{p}_1] \tag{2.6c}$$

$$= \boldsymbol{\alpha}_1\boldsymbol{\alpha}_1 \mathbf{G}(\mathbf{x}_1, \mathbf{x}_0)\boldsymbol{\alpha}_0 \mathbf{E}_F(\mathbf{x}_0) + \boldsymbol{\alpha}_1 \mathbf{G}(\mathbf{x}_1, \mathbf{x}_0)\boldsymbol{\alpha}_0 \mathbf{G}(\mathbf{x}_0, \mathbf{x}_1)\mathbf{p}_1 \tag{2.6d}$$

$$= \left(\mathbf{1} - \boldsymbol{\alpha}_1 \mathbf{G}(\mathbf{x}_1, \mathbf{x}_0)\boldsymbol{\alpha}_0 \mathbf{G}(\mathbf{x}_0, \mathbf{x}_1)\right)^{-1} \boldsymbol{\alpha}_1 \mathbf{G}(\mathbf{x}_1, \mathbf{x}_0)\boldsymbol{\alpha}_0 \mathbf{E}_F(\mathbf{x}_0). \tag{2.6e}$$

where the dipole field is relayed from the dipole location $\mathbf{x}_i$ to the point $\mathbf{x}_j$ by the tensor

$$\mathbf{G}(\mathbf{d}) = \left[\left(3\hat{d}\hat{d} - \mathbf{1}\right)\left(\frac{1}{d^3} - \frac{ik}{d^2}\right) - \left(\hat{d}\hat{d} - \mathbf{1}\right)\frac{k^2}{d}\right] e^{ikd}. \tag{2.7}$$

With the model, the effects of the nanorod longitudinal and transverse dipolar localized surface plasmon (LSP) modes are independently studied for molecules at specified locations and orientations. The individual influence of each mode on the observed mispolarization can then be explicitly isolated, along with its dependence on interference effects.

With an analytical relationship between the two dipole moments, the dyadic polarizabilities can be parameterized from spectra of the uncoupled molecules and nanorod. For this purpose, the molecule emissive dipole transition is modeled by a Lorentz oscillator polarizable only in one direction fixed by the molecular orientation; i.e., $\alpha_0 = \hat{\mathbf{e}}_\mathbf{x}\alpha_{mol}\hat{\mathbf{e}}_\mathbf{x}$ in the reference frame of the molecule. The nanorod is approximated as a prolate spheroid in the modified long-wavelength approximation [84], with polarizability $\alpha_1 = \hat{\mathbf{e}}_{\mathbf{x}'}\alpha_{short}\hat{\mathbf{e}}_{\mathbf{x}'} + \hat{\mathbf{e}}_{\mathbf{y}'}\alpha_{long}\hat{\mathbf{e}}_{\mathbf{y}'} + \hat{\mathbf{e}}_{\mathbf{z}'}\alpha_{short}\hat{\mathbf{e}}_{\mathbf{z}'}$ in the basis aligned with the nanorod principal

axes. The prolate spheroid geometry idealizes the true nanorod geometry to allow for a closed form solution to Maxwell's equations including radiation damping for the dipolar LSPs. Both components of α_1 are parameterized by the two unique semi-radii of the cylindrical nanorod (here 44 nm and 20 nm) and three material parameters built into the Drude model dielectric function describing the electronic responses of bulk gold (See Sec. 2.6 for details of nanorod paramaterization).

To compute the two-channel diffraction-limited images generated by the polarizing beam displacer (PBD), the fields emitted by the coupled dipoles in Eq. 2.4.1 and Eq. 2.4.1 are propagated through an idealized microscope. The resulting image contains the superposition of the focused and diffraction-limited fields, $\mathbf{E_0^{im}}$ and $\mathbf{E_1^{im}}$, which are proportional to each dipole moment respectively (see Sec. 2.6 for more detail). In accordance with our experiment, orthogonal polarization components of the total field are split to form separate images, each with the form:

$$I_q = \frac{cn}{8\pi} \left| \left(\mathbf{E_0^{im}} \cdot \hat{\mathbf{e}}_\mathbf{q} \right|^2 + \mathbf{E_1^{im}} \cdot \hat{\mathbf{e}}_\mathbf{q} \right|^2 + 2\mathrm{Re}\left[\mathbf{E_0^{im}} \cdot \hat{\mathbf{e}}_\mathbf{q} \mathbf{E_1^{im}} \cdot \hat{\mathbf{e}}_\mathbf{q} \right] \Big) \tag{2.8}$$

where $q \in \{x, y\}$ are analogous to the center and off-center experimental image channels, c is the speed of light in vacuum, and n is the refractive index of the background medium (here water). Combining this polarized image intensity with Eq. 2.3.1 makes explicit how the average emission polarization measured in experiment is determined by the orientation-dependent relay tensor G that influences the dipole moment magnitudes and phases according to Eq. 2.4.1 and Eq. 2.4.1. The polarizabilities in the latter equations are parametrized from the independent dye emission and nanorod scattering spectra. By assuming the nanorod location and orientation are determined, Eq. 3.2 provides an analytical measure of the imaged intensities and observed polarization as a function of molecule position and orientation.

2.4.2 Analysis of the isolated contributions from the transverse and longitudinal LSP modes and interference

By manually setting the short- or long-axis components of the nanorod polarizability to zero in the model, the independent contributions of the transverse and longitudinal LSP modes on $\phi_{apparent}$ can be studied. As in the experiments, $\phi_{apparent}$ (Eq. 2.3.1) maps onto an angle range slightly smaller than 0-90° due to the inherent cross-talk. In both the analytical model and the simulations, the calculated polarization is mapped back onto a 0 - 90° range by inverting the one-to-one mapping between the true dipole orientation in plane and $\phi_{apparent}$ (Fig. 2.2). To determine how interference affects the PBD-resolved emission polarization [62], we also compare the full emission polarization with that produced by the isolated plasmon modes in the absence of the interference term in Eq. 3.2. Four geometries are studied: 0°-oriented molecular dipoles analogous to Cy5.5 (i.e., parallel to and resonant with the longitudinal LSP mode), 0°-oriented molecular dipoles analogous to Cy3 (i.e., parallel to and off resonance with the longitudinal LSP mode), 90°-oriented dipoles analogous to Cy5.5 (i.e., perpendicular to and resonant with the longitudinal LSP mode), and 90°-oriented dipoles analogous to Cy3 (i.e., perpendicular to and off resonance with the longitudinal LSP mode); Fig. 2.15-Fig. 2.18.

The most significant mispolarization is shown in the configuration of the 0°-oriented molecular dipoles resonant with the longitudinal LSP (Fig. 2.4.2a).

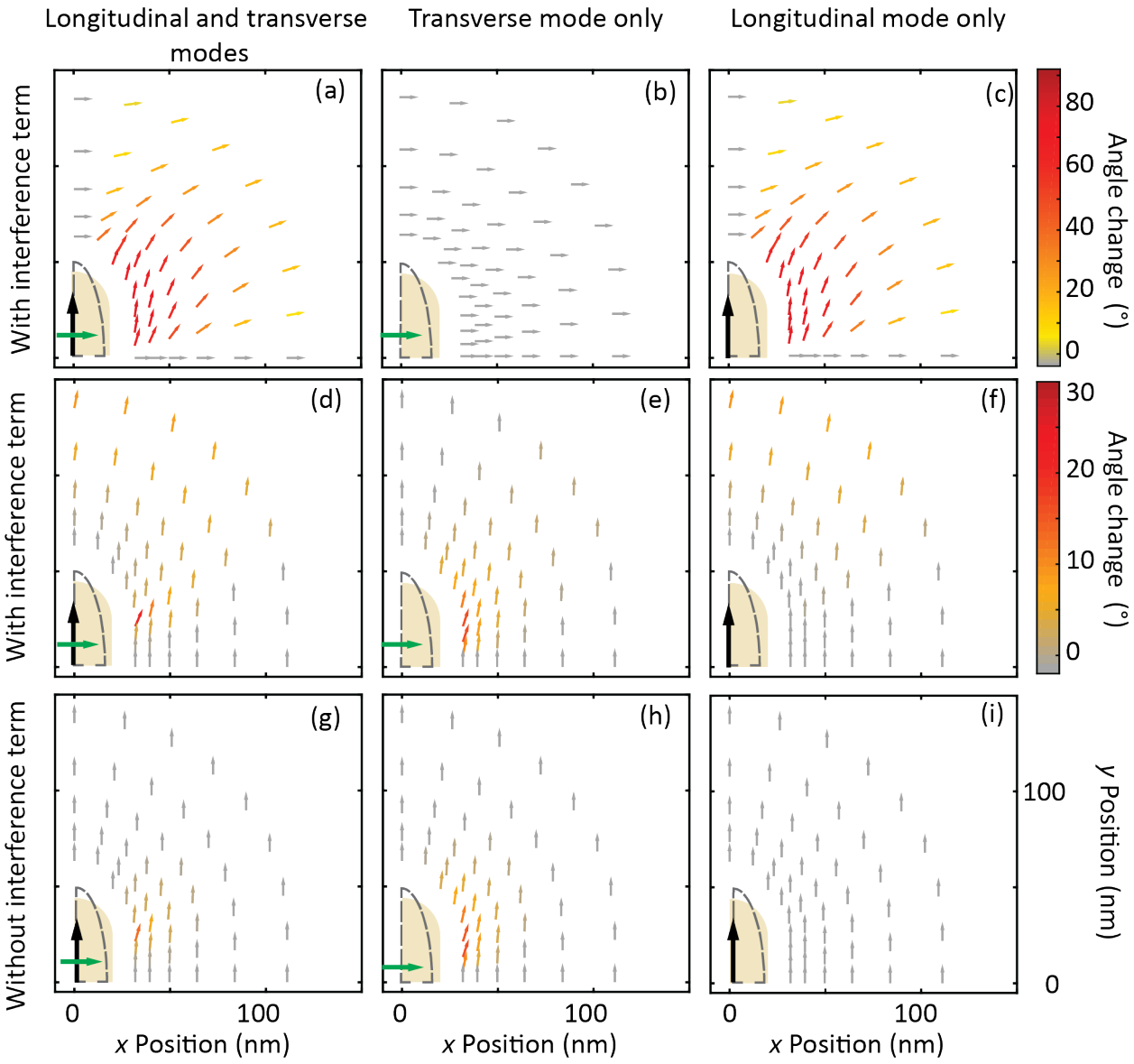

Figure 2.14: **Mispolarization map calculated from the coupled-dipole model.** (a)-(c) $\phi_{apparent}$ maps corresponding to 0°-oriented molecular dipoles resonant with the longitudinal LSP. (d)-(i) $\phi_{apparent}$ maps corresponding to 90°-oriented molecular dipoles that are also resonant with the longitudinal LSP. The black and green arrows indicate the longitudinal and transverse LSP modes, respectively, of the nanorod. The tan shapes in (a)-(i) show a quarter of the simulated nanorod. The black dashed outline shows the prolate spheroid model of the nanorod (best fit geometric and material parameters are given in Sec. 2.6).

Fig. 2.4.2b-c shows the decomposition of the $\phi_{apparent}$ of these molecules by projecting onto either the transverse or longitudinal LSP modes in isolation. Comparing among the panels in Fig. 2.4.2, it is clear that the experimentally measured skew of molecule emission polarization toward the nanorod long axis displayed in Fig. 2.3 is mostly due to superposition of the longitudinal plasmon mode scattering with the molecular emission. Molecules not aligned with the main nanorod axis still couple to and drive the long-axis dipole plasmon, which emits mostly light polarized along its axis and biases the average polarization across an image in its favor. However, similar polarization maps for 90°-oriented dipoles resonant with the longitudinal LSP (Fig. 2.4.2d-i) show that the influence of the longitudinal LSP upon $\phi_{apparent}$ is more complicated: as in the case for 0° orientation, the longitudinal LSP strongly mispolarizes the molecular emission toward the longitudinal LSP mode (aligned along the y-axis) by superposition with fluorescence emission redirected through the plasmon (Fig. 2.4.2d-f); additionally, for the 90° case, the longitudinal LSP mode mispolarizes dipoles that are parallel to y-axis toward the transverse mode axis (aligned along the x-axis) orientation because of destructive interference effects in the y-oriented fields (Fig. 2.4.2g-i). This interference effect results from the far-fields of the molecule and nanorod that are parallel to their dipole moments being out of phase, thereby turning the last term in Eq. 3.2 negative for both components, which reduces the argument of the arctangent in Eq. 2.3.1 and therefore reduces the observed polarization angle below 90°. The transverse plasmon mode produces mispolarization of 90° molecules close in proximity to its dipole moment by superposition similar to how the longitudinal mode mispolarizes x-oriented molecules. However, as the electric field of the transverse mode is much weaker than that of the longitudinal mode, the transverse mode does not change the polarization as much as the longitudinal mode even for resonant molecules (Fig. 2.17).

With other geometries, we can compare the model with simulations and evaluate the contributions from each mode using the same approach mentioned above. Here we listed

the four different geometries we studied for your reference. In these figures, panel a are apparent emission polarizations from electrodynamics simulation. In the simulations, the simulated dipoles were placed directly on the glass substrate (Fig. 2.10), whereas in the analytical model they were placed in the plane bisecting the nanorod, which may account for small differences between simulated and model emission polarizations. To avoid the regime of fluorescence quenching, no dipoles were placed within 10 nm from the edge of the nanorod in both the analytical calculation and simulation. The colored arrows show the position and apparent polarization of each dipole. The color bar shows the change of the polarization angle from the original ones, which in this case is 0°. b - g are the apparent emission polarization map of the dipoles calculated from analytical model under the same configuration as the simulation. The large black and green arrows in b - g indicate the longitudinal and transverse mode of nanorod in the analytical model, respectively. The gold shapes in a - g shows a quarter of a nanorod. The black dashed line in b - g shows the prolate spheroid used in the analytical model. e - g are produced by the isolated plasmon modes with the polarizations calculated in absence of the interference term in Eq. 3.2, such that $|\mathbf{E_0} \cdot \hat{\mathbf{e}}_\mathbf{q} + \mathbf{E_1} \cdot \hat{\mathbf{e}}_\mathbf{q}|^2 \rightarrow |\mathbf{E_0} \cdot \hat{\mathbf{e}}_\mathbf{q}|^2 + |\mathbf{E_1} \cdot \hat{\mathbf{e}}_\mathbf{q}|^2$, leaving only the superposition of polarized images from each dipole. By comparing plane a and b of each figures, we can see that the simulation agrees well with the model results containing the physical effects of both dipolar plasmon modes and far-field interference.

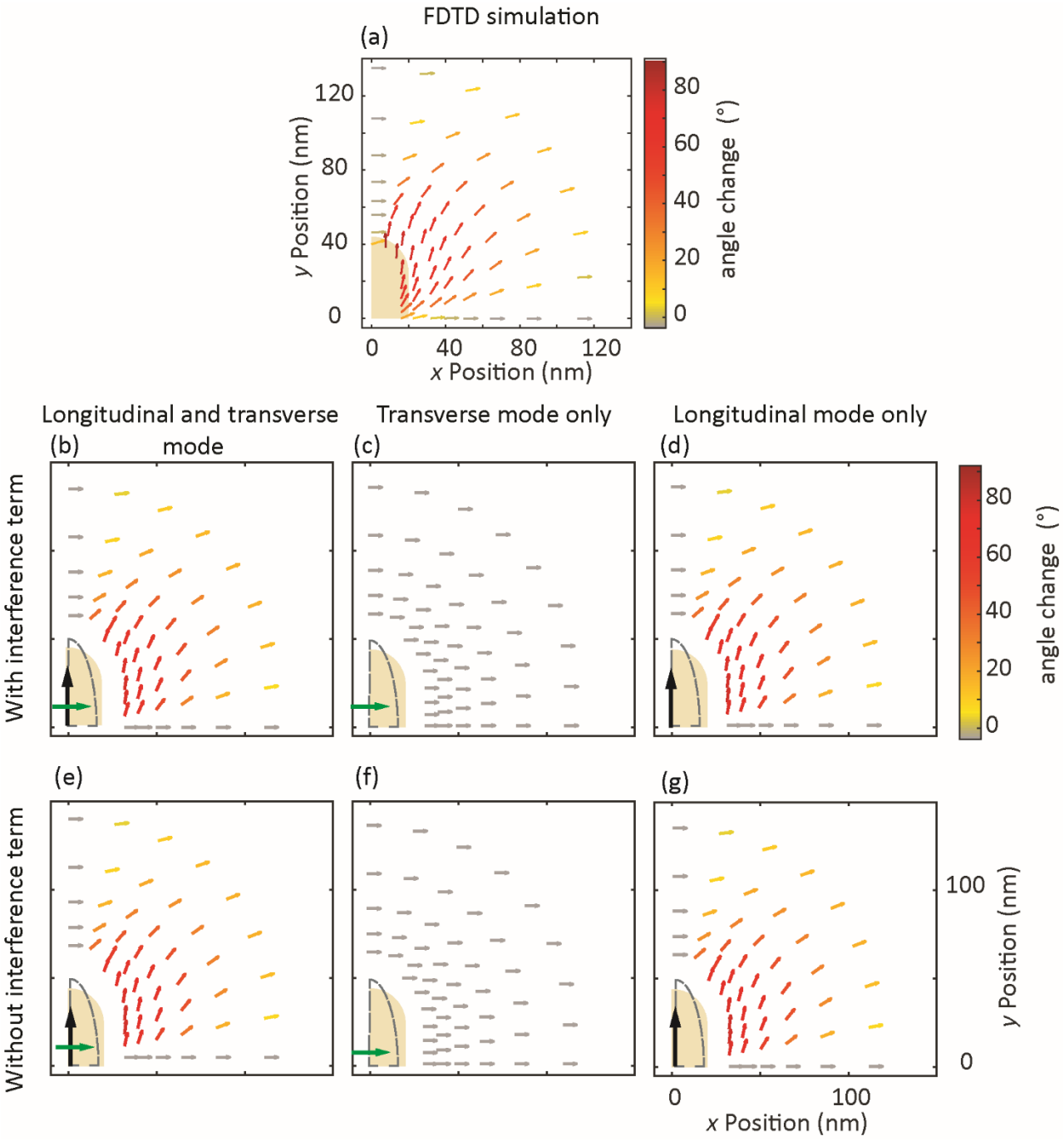

Figure 2.15: **Model evaluation geometry 1.** Dipoles resonant with the simulated nanorod longitudinal mode (700 nm) but aligned with the transverse mode of the nanorod (0°).

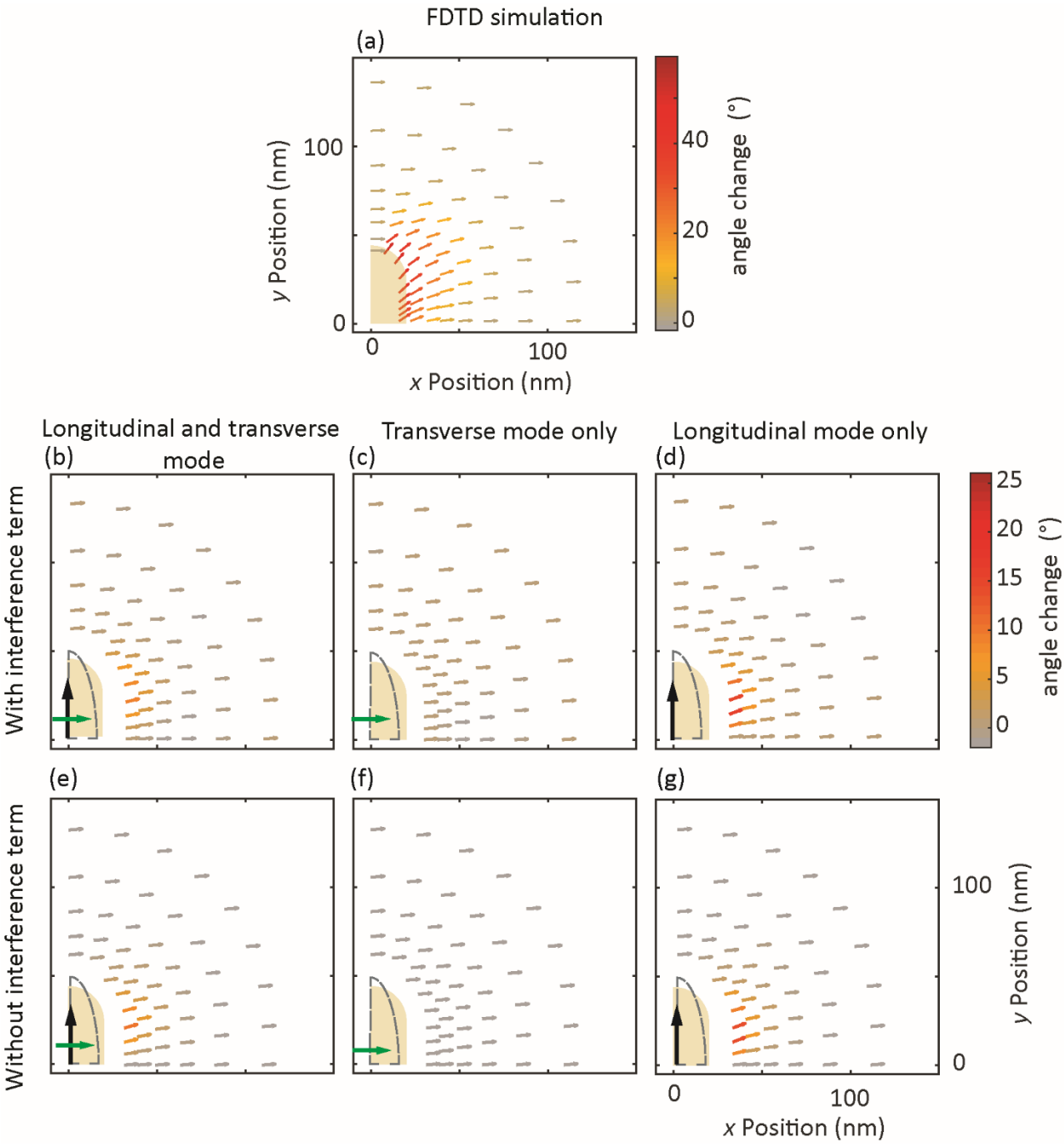

Figure 2.16: **Model evaluation geometry 2.** Dipoles resonant with the simulated nanorod transverse mode (560 nm) but aligned with the transverse mode of the nanorod (0°).

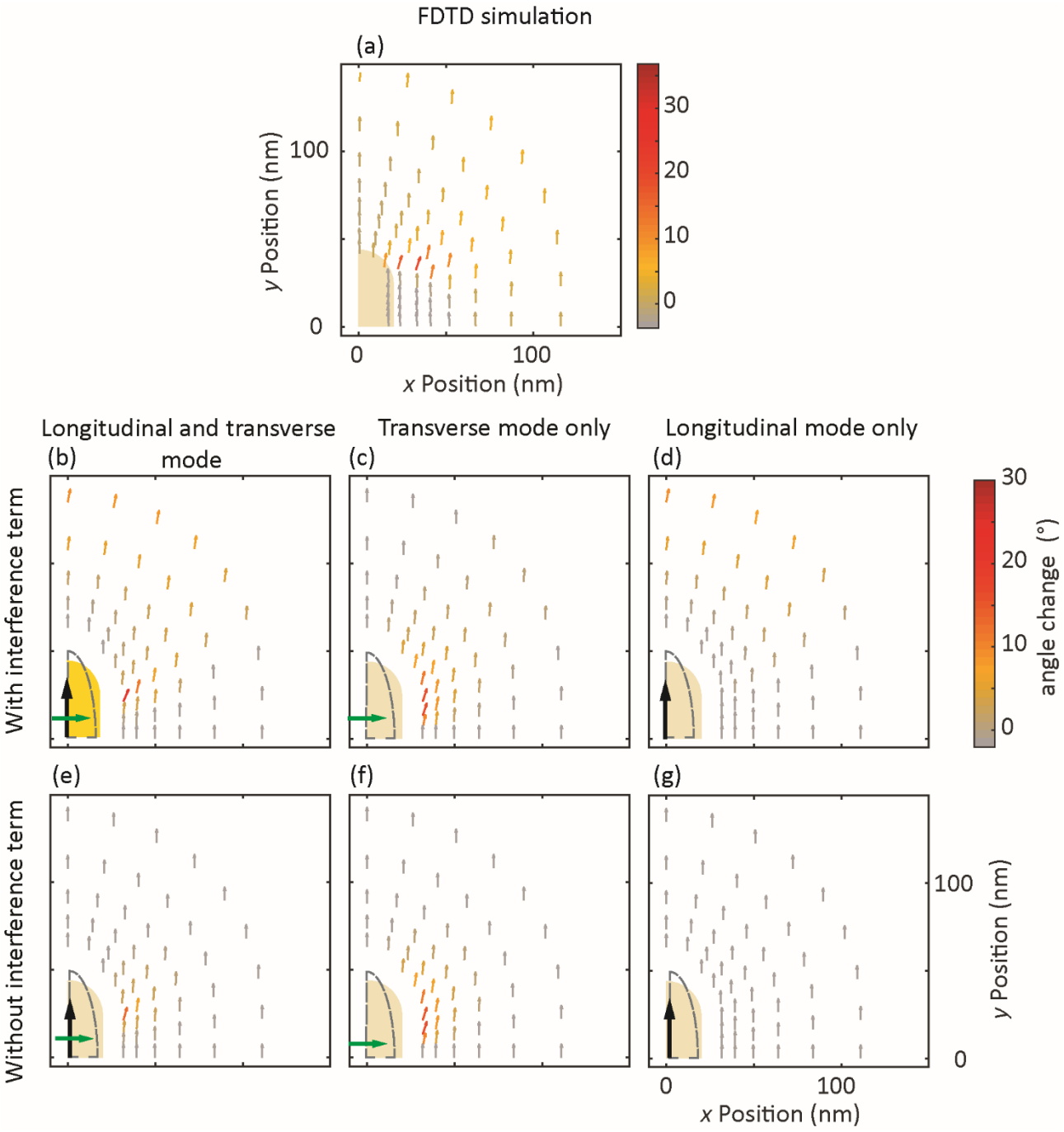

Figure 2.17: **Model evaluation geometry 3.** Dipoles resonant with the simulated nanorod longitudinal mode (700 nm) but aligned with the longitudinal mode of the nanorod (90°).

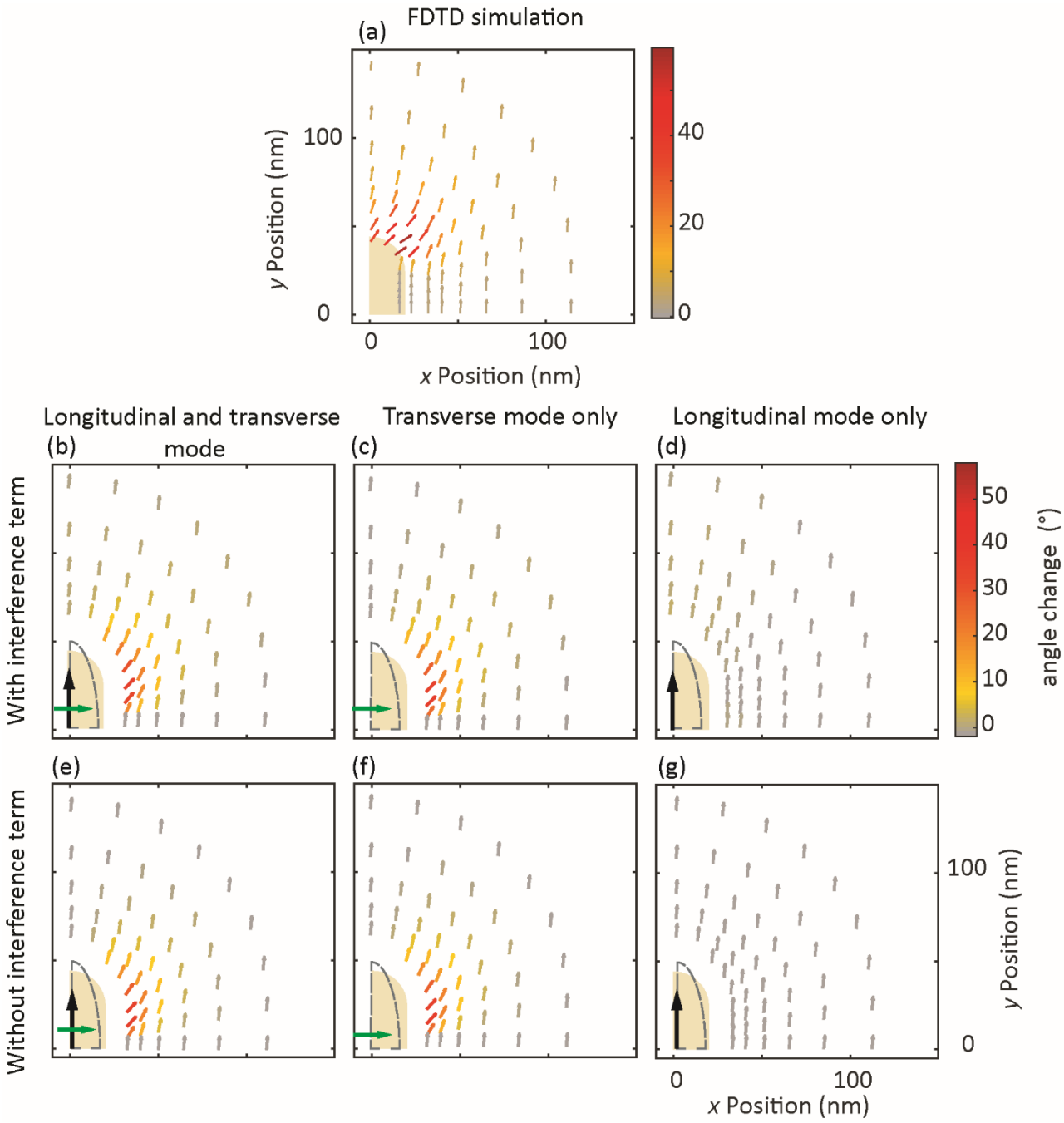

Figure 2.18: **Model evaluation geometry 4.** Dipoles resonant with the simulated nanorod transverse mode (560 nm) but aligned with the longitudinal mode of the nanorod (90°).

2.5 Conclusion

In conclusion, using high-throughput single-molecule polarization-resolved microscopy, we have discovered that emission polarization is a measure of the coupling strength between molecular emitters and plasmonic nanoantennas. The stronger the coupling of the molecule to a plasmonic nanoantenna, the more the molecule emission polarization will rotate toward the polarization of the nanoantenna LSP mode. While this effect is apparent for an ensemble of single molecule measurements, simulations and analytical modeling demonstrate that the mispolarization of single molecules with known location and orientation is much more complicated. $\phi_{apparent}$ is rotated both toward and away from the nanorod long-axis by two distinct physical phenomena, even for molecules that are resonant with the nanorod longitudinal LSP mode. Either constructive or destructive interference can dominate depending on the molecule orientation and location relative to the nanorod. Significantly, the emission polarization is a more sensitive measure of coupling than fluorescent intensity enhancement because, even for weakly coupled Cy3 where no apparent fluorescent enhancement is observed, the emission polarization change is appreciable. Future work will use this model fit to extract the true molecule location and orientation from experimental images.

2.6 Methods

2.6.1 Gold nanorod samples

Nanorods (40 nm diameter, 92 nm length, A12-40-700 NRs) were purchased from Nanopartz Inc. (Loveland, CO) and used as received. To prepare the nanorod substrate, 5 μL 50-fold diluted nanorods (5 μL nanorod stock solution + 245 μL DDI water) were drop-cast on a microscope coverslip for 5 min. The sample was then washed under DDI water for 3 mins to wash away those nanorods that did not stick on the coverslip.

2.6.2 Single-nanorod dark-field scattering spectroscopy

Nanorods were immobilized on glass coverslips as described above. These nanorod substrates were immersed in water. A broadband halogen white light source excited the sample through a dark-field water-immersion condenser, and scattered light was collected in an Olympus IX71 inverted microscope equipped with a dark-field oil-immersion objective (NA = 0.6). The diffraction-limited image of a single nanorod was aligned to the entrance slit of an imaging spectrograph (Acton 2300, Princeton Instruments), and spectral data were collected on an electron multiplying charge-coupled device (EMCCD) (5 s integration time; Andor iXon). Background spectra collected from nearby positions with no nanorod on the spectrograph entrance slit were subtracted from measured spectra, and all data were divided by the broadband spectrum of the halogen light source and any additional neutral density filters to correct for the system spectral efficiency.

2.6.3 Polarization-resolved single-molecule epifluorescence microscopy

Wide-field epifluorescence microscopy was performed on nanorod substrates with a 100x 1.30 NA oil-immersion objective in an Olympus IX71 inverted microscope. A volume of 75-100 μL of 22 nM Cy5.5 NHS ester or Cy3 NHS ester dye (Lumiprobe Corporation) in water was placed on top of the nanorod substrates in a rubber O-ring that had been cleaned by sonication in acetone. Single Cy5.5 or Cy3 molecules were excited with circularly polarized 635 nm laser light (Coherent CUBE 640-40C) and 532 nm laser light (CrystaLaser CL-532-025-O) respectively. Excitation intensities were ~4 $\mu W/\mu m^2$. Fluorescence emission was filtered by passing through appropriate dichroic mirror (Di01-R640 and Di01-R532 respectively) and long-pass filter (BLP01-640R and BLP01-532R respectively) to maximize signal and minimize scattered laser light.

The emission beam then passed through a Polarizing Beam Displacer (Thorlab BD40) which separates the input beam into two orthogonally polarized output beams-Center channel and Off-center channel). These output beams were then collected on a 512 pixel

x 512 pixel Andor iXon EMCCD with beam size 450 μm^2 ea. (1 camera pixel = 160 nm in the imaging plane).

The images were recorded at 100 ms/frame to acquire emission from only those dye molecules adsorbed to the sample surface. An adsorbed molecule is sufficiently constrained by the sample surface to be observed on the imaging time scale. The adsorption rate, which is proportional to the dye concentration in solution (~10 nM in our experiments), can be controlled, ensuring that only one molecule is adsorbed at a time per diffraction-limited area. The immobilization times of adsorbed molecules is typically 100 ms - 1 s and are completely random.

2.6.4 Single-molecule intensity and emission polarization angle analysis

The SMALL-LABS algorithm was used to localize single molecules from the movies and to subtract accurate backgrounds [78]. The Off-nanorod molecules were the ones that located at least 400 nm away from any nanorods. The On-nanorod molecules were identified as those located within 120 nm to the nanorods. The local true background a certain molecule was the average intensity of the ±100 frames of that molecule frame, in which no molecules were localized in the vicinity of that molecule. This local background was then subtracted from the raw molecule image and the molecule fluorescent intensity was calculated by summing the pixel intensities over 12 x 12 image pixels (480 x 480 nm). The intensity of the intrinsic photoluminescence of nanorod is calculated in the same way as it can also be treated as a single point emitter. The Center and Off-center channels were overlaid before using SMALL-LABS to maximize the signal-to-noise ratio for single molecule detection. The intensities of molecules and nanorods were calculated in the two channels separately.

2.6.5 Electromagnetic simulations

Time-domain electromagnetic simulations were performed for supplementary analysis by using the Lumerical finite difference time domain (FDTD) Solutions software package. Nanorods were modeled as a cylinder with length = 44 nm and 40-nm diameter hemispherical caps. All simulations were performed with the nanorods immersed in water and placed on a glass slab. The total simulation volume is 3.375 μm^3; near the nanorods, a fine-mesh grid with 3.375 nm^2 cell volume was used. The nanorod geometry parameters were determined by varying the simulated size parameters (cylinder length and hemisphere radius) and matching the simulated far-field scattering spectra to the experimentally measured dark-field scattering spectra (Fig. 2.5, Fig. 2.10). Water and glass were modeled with a constant refractive index of (n = 1.333, k = 0) and (n = 1.5, k = 0), respectively. The frequency-dependent complex permittivity of Au was obtained by an analytical fit to experimental data [85].

The simulated scattering spectrum of nanorod (Fig. 2.19) was calculated by exciting the nanorod from above the water at normal angle with a broadband plane wave, which is consistent with dark-field spectroscopy experiments. Two orthogonal excitation polarizations were averaged to simulate the incoherent lamp light. The apparent polarization analysis in Fig. 2.2 and Fig. 2.4, as well as the coupled emission polarization results in Fig. 2.8 and Fig. 2.12, were obtained using a broadband point dipole source (constant current) to represent a dye molecule. To reproduce the coupled emission with dye molecules with random distances and orientations near nanorod, we simulated dipoles at different distances from the nanorod center (from 16 to 131 nm, logarithmically spaced). At each dipole position considered, simulations were run for 19 different orientations (from 0° to 90°, spaced by 5°) and a reference simulation under the same conditions but without the nanorod was run. We only considered in-plane dipoles due to the fact that out-of-plane-dipoles can be treated as the projections of in-plane dipoles. All dipoles are sampled over one quadrant corresponding to the minimum symmetry unit of the NR (Fig. 2.20). The

dipoles were placed right on top of glass slab rather than the same z plane as the center of the nanorod so some dipoles could get underneath the nanorod, which is consistent with our experimental configuration. To mimic the effect of our objective lens, the fields were monitored and recorded in a plane in the glass substrate below the dipole source.

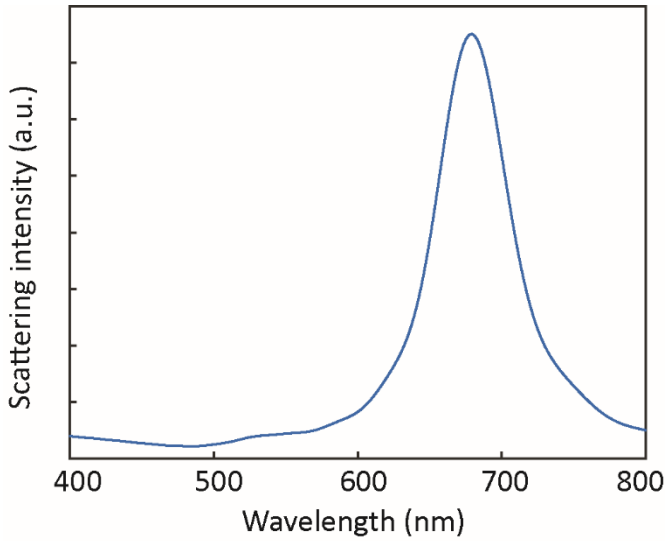

Figure 2.19: **Simulated nanorod dark-field scattering spectrum.** Nanorods were modeled as a cylinder with length = 44 nm and 40-nm diameter hemispherical caps.

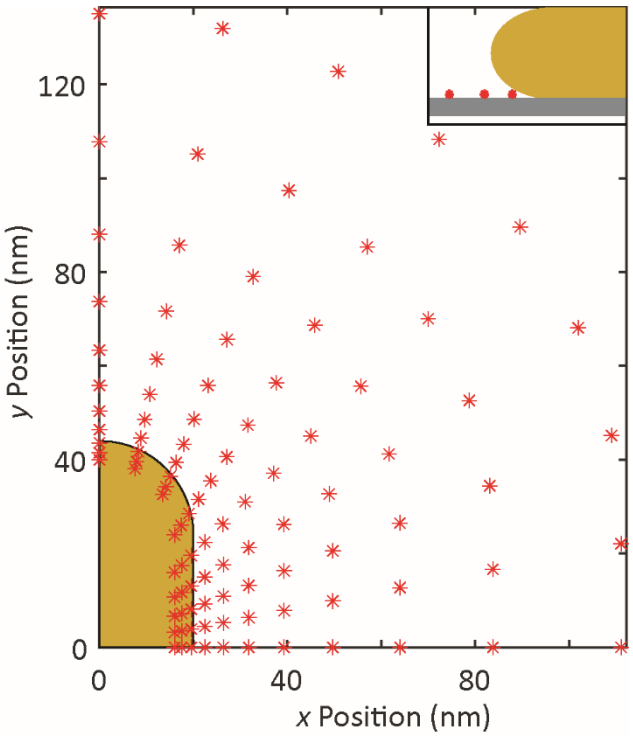

Figure 2.20: **Simulated dipole positions around a nanorod.** Simulated dipole positions around a nanorod (red asterisks), corresponding to the minimum symmetry unit of the nanorod. At each position, 19 dipole orientations were simulated. Inset: side view of the simulation geometry; the coverslip is indicated in gray.

2.6.6 Simulating the apparent emission polarization

The simulated near-field electromagnetic field distribution was propagated to the far field by employing near-to-far field transformations [78]. Only the components radiating at angles within the 1.4 numerical aperture of our objective lens were collected. The resulting distribution was focused to a plane, and at each emission wavelength considered (560 and 700 nm), the integral this diffraction-limited image was calculated to determine the fluorescence intensity at both polarization direction (x and y). The $\phi_{apparent}$ were then calculated by using Eq. 2.3.1 which is the same as the experimental data.

To predict the $\phi_{apparent}$ distributions that come from random dye adsorption positions in the experiment, Fig. 2.8 and Fig. 2.12 were generated by randomly sampling interpolated results on to an area of 0.6 μm^2 with nanorod in the center. The result of each location is the average from 3 closest simulation points shown in Fig. 2.20.

2.6.7 Parameterization of the nanoparticle-molecule interaction model

Frequency-domain electromagnetic simulations were performed to parameterize the analytic model. The MATLAB MNPBEM17 Toolbox was used [86]. Each nanorod was modeled as a cylinder with length = 48 nm and 40-nm diameter hemispherical caps with surface discretized to convergence of the scattering spectra in Fig. 2.6.7. Nanorods were assigned tabulated dielectric data from Johnson and Christy [85] and immersed in water with a constant refractive index of (n = 1.333, k = 0). The nanorod scattering spectra fit for model parameterization in Fig. 2.6.7 were generated by an incident plane wave polarized parallel to either the short or long axis of the nanorod.

The scattering cross section can be used to parameterize the coupled dipole model by fitting a model expression to experimental or simulated spectra for the nanorod. The scattering cross section σ_s is defined as the power scattered P_s per incident field intensity I_{inc}, and can be derived using the expressions for the fields radiated by a dipole. The scattering cross section of an ideal dipole with polarizability $\alpha(\omega)$ in an isotropic and non-dissipative

background is:

$$\sigma_s(\omega) \equiv \frac{P_s}{I_{\text{inc}}} = \frac{8\pi}{3}\frac{k^4}{n_b/2}|\hat{\epsilon}\cdot\boldsymbol{\alpha}(\omega)|^2, \tag{2.9}$$

where $k = \frac{\omega n_b}{c}$ and $n_b = \sqrt{\epsilon_b}$ is the background refractive index and $\hat{\epsilon}$ is the polarization vector of the incident field.[1]

For the purpose of modeling a nanorod, the frequency-dependent polarizability $\alpha(\omega)$ is set to be the modified long-wavelength tensor in Eq. 1.21 with components given by Eq. 1.25. The dielectric permittivity is assigned the Drude model in Eq. 1.5. This procedure yields $\sigma_s(\omega)$ determined by five free parameters, $\{a, b, \epsilon_\infty, \omega_p, \gamma\}$. First, the polarizability is fundamentally geometric and likewise, the two semi-radii of the prolate spheroid appear; (1) a along the long axis and (2) the short semi-radius b. Next, the three material properties determining the Drude model; (3) the high frequency limit of the permittivity ϵ_∞, (4) the plasma frequency ω_p containing the characteristic response time of the conduction electrons, and (5) electron scattering rate γ that serves as a damping on electronic motion. The simulated nanorod is assigned dielectric data for gold from Johnson and Christy [85]. Its geometry is a cylinder with radius of 20 nm and length of 24 nm with hemispherical end-caps of matching radius. The parameters resulting from the best fit of the two spectra in Fig. 2.6.7 are: $a = 51.77770nm$, $b = 15.9601nm$, $\epsilon_\infty = 28.9857$, $\hbar\omega_p = 13.5885eV$, $\hbar\gamma = 0.0977eV$

[1] The factor of $n_b/2$ in denominator of the scattering cross section corrects for the background dielectric properties and follows the implementation in the MNPBEM17 MATLAB toolbox [86].

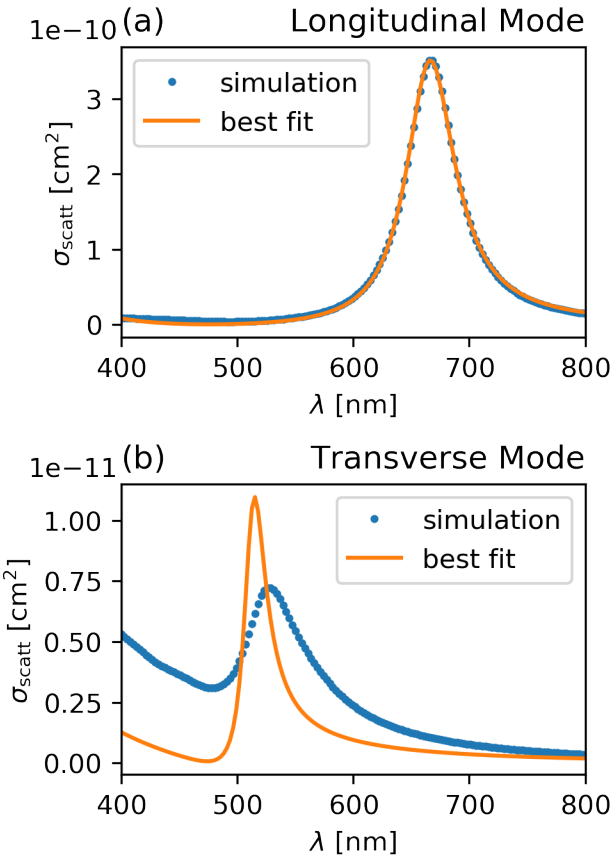

Figure 2.21: **Parameterization by fitting to long and short mode.** Parameterization of the nanorod polarizability along the long (a) and short (b) principal-axes of the nanorod from scattering spectra calculated by the Maxwell equations solver MNPBEM17 Toolbox for MATLAB [86]. Simulated cross sections were calculated by aligning the polarization of the incident light along either rod axis, and fit simultaneously to the corresponding model expression in Eq. 2.9 with appropriate component of the polarizability in terms of the five free parameters, $\{a, b, \epsilon_\infty, \omega_p, \gamma\}$. The relative inaccuracy of transverse mode fit can be attributed to the low-energy tail of gold interband transitions that overlap this portion of the spectrum and are not well accounted for by the Drude model dielectric function.

2.6.8 Far-field transformation of the diffraction-limited image fields for a point dipole

Following the methods section of Ref. 73, the focused and diffracted fields of a point dipole emitter can be calculated using the Debye-Wolf integral [87], which provides an accurate model of the fields produced by diffraction-limited optical systems with the large numerical apertures common in single-molecule fluorescence imaging [88]. For an idealized infinity-corrected microscope, the field composing the image can be constructed by first considering geometric refraction at the objective and tube lenses focusing the fields into image space and then considering diffraction effects at the tube lens aperture. As outlined in Ref. 89, both the objective and tube lens are considered spherical refracting surfaces with focal lengths f_{obj} and f respectively. The objective is defined by spherical coordinates $(\xi_{\text{obj}}, \zeta_{\text{obj}}, f_{\text{obj}})$ relative to the dipole location. The tube lens is defined by (ξ, ζ, f) relative to the focal point in image space. The image field is related to the scattered field at the objective by the integral:

$$\mathbf{E}(\rho, \varphi, z) = -\frac{ikfe^{ikf}}{2\pi} \int_0^{\xi_m} d\xi \sin\xi \int_0^{2\pi} d\zeta \sqrt{\frac{\cos\xi}{\cos\xi_{\text{obj}}}} \mathbf{E}^{\text{scat}}(\xi, \zeta) e^{ik[\rho \sin\xi \cos(\varphi - \zeta) + (z-h)\cos\xi]}. \tag{2.10}$$

The scattered field is evaluated at points on the objective by the relationship $\sin\xi = (f_{\text{obj}}/f)\sin\xi_{\text{obj}}$ and $\zeta = 2\pi - \zeta_{\text{obj}}$. The ratio of cosines appearing in the square root accounts for the two refractions. The term $e^{ik(z-h)\cos\xi}$ describes defocussing and defines the focal plane at $z = h$.

To obtain a simple closed form for the image fields, the numerical aperture is fixed at NA $= 1$ as well as the magnification, $f/f_{\text{obj}} = 1$. The effect of magnification can be restored theoretically by choosing a small, high-resolution image detection plane [90]. Under these conditions, both integrals in Eq. 2.10 can be solved analytically. The image field in the focal plane produced by a single dipole source with moment magnitude p_x

located along the optical axis ($\hat{e}_z$) and oriented in the $\hat{e}_x$ direction is:

$$\mathbf{E}^{\mathrm{im}}_{p_x}(\rho, \varphi, z = h) = -ik^3 e^{2ikf} p_x \begin{pmatrix} \left[\cos^2(\varphi) + \cos(2\varphi)\right] \frac{j_1(k\rho)}{k\rho} + \sin(\varphi)^2 j_0(k\rho) \\ \sin(\varphi)\cos(\varphi) j_2(k\rho) \\ -\cos(\varphi)\frac{J_2(k\rho)}{k\rho} \end{pmatrix}, \tag{2.11}$$

where the dipole moment points at an angle ψ relative to $\hat{e}_x$.

To express the field of an arbitrarily oriented dipole, this expression must be rotated. For a dipole $\mathbf{p} = |p|(\cos\psi_p \hat{e}_x + \sin\psi_p \hat{e}_y)$ oriented in the focal plane at an angle ψ_p from the x-axis, the generalized image field can be written in terms of Eq. 2.11 as

$$\mathbf{E}^{\mathrm{im}}(\rho, \varphi, z = h; \psi_p) = \mathbf{R}(\psi_p) \cdot \mathbf{E}^{\mathrm{im}}_{p_x}(\rho, \varphi - \psi_p, z = h), \tag{2.12}$$

where the rotation matrix is defined:

$$\mathbf{R}(\psi) = \begin{pmatrix} \cos\psi & -\sin\psi & 0 \\ \sin\psi & \cos\psi & 0 \\ 0 & 0 & 1 \end{pmatrix}. \tag{2.13}$$

CHAPTER III

Model-Based Localization and Polarization Determination of Single-Molecule Emission

Sec 3.2 and 3.3 presented in the chapter has been published in

Tiancheng Zuo, Harrison J. Goldwyn, Benjamin P. Isaacoff, David J. Masiello, Julie S. Biteen. "Rotation of Single-Molecule Emission Polarization by Plasmonic Nanorods". *The Journal of Physical Chemistry Letters*,**10**,5047-5054 (2019). DOI: 10.1021/acs.jpclett.9b02270

Author contributions

TZ designed and carried out the experiments, analyzed data, and performed time-domain FDTD with help from JSB. HJG developed and implemented the analytical model and performed frequency-domain electromagnetic simulations with help from DJM. All authors discussed the results and analysis, developed conclusions, and edited the paper.

3.1 Introduction

Super-resolution imaging techniques overcome the diffraction limit and enable optical microscopes with resolution down to tens of nanometers. Plasmonic nanoparticles are known to concentrate the electromagnetic fields around them. Therefore, they have been

used to enhance the fluorescent intensity [41, 42, 58, 83]. One promising application is to use plasmonic nanoparticles to enhance the resolution for bioimaging [91] and hotspot mapping [64, 65, 92, 93].

The raw images obtained from single-molecule microscopy are still diffraction-limited. Each point spread function (PSF) is fit with a 2-dimensional Gaussian function to localize the center with sub diffraction-limited resolution. The assumption behind this fitting method is that the most intense emission point of the PSF in the image plane should reflect the single emitter location in the focal plane. The single-molecule PSF can be well-described by a 2-dimensional Gaussian function. Hence, the single emitter location can be calculated by fitting the PSF to the Gaussian function. The more photons obtained from a single emitter, the better resolution the fitting can get [94]. However, it has been discovered that the PSF is distorted by the plasmonic nanoparticles upon coupling [1, 64, 65, 72, 73, 75, 90, 95–99]. In order to get the optimal enhancement, the single emitter must be close (within tens of nanometers) to the plasmonic nanoparticle [77, 83]. In this coupling geometry, the assumption that the most intense emission point represents the single emitter location is no longer true as the plasmonic nanoparticle scatters light efficiently, acting like a second emission center within a diffraction-limited region. Another way to explain the modification of the emission pattern is that the plasmonic nanoantenna alters the local density of states of proximal single emitters [65]. Consequently, the center of a Gaussian function that is used to fit the distorted PSF will not indicate the true location of the single emitter. This mismatch between the true emission center and the localization from the Gaussian fit is also called mislocalization. The extent of mislocalization in a nanoparticle-molecule coupling geometry can be as large as 30-50 nm either towards or away from the plasmonic particle [65, 73, 95, 96]. It has been understood that the mislocalization is indeed a result of emission coupling [65, 96]. Using a dye with an emission spectrum largely blue-shifted relative to the localized surface plasmon resonance (LSPR) of the plasmonic particle can avoid mislocalization to a great extent and still achieve en-

hancement through absorption coupling [51,75]. However, the linewidth of both the LSPR and single molecule emission spectrum are broad, which makes it harder to decouple the emission coupling from absorption. Additionally, enhancement is largely weakened without the emission coupling [42,58,100]. A more complex model is needed to understand the emission coupling and to extract the true molecule position in the presence of emission coupling. Models such as the dipole-dipole interference model [65,73,100] and the multipole model [90] have been proposed in the past 5 years to account for the distortion in the PSF due to plasmonic structures nearby. The multipole model was developed to describe a much stronger coupling regime, such as super-resolution surface-enhanced Raman scattering, in which the molecule distance is usually much closer to the plasmonic structure (< 10 nm) [90, 101]. Within that distance, fluorescence is usually quenched [61, 77, 83]. Landes *et al.* also used a Hermite-Gaussian model to retrieve the orientation information from a multilobed PSF that occurs when a dye couple to an Ag nanowire. One of the challenges that hinders the model development is the difficulty of designing a single-molecule experiment that allows one to have the information of the ground truth position of the molecule [96,102–104].

Here, we extend the dipole-dipole interference model [73] from fitting a highly symmetric nanosphere system to a simulated anisotropic nanorod system and extract the molecule orientation and location from the model fitting with the error significantly less than the standard Gaussian fitting. We also present a high throughput single-molecule experiment in which the molecule-nanoparticle radial distance is controlled. The model and experiment together will make it possible to ultimately apply the model to fit experimental data and retrieve the true molecule positions.

3.2 Model-based localization and polarization determination on simulated data

As detailed in Sec. 3.1, since the image of a plasmon-coupled dye molecule will be affected by the presence of the plasmonic nanoparticle, a simple centroid determination fails to retrieve the position of the molecule. We therefore examined this mislocalization effect with simulations. The model-generated image:

$$I_q = \frac{cn}{8\pi} \left| \left(\mathbf{E_0^{im}} \cdot \hat{\mathbf{e}}_\mathbf{q} \right|^2 + \mathbf{E_1^{im}} \cdot \hat{\mathbf{e}}_\mathbf{q} \right|^2 + 2\mathrm{Re}\left[\mathbf{E_0^{im}} \cdot \hat{\mathbf{e}}_\mathbf{q} \mathbf{E_1^{im}} \cdot \hat{\mathbf{e}}_\mathbf{q} \right] \right) \tag{3.1}$$

can be used as a simultaneous localization and polarization fit function to recover the true position and orientation of nanorod-coupled dye molecules. Model localization and polarization determination is accomplished by least-squares fit of the model generated images to the simulated images with no noise (See Sec. 2.6 in Chapter II). In the simulation, the dipoles were evenly distributed in the 250 nm x 250 nm square around the nanorod. Fig. 3.1 shows the design of the simulation. At each dipole position (black dots), two orientations were considered: parallel to the x-axis and parallel to the y-axis.

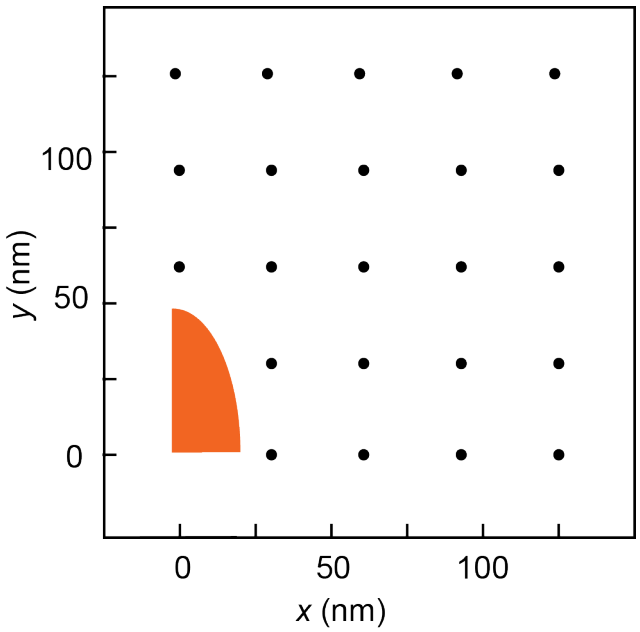

Figure 3.1: **Simulation geometry.** The orange shape is a quarter of gold nanorod. At each dipole position (black dots), two orientations were considered: parallel to the x-axis and parallel to the y-axis. Nanorod were modeled as a cylinder with length = 44 nm and 40-nm diameter hemispherical caps. All simulations were performed with the nanorods immersed in water and placed on a glass slab.

The model fits take only 3 free parameters, since molecules are assumed to lie in the focal plane (center of the nanorod) with dipole moment located in the focal plane. The initial guesses for molecule location are determined by the result of Gaussian localization and fits are insensitive to the guess of the molecule orientation. When the molecule is close to the nanorod and the images become dominated by plasmon emission, each image does not change much with molecule location. With this naive initial guess procedure, these fits often converge to molecule locations on top of the nanorod, which is unphysical because such molecules should be quenched. To resolve this issue, a smarter initial guess algorithm was implemented: if the initially guessed molecule location provided by the Gaussian localization procedure is located on top of the nanoparticle, the guess location is pushed outside the quenching zone [61, 77, 83] of the nanorod (defined as 10 nm added to the prolate spheroid radius). This algorithm was found to yield numerically stable fit results, showcasing the best fit possible with the current model and parameterization presented

in this work.

The results for the model fit were compared to standard Gaussian fits. Gaussian localization fits a two-dimensional Gaussian function to the normalized simulated images with 5 free parameters: the two centroid coordinates (x, y), two standard deviations, and a rotation angle. Initial guesses for least-squares minimization of the residual for the centroid coordinates are determined by the (numerical) detector pixel of maximum intensity. Initial guesses for the widths are fixed near the diffraction limit, and the initial rotation angle was not found to have consequence on the fit convergence.

3.3 Comparison between model-based fitting and typical Gaussian fitting

Let's now compare the fit results from the typical Gaussian fitting and model-based fitting. Again, the four geometries mentioned in the last chapter Sec. 2.4.2 was studied here. The molecules in Fig. 3.2 are aligned along the x-axis (0°). For the model fits in Fig. 3.2b, the molecule and nanorod dipoles are parametrized, leaving only three fit parameters for residual minimization: the x and y coordinates of the molecular transition dipole relative to the center of the nanorod, and the dipole angle.

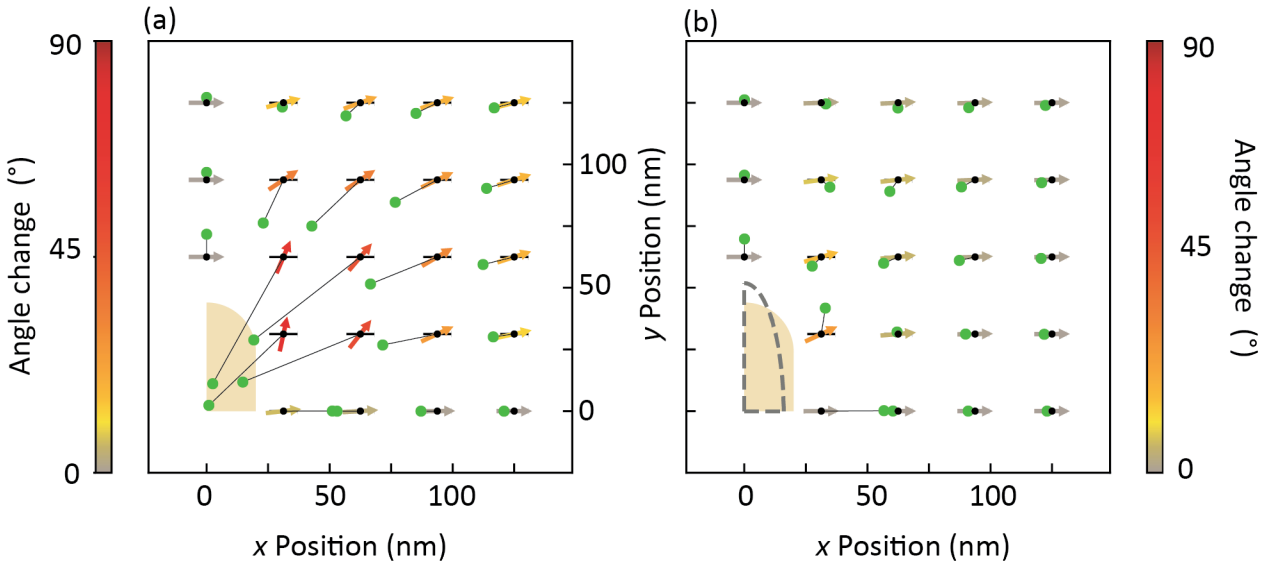

Figure 3.2: **Model evaluation geometry 1.** Comparison of the best fit results for dipole position (green) and polarization (colored arrows) determined in simulated diffraction-limited images (at a single frequency matching the longitudinal LSP peak in Fig. 2.6.7) of 23 simulated single-molecule dipoles (black dots) oriented parallel to the x-axis and placed near a nanorod (shaded tan) up to 150 nm away from the center of the nanorod. (a) Gaussian localization of the total intensity paired with molecule orientation as would be determined by polarization-resolved microscopy reveals the familiar mislocalization of x-oriented molecules mostly toward the nanorod (apparent locations marked by green dots connected to the true molecule location in black) is accompanied by mispolarization of the molecules due to superposition of fluorescence emission redirected through the nanorod. (b) Least-squares fit of the model-generated images to simulated images.

The comparison to the other three geometries is listed below:

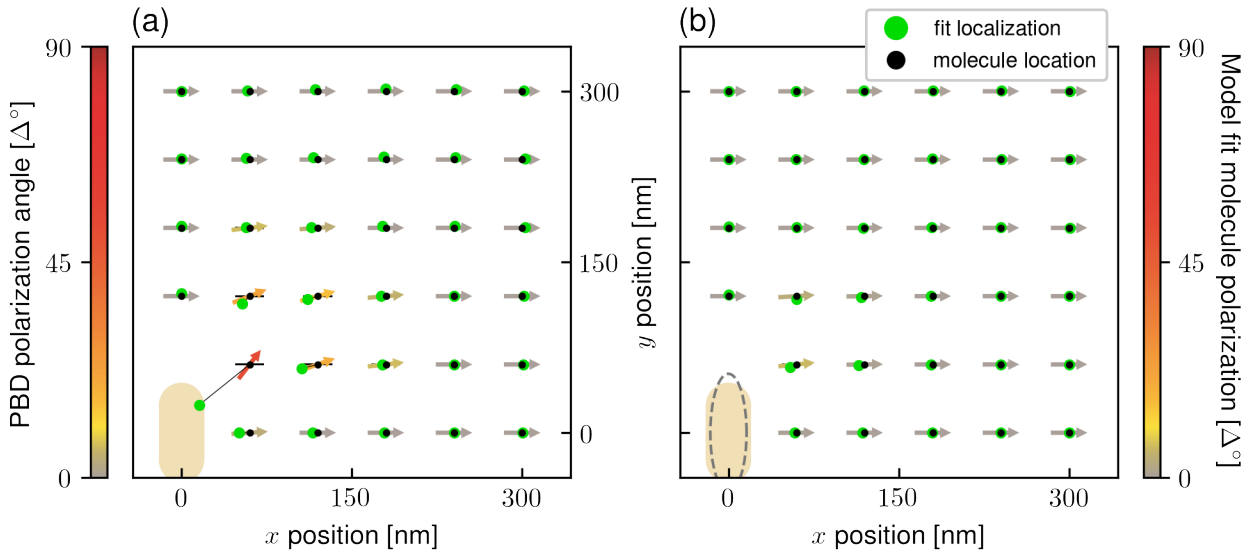

Figure 3.3: **Model evaluation geometry 2.** Comparison of best fit results for molecule position (green) and polarization (colored arrows) determined for diffraction-limited images of 23 simulated x-axis oriented single molecule dipoles (black dots) near a nanorod (shaded tan) up to 300 nm away from the center of the nanorod. (a) Gaussian localization of the total intensity paired with molecule orientation as would be determined by polarization-resolved microscopy reveals the familiar mislocalization of x-oriented molecules mostly toward the nanorod (apparent locations marked by green dots connected to the true molecule location in black) is accompanied by mispolarization of the molecules due to superposition of fluorescence emission redirected through the nanorod. (b) Least-squares fit of the model-generated images to simulated images.

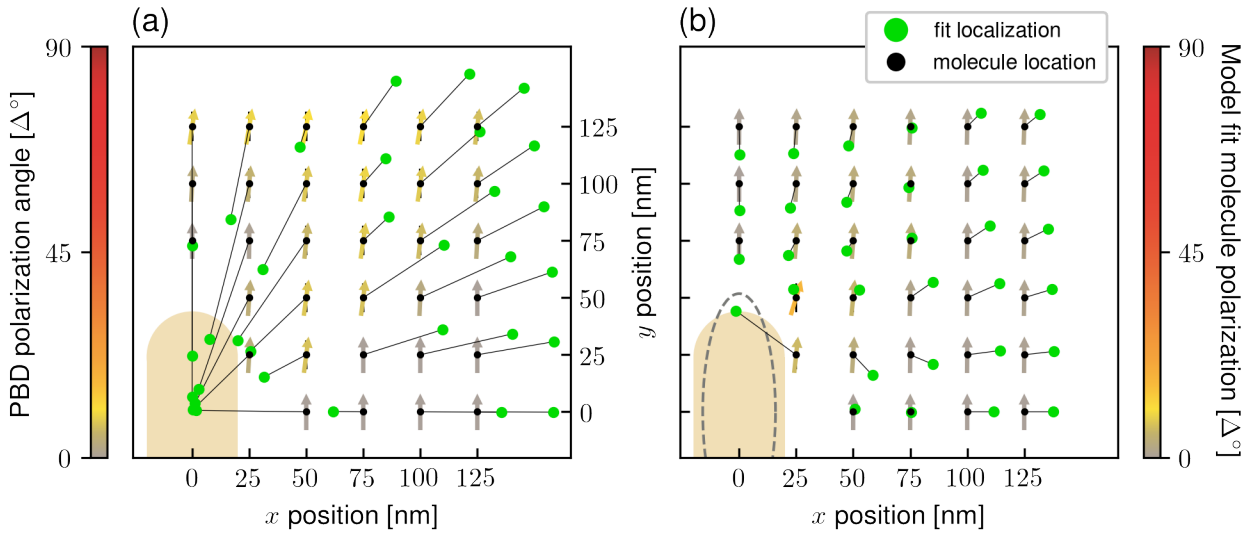

Figure 3.4: **Model evaluation geometry 3.** Comparison of best fit results for molecule position (green) and polarization (colored arrows) determined for diffraction-limited images of 23 simulated y-axis oriented single molecule dipoles (black dots) near a nanorod (shaded tan) up to 150 nm away from the center of the nanorod. (a) Gaussian localization of the total intensity paired with molecule orientation as would be determined by polarization-resolved microscopy reveals the familiar mislocalization of x-oriented molecules mostly toward the nanorod (apparent locations marked by green dots connected to the true molecule location in black) is accompanied by mispolarization of the molecules due to superposition of fluorescence emission redirected through the nanorod. (b) Least-squares fit of the model-generated images to simulated images.

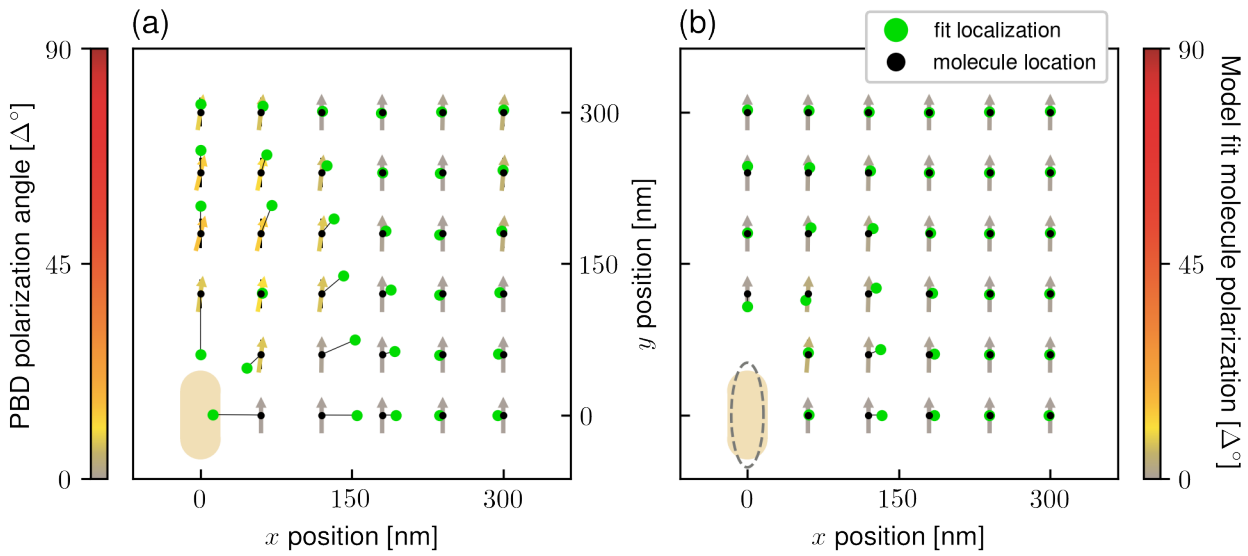

Figure 3.5: **Model evaluation geometry 4.** Comparison of best fit results for molecule position (green) and polarization (colored arrows) determined for diffraction-limited images of 23 simulated y-axis oriented single molecule dipoles (black dots) near a nanorod (shaded tan) up to 300 nm away from the center of the nanorod. (a) Gaussian localization of the total intensity paired with molecule orientation as would be determined by polarization-resolved microscopy reveals the familiar mislocalization of x-oriented molecules mostly toward the nanorod (apparent locations marked by green dots connected to the true molecule location in black) is accompanied by mispolarization of the molecules due to superposition of fluorescence emission redirected through the nanorod. (b) Least-squares fit of the model-generated images to simulated images.

The model-based localization and polarization significantly outperform Gaussian localization and effectively eliminate the mispolarization observed in $\phi_{apparent}$ for all molecules studied here except those closest to the nanorod corner. The mislocalization error is greatly reduced because, unlike Gaussian fitting, the molecule location is estimated with full knowledge of the interaction and configuration-dependent far-field radiation pattern produced by coupled dipoles. Any error left in the determined molecule location is not due to convolution of molecule and nanorod emission, but is likely a due to the slight deficiency of the Drude model dielectric function for describing the optical response of gold in the frequency range spanning the longitudinal and transverse mode resonances (Fig. 2.6.7). Although a model dielectric function with greater predictive power and more fit pa-

rameters can easily be employed, the degree of success achieved here demonstrates that the relevant physics underlying the diffraction-limited image of coupled molecule and nanorod can be qualitatively captured with only the three Drude material parameters.

The in-plane molecule orientation is determined by the model fit in a qualitatively different manner from the way $\phi_{apparent}$ is calculated. While the latter is a measure of the average polarization of a dye molecule in the focused image field, the model fit angle is a direct estimation of the orientation of the molecule emissive transition dipole moment during the time span of photon collection. At close molecule-nanorod separations, the localization provided by the model fit seems to be no more reliable than Gaussian fitting. This fitting error is due to the simplicity of the model rather than the fitting process. For instance, greater accuracy could be achieved by including the nanorod quadrupolar LSP response which becomes increasingly important at close proximity.

3.4 Distance-controlled single-molecule experiments

So far, we have shown that model-based fitting outperforms Gaussian fitting on single-molecule images generated from simulation. If we want to actually apply the model-based fitting to single-molecule images obtained from experiments, it requires us to know the actual location of the molecules to do the ground truth validation. The points accumulation for imaging in nanoscale topography (PAINT) experiment described in Chapter II was not able to control the distance between dye and nanoparticle because it relied on random positioning. Here, we designed a single-molecule experiment that allows us to know the radial distance between molecules and nanoparticles by using double stranded DNA (dsDNA) as spacers (Fig. 3.6a). Short dsDNA oligomers (< 50 nm) are rigid in aqueous solutions [76]. A single stranded DNA with ATTO 590 at one end and a complementary single stranded DNA with -SH group at the other end was hybridized to produce a dsDNA molecule with dye at one end and thiol at the other. Nanodisks that consisted of a layer of Cr, a layer of Au, a layer of Cr, then a final layer of SiO_2 were made by electron-beam

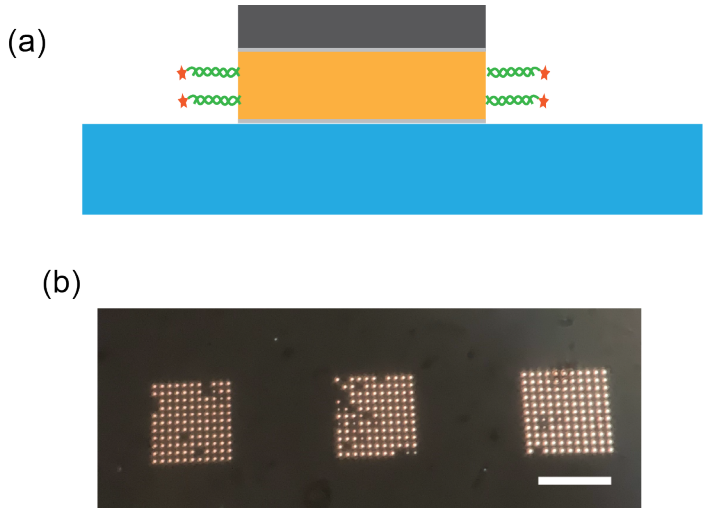

Figure 3.6: **Sample design and dark-field imaging.** (a) schematic of a nanodisk sample design. The blue slab at the bottom is the glass coverslip, the orange square is the gold nanodisk (30 nm thick, 70 nm diameter) and the dark grey layer on the top is the coated SiO_2 (20 nm thick). The two thin grey layers on the top and bottom of the gold layer are the wetting Cr layers (2 nm thick). DNA linkers are shown by the green double helices (30 base pairs, 10 nm) and the red stars indicate single ATTO 590 dye molecules. (b) dark-field image of the three gold nanodisk arrays with different sizes of nanodisks and center-to-center spacing of 2 μm. The scale bar is 15 μm

lithography (EBL) (Fig. 3.6a). The dye molecules with dsDNA spacers were then attached to the nanodisks via a S-Au bond. Because of the SiO_2 layer on the top, the dyes are only able to attach to the gold disks from the sides. Therefore, the radial distance of each dye molecule to the edge of the nanodisk is always the length of the dsDNA which is controlled by the number of base pairs. In this study, DNA spacers of 30 base pairs, which corresponds to a length of 10 nm, were used (Table 3.1). Experimental and simulation studies show that 10 nm distance is a optimal distance for plasmon enhancement and does not induce quenching [63, 76, 77]. To study how the mislocalization is affected by the size of nanodisk in a high throughput fashion, we made nanodisks into arrays by EBL with three different diameters, 70, 76, and 86 nm and chose the spacer dsDNA with 30 base pairs (10 nm). Fig. 3.6b shows the dark-field scattering image of those three nanodisk arrays. The size of the array is designed to fit in the full size of the field of view (25x25 μm^2) in the epifluorescence single-molecule setup used in the lab [72,76] and the 2 μm large pitch size between each nanodisk prevents any lattice mode in LSPR [72, 91]. The three nanodisk diameters were chosen such that the smallest one, 70 nm would have a bluer LSPR wavelength than the ATTO 590 emission peak (Fig. 3.7a), the middle one, 76 nm, would overlay well with ATTO 590 (Fig. 3.7b) and the biggest one, 86 nm would be redder (Fig. 3.7c).

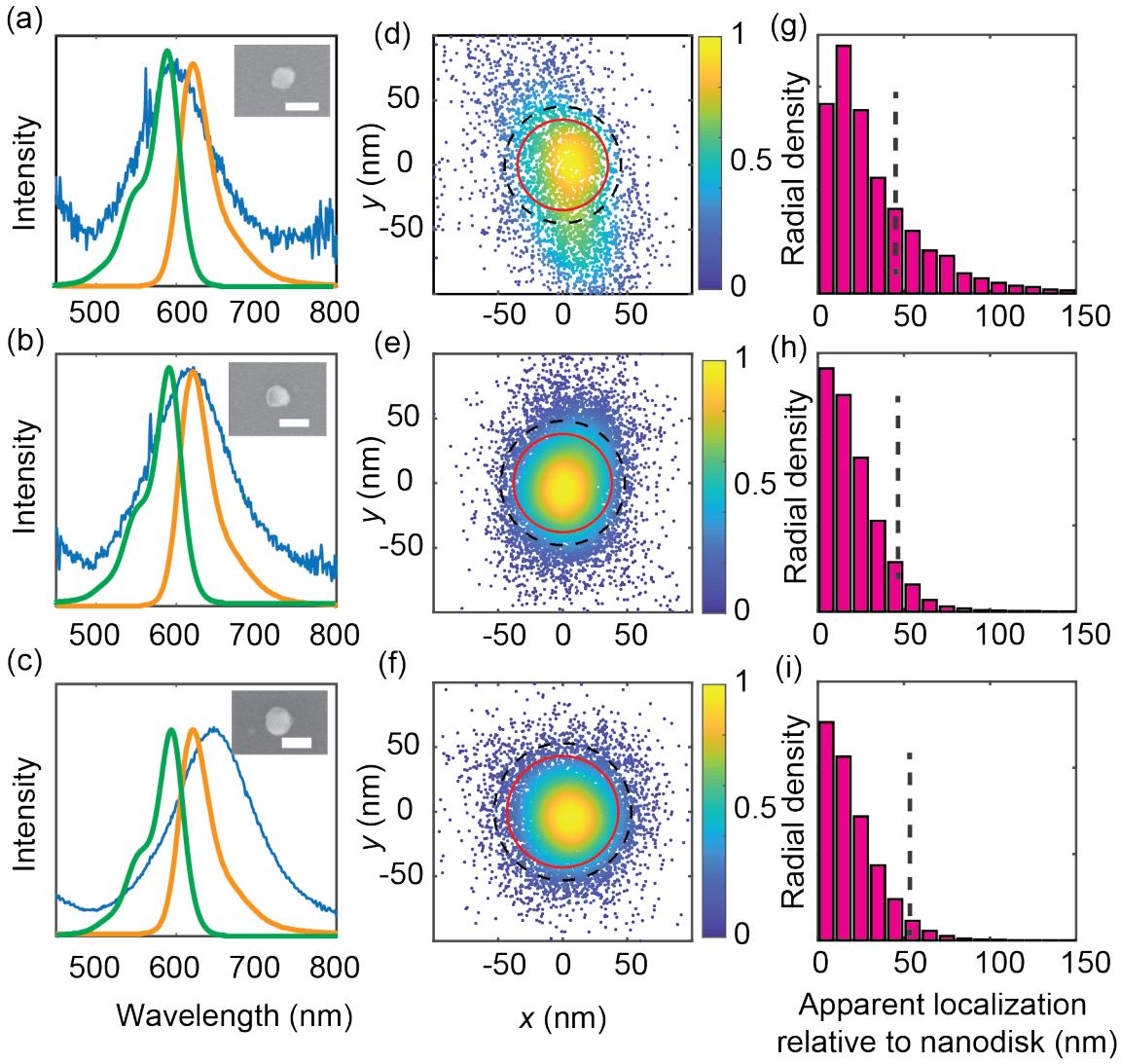

Figure 3.7: **Dark-field spectra and apparent localization density.** Blue curves in a-c are the dark-field scattering spectra of 70, 76 and 86 nm diameter nanodisks, respectively. The green and orange curves are the ATTO 590 absorption and emission spectra respectively (data from IDEX Health & Science, LLC). The insets: SEM images of a single nanodisk with 100 nm scale bars. d-f are the localization density maps centered at the nanodisks. Red circles indicate the size of the nanodisk, 70, 76 and 86 nm, respectively. Black dashed circles indicate the actual radial positions of the dye molecules. The colorbar in each figure shows the normalized apparent localization density. g-i are the radial localization density histograms with the black dashed lines indicating the actual radial positions of the dye molecules. For each diameter, we detected the fluorescence from 2000-8000 single molecule fluorescence events from molecules around 12 particles.

Single molecule emission images were then collected by our epifluorescence single molecule setup via direct stochastic optical reconstruction microscopy (dSTORM) method [76, 105]. Under the laser excitation, ATTO 590 molecules stochastically turned on and off in the oxidizing and reducing dSTORM imaging buffer, which enables single-molecule imaging [105]. Fig. 3.7d-f shows the molecule localization density maps around the three different size nanodisks. The localization was done by the conventional Gaussian fitting method. The localization density for each point is defined as the number of neighboring points within a 25-nm radius circle divided by the area of the circle. If there were no mislocalizations, all the molecules would appear to be located along a ring 10 nm away from the edge of the disks (black dashed circles). However, in Fig. 3.7d-f, at least 80% of the localizations appear to be shifted to the inside of the black circles and at least 5% shift outside the black circles. In other words, most of the molecules are mislocalized towards the nanodisks and a few are mislocalized outwards. As the nanodisk size gets bigger, the apparent localizations shift further away from the true locations, more towards the center of nanodisk.

This trend in the magnitude of the localizations is more obvious in Fig. 3.7g-i, which shows the radial density plots of those apparent localizations. The radial localization density is defined as the number of localizations within each radial distance interval (10nm) divided by the area of that radial distance interval. The dashed vertical lines show the actual radial location of the dyes. It is evident that as the nanodisk size gets bigger, a higher percentage of the apparent positions fall on the left side of the dashed vertical lines, i.e., is towards the center of the nanodisk. A shift in the most probable position as large as 50 nm is seen in Fig. 3.7i. Among the three different size nanodisks, the LSPR of 86-nm nanodisk overlaps least with the absorption of ATTO 590 Fig. 3.7c, however, it shifts localization the most. Therefore, mislocalization is less related to absorption coupling than emission coupling. For each diameter, we detected the fluorescence from 2000-8000 single molecule fluorescence events from molecules around 12 particles. Fig. 3.8 shows the

localization density maps of the molecules about one particle of the 3 different sizes. This figure shows the inhomogeneity that arises from undersampling, and comparing Fig. 3.7 and Fig. 3.8, it shows that summing the localization from 12 particles gets rid of this inhomogeneity.

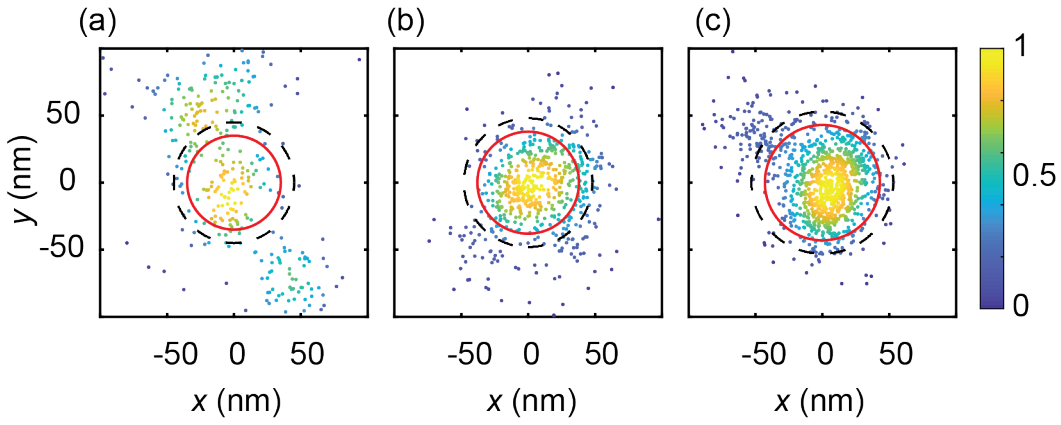

Figure 3.8: **Representative localization density maps.** a-c are the localization density maps of one nanodisk from each of the 3 different sizes, respectively. Red circles indicate the sizes of the nanodisk: 70, 76 and 86 nm, respectively. Black dashed circles indicate the actual radial positions of the dye molecules. The colorbar in each figure shows the normalized apparent localization density.

We performed simulations to investigate if the trend and extent of mislocalization in this experiment agree with simulation. In the experiment, the attached ATTO 590 has some degree of freedom in terms of rotational movement because it is bound to the DNA through a single covalent bond. In the simulation, to qualitatively mimic the rotational flexibility of the dye molecules, three different orientations were considered: oriented in the radial direction (x-axis), oriented in the tangential direction (y-axis) and oriented vertically (z-axis) (Fig. 3.9a).

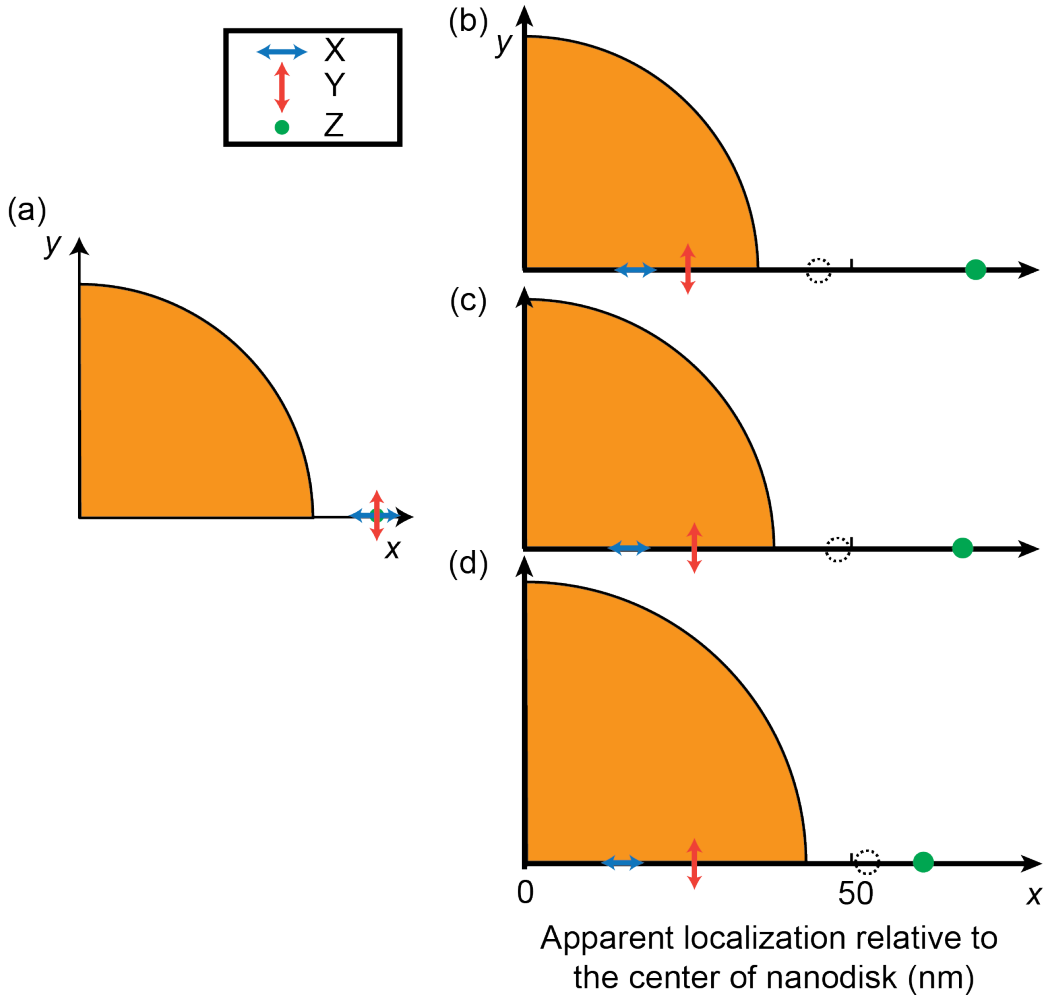

Figure 3.9: **Simulation setup and results.** a is the top view of one quadrant of the 70-nm nanodisk simulation setup. We simulated a dipole located 10 nm away from the edge of the nanodisk for each of three different nanodisk sizes. Three different dipole orientations were considered, parallel to the x-axis (blue arrows), parallel to the y-axis (red arrows) and parallel to the z-axis (green dots). b-d are the apparent localizations of those three dipoles coupled to three different sizes of nanodisk respectively: 70, 76 and 86 nm. The edge of each nanodisk is indicated by the orange shape with a curve on the right. Black dashed circles in a-d indicate the actual radial positions of the dipoles.

A similar trend of mislocalization is seen in the simulation in Fig. 3.9b-d as in the experiments in Fig. 3.7. As the size gets larger, the apparent localizations shift more towards the nanodisk than outwards the nanodisk.

Single-molecule imaging also enables us to correlate each molecule's emission intensity with the apparent emission position. Fig. 3.10 shows the relationship between the single-molecule intensity enhancement and the apparent radial position. The molecules localized at their actual radial distance are molecules that have no coupling to the nanodisk. These molecules should therefore have no intensity enhancement. The average intensity enhancement is therefore calculated by normalizing the intensity at each position by the average intensity of the molecules localized in the radial distance interval of 50 nm, as this interval comprises the actual molecular distances (45, 48 and 53 nm). The localizations larger than the actual distances (45, 48 and 53 nm) correspond to the molecules whose emission got mislocalized further away from the nanodisks. This outward mislocalization is also confirmed in the simulations (the green dots in Fig. 3.9). On the other hand, the overall trend in Fig. 3.10 indicates that the molecules that appear mislocalized farther inward have higher intensity. The difference between Fig. 3.10 and Fig. 3.7a-c indicates that emission intensity enhancement (greatest for the 76-nm nanoparticles in Fig. 3.10) is affected by the overlap of the nanoparticle LSPR with both the absorption and emission spectra of the dyes, whereas the mislocalization (greatest for the largest nanoparticles in Fig. 3.7) is the result of emission coupling. The LSPR frequency of the 76-nm nanodisks overlaps with both absorption and emission of the dye the most (Fig. 3.7b). Therefore Fig. 3.10b shows the most enhancement. The LSPR frequency of the 86-nm nanodisks overlaps less relative to the 70-nm nanodisks with the absorption so less enhancement is seen (Fig. 3.10a and c). However, the LSPR frequency of the 86-nm nanodisk overlaps with the dye emission more than the 70-nm one, so it produces more mislocalization (Fig. 3.7g and i).

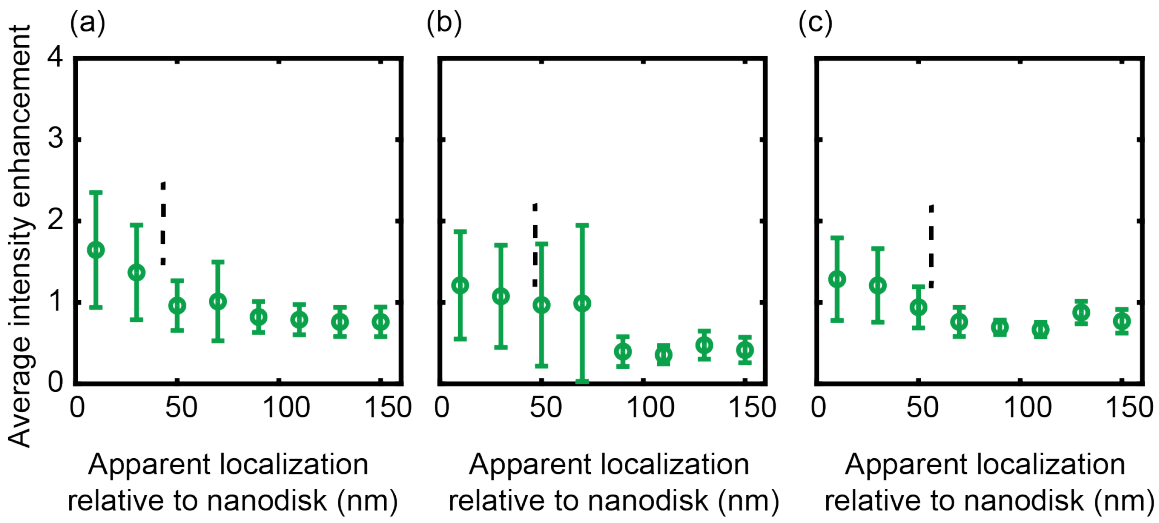

Figure 3.10: **Emission intensity vs. apparent emission localization.** a-c are the single molecule emission intensity vs. apparent emission localization plots for 70, 76, 86 nm nanodisks, respectively. The green circles show the average intensity of the molecules at that position interval divided by the average intensity of molecules at the 50-nm radial distance interval (i.e., at the actual position of the molecules). The length of the error bars shows the standard deviation of the normalized molecule intensity at each 20-nm radial distance interval. Black dashed lines indicate the actual radial positions of the molecules.

3.5 Conclusion

In conclusion, we extracted the molecule orientation and location by fitting an analytical model of the coupled-dipole image to simulation data. The model developed exceeds the accuracy of the best fits achieved through standard Gaussian localization as well as the polarizing beam displacer (PBD) based determination of the in-plane polarization angle for simulated molecule-nanorod images. We also presented a single-molecule experiment that enabled us to couple a single plasmonic particle to a single dye with precise distance control in a high throughput way. By correlating the single-molecule emission intensity with its apparent emission localization, we show that indeed mislocalization is a result of fluorescence emission coupling whereas intensity enhancement is affected both by absorption coupling and emission coupling.

In the future, the model will be applied to the experimental data to recover the true

molecule positions in experiments. The model will incorporate the presence of the substrate and the dielectric constant of the environment. One of the challenges is how to maintain the accuracy that model has achieved with the simulated image as the experimental data will inevitably have noise. Having more readouts besides the emission image will also improve the accuracy of the model, such as emission spectrum and emission decay rate [99]. Additionally, the dependence of absorption coupling on mislocalization would be an interesting direction to investigate. This study would, however, require additional experimental progress. Such an investigation might be realized by looking into the single-molecule absorbance and its corresponding mislocalization. Although single-molecule absorbance enhancement by plasmonic nanoparticles was proved theoretically [58, 63] a decade ago, it is challenging to demonstrate this absorbance enhancement in experiment at the single-molecule level. In bulk solutions, on the hand, the absorbance enhancement can been demonstrated [106]. For example, it can be achieved by comparing the absorbance of the solution that contains nanoparticles linked with dye molecules to the absorbance of the solution without nanoparticles [106]. Measuring absorbance in bulk solution is easier to realize as the difference of the light intensity when passing through the bulk dye solution is significant enough to be detected. However, measuring single-molecule absorbance is challenging and must be realized by indirect methods like photothermal absorption spectroscopy [107–110]. It would therefore be difficult to measure mislocalization based on absorbance instead of emission.

3.6 Methods and characterization

3.6.1 Gold nanodisk arrays preparation

Gold nanodisk arrays were designed with 3 different diameters and 9 repeating units 70, 80 and 90 nm, respectively. The actual sizes of 70, 76 and 86 nm were selected based on the simulation described below. The nanodisks were prepared on coverslips by EBL.

First of all, a 200 nm poly(methyl meth-acrylacte) (PMMA, Michrochem) layer was spin coated on a glass coverslip. Then an 8 nm gold thin film was thermally deposited on top of the PMMA to make a conductive layer for electron beam writing (Angstrom Engineering, Evovac Evaporator). The sample was then exposed to an electron beam, 110 kV, 1000 pA (JEOL JBX 6300FS). The thin gold layer was removed with gold etch (KI and iodine complex) followed by soaking in developing solvent, 1:3 methyl isobutyl ketone (MIBK): isopropanol (IPA). The sample was cleaned with IPA. A 30 nm gold layer was coated on to the coverslip by electron beam evaporation (Denton Enerjet Evaporator). A 20 nm SiO_2 layer was then coated on top of the gold layer. Before and after the gold layer, a 2 nm Cr was evaporated onto the sample as wetting layers. Finally the sample was soaked in 60°C acetone overnight for the lift-off.

3.6.2 Linking ATTO 590 to nanodisks

This protocol was adapted from methods mentioned in ref [76, 111, 112]. 5 μL 100 μM thiolated single stranded DNA was mixed with equal amount of complementary ATTO 590 single stranded DNA (Table 3.1). 80 μL ethylenediaminetetraacetic acid-tromethamine (Tris-EDTA) pH 8 was added. The solution was hybridized at 95°C for 2 mins followed by incubation at room temperature for 1 hour. 10 μL 1M dithiothreitol (DTT) (15mg in 100 μL Tris-EDTA buffer) and 130 μL Tris-EDTA buffer were added into the solution for an hour to reduce the disulfide group. NAP-5 column (GE Healthcare Life Sciences) was then used to separate the DTT from the thiol dsDNA. 1 mL of the DNA solution was immediately added to the beaker that contained the nanodisks coverslip. 9 mL of Tris-EDTA was added and the sample was incubated for 1 hour. 100 μL of 0.1 M phosphate buffer, 1/10 by volume and 1 μL 10% sodium dodecyl sulfate (sds), 1/1000 by volume, was added to reduce the non-specific binding of dyes to the coverslip. The sodium chloride concentration in the solution was gradually brought up to 0.5 M over the course of 3 hours to increase the DNA loading. Finally, the coverslip was sonicated in deionized water 3 times to get rid of

unbound dsDNA and blow dried with high pressure nitrogen gas.

DNA base pair number	Sequence
30	5- /5ThioMC6-D/CTT GCC ATC GCT AGT ACA TGG CAC TGA CTG -3
30	5- /5ATTO590N/CAG TCA GTG CCA TGT ACT AGC GAT GGC AAG -3

Table 3.1: **Oligonucleotides used in this study.**

3.6.3 dSTORM imaging

Single-molecule dSTORM imaging was performed in the epifluorescence setup used in the previously published work from our lab [1, 72, 76]. A 561-nm CW laser was used as the excitation light source (Coherent CUBE). 100μL of dSTORM imaging buffer was drop on the sample coverslip. The sample was illuminated with high laser power at 40 $\mu W/\mu m^2$ to make dyes enter dark state and was imaged at 12 $\mu W/\mu m^2$ [105, 113, 114]. Images were recorded by an 512 pixel x 512 pixel Andor iXon EMCCD camera with electron-multiplying gain set to 1000 at 100 ms integration time.

100 μL 500mM 2-Mercaptoethanol (MEA) at pH 9 was used as dSTORM imaging buffer to control the density of actively fluorescent molecules at any given time in order to enable single-molecule detection [105, 113, 114].

3.6.4 Electromagnetic simulations for nanodisks

Time-domain electromagnetic simulations were performed by using the Lumerical finite difference time domain (FDTD) Solutions software package. All simulations were performed with the nanodisk immersed in water and placed on a glass slab. The total simulation volume is 3.375 μm^3; near the nanodisk, a fine-mesh grid with 3.375 nm^2 cell volume was used. Water and glass were modeled with a constant refractive index of (n

= 1.333, k = 0) and (n = 1.5, k = 0), respectively. The frequency-dependent complex permittivity of Au and Cr was obtained by an analytical fit to experimental data [85]. The thickness of each layer in the nanodisks are 2 nm Cr, 30 nm Au, 2 nm Cr and 20 nm SiO_2 (from the bottom to the top). The nanodisks diameters were determined by varying the simulated cylinder radius and matching the simulated far-field scattering spectra to the experimentally measured dark-field scattering spectra (Fig. 3.12).

The simulated scattering spectrum of nanodisk in Fig. 3.12 was calculated by exciting the nanodisk from above the water at normal angle with a broadband plane wave, which is consistent with dark-field spectroscopy experiments. Two orthogonal excitation polarizations were averaged to simulate incoherent lamp light.

To reproduce the coupled emission with dye molecules 10 nm away from a nanodisk, we simulated dipoles at 10 nm away, at the height of the center of the gold layer. Simulations were run for 3 different orientations: oriented in the radial direction (x-axis), oriented in the tangential direction (y-axis) and oriented vertically (z-axis) (Fig. 3.9a). To mimic the effect of our objective lens, the fields were monitored and recorded in a plane in the glass substrate below the dipole source.

3.6.5 Gold nanodisk characterization

In each of the three sizes of nanodisks, dark-field scattering spectra were collected from 3 randomly chosen nanodisks (Fig. 3.11). These arrays were immersed in water. A broadband halogen white light source excited the sample through a dark-field water-immersion condenser, and scattered light was collected in an Olympus IX71 inverted microscope equipped with a dark-field oil-immersion objective (NA = 0.6). The diffraction-limited image of a nanodisk was aligned to the entrance slit of an imaging spectrograph (Acton 2300, Princeton Instruments), and spectral data were collected on an electron multiplying charge-coupled device (EMCCD) (1 s integration time, Gain 100; Andor iXon). Background spectra collected from nearby positions with no nanodisk on the spectro-

graph entrance slit were subtracted from measured spectra, and all data were divided by the broadband spectrum of the halogen light source and any additional neutral density filters to correct for the system spectral efficiency.

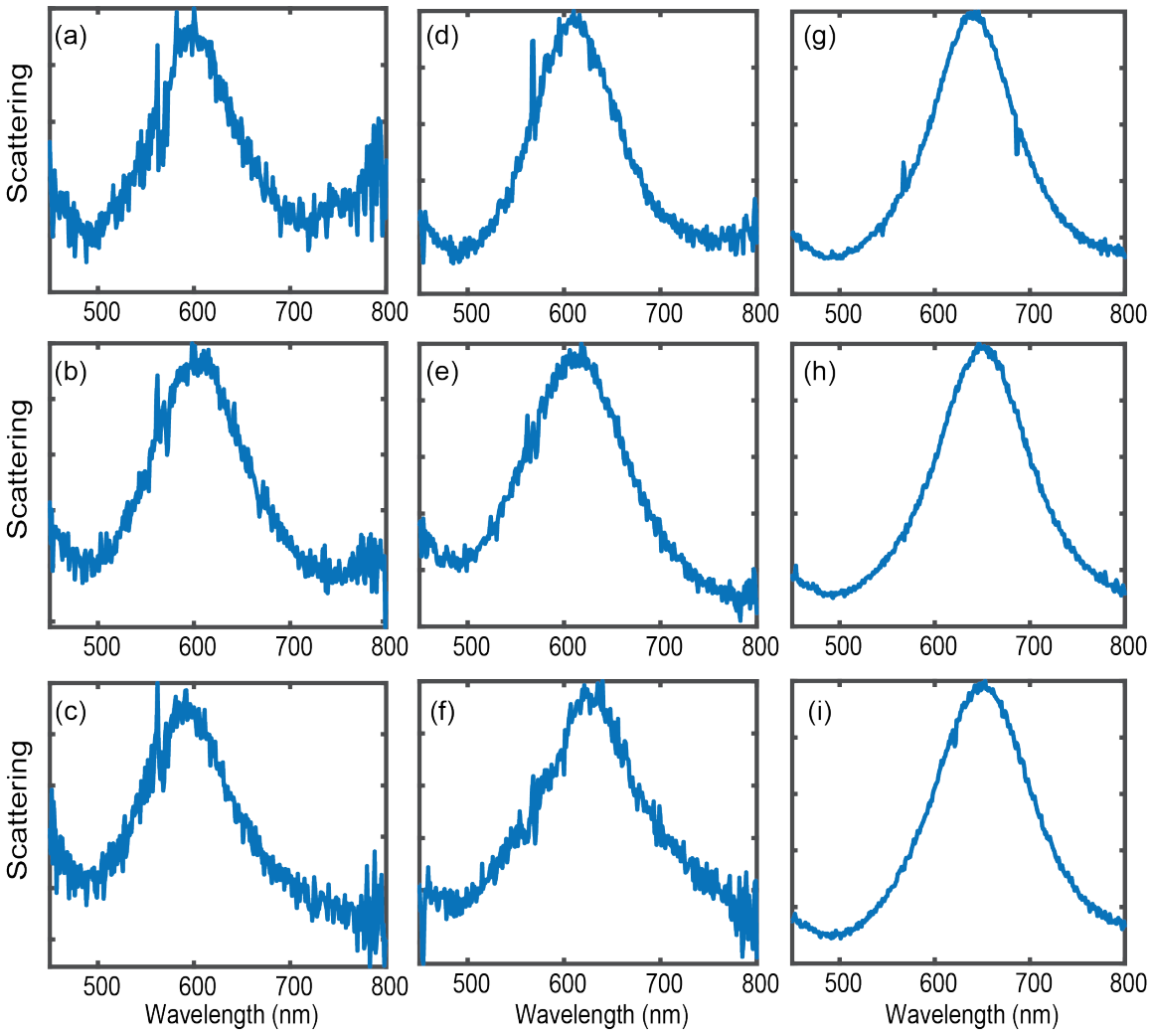

Figure 3.11: **Dark-field scattering spectra of 3 different sizes nanodisks.** a-c are for 70-nm nanodisks. d-f are for 76-nm nanodisks. g-i are for 86-nm nanodisks.

The EBL pattern was designed to create nanodisks with nominal sizes of 70, 80 and 90 nm. Then the actual size of nanodisk in each array was determined by matching the average dark-field scattering spectrum of each size to the scattering spectrum from the simulation (Fig. 3.12). The best matching results from the simulation are: 70 nm, 76 nm and 86 nm respectively.

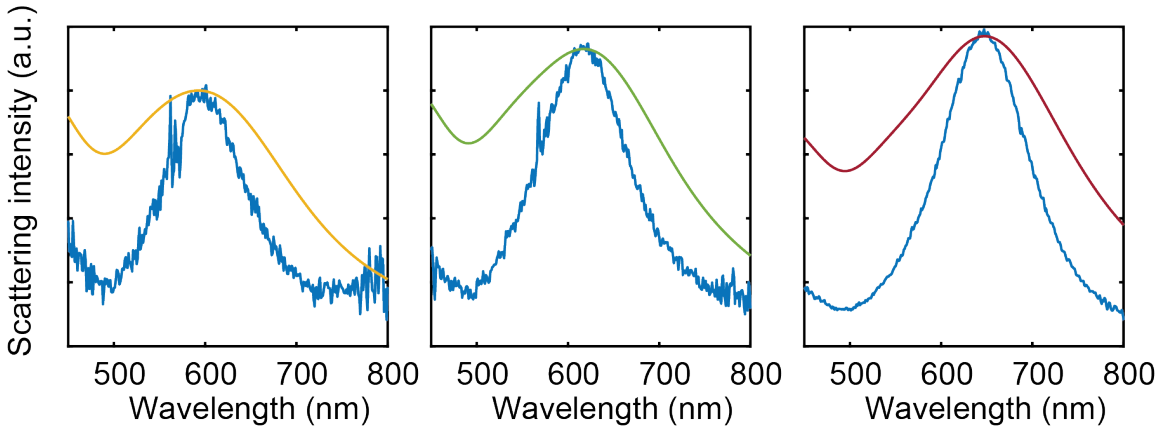

Figure 3.12: **Scattering spectra from simulation and the average dark-field scattering spectra of 3 different sizes nanodisks.** Blue curves dark-field scattering spectra. The yellow, green and red curves are the scattering spectra from simulation for 70-nm, 76-nm and 86-nm nanodisks, respectively.

The thickness of the top SiO_2 layer and the gold layer were characterized by ellipsometry (Woollam M-2000 Ellipsometer). As the polarized light beam is reflected by a sample, the polarization will be altered depending on the thickness of each layer in the sample. Delta and psi are the two variables measured for the change in polarization. Those two variables were measured as a function of the wavelength of light reflected off of the control sample. A large bare coverslip was coated with gold and SiO_2 under the same condition as the nanodisks fabrication. The thickness of the gold layer and SiO_2 was extracted by fitting the measurement to a gold-SiO_2 two-layer model. The fit results: Mean Squared Error=17.440, SiO_2 layer thickness: 191.00 ± 0.586 Å and gold layer thickness 365.75 ± 2.006 Å.

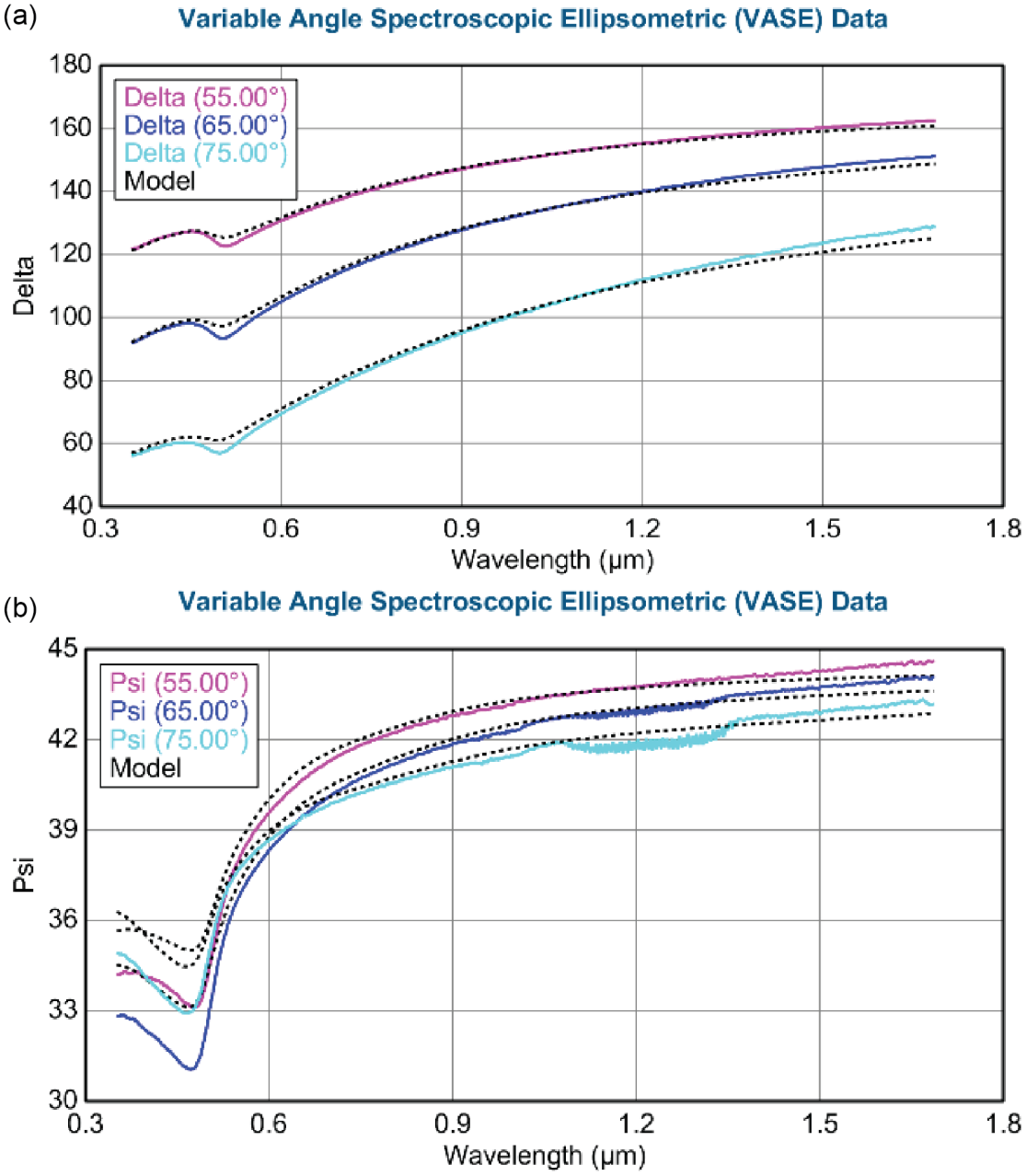

Figure 3.13: **Delta and psi vs. wavelength.**

The size and shape of gold naondisks were characterized by scanning electron microscope (SEM) with 5 kV accelerating voltage and 6600 nA (SU8000, Hitachi High Technologies America, Inc.).

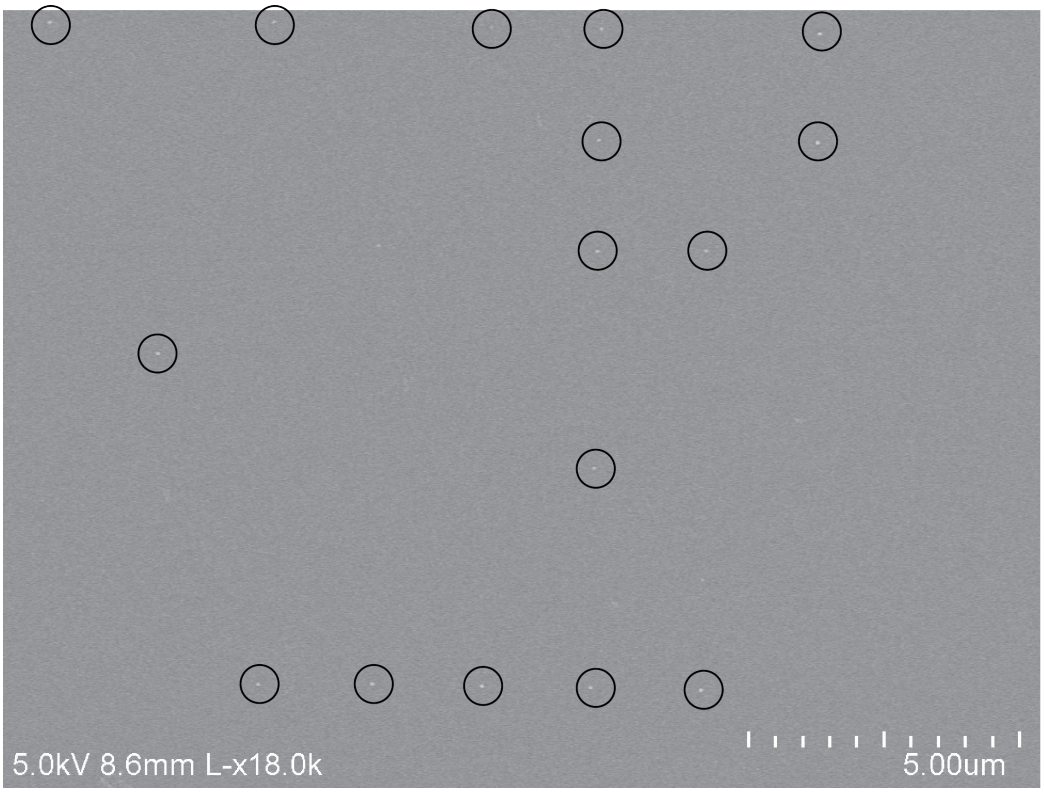

Figure 3.14: **SEM image of a 70-nm gold nanodisk array.** The nanodisks are circled here as a big part of the nanodisks in this array did not show up after the EBL which is normal during EBL process when making features with small sizes.

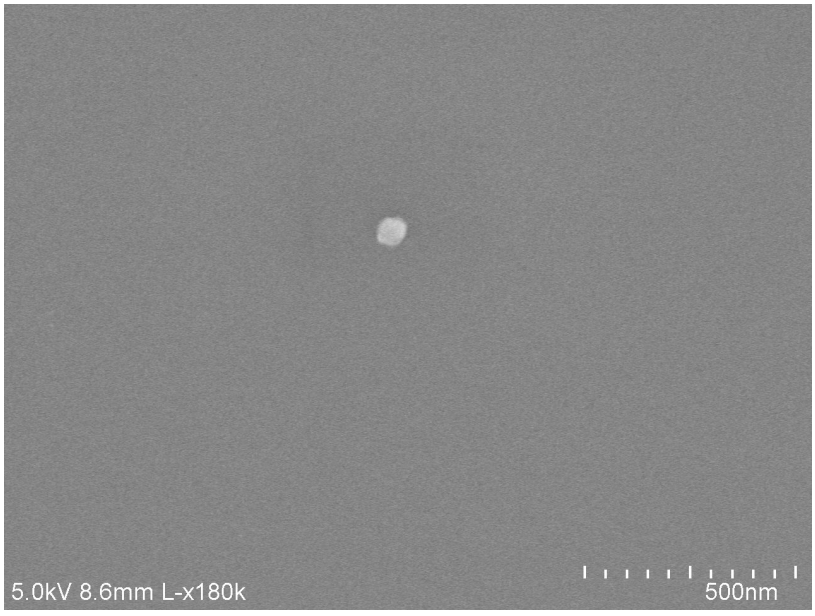

Figure 3.15: **SEM image of a 70-nm gold nanodisk.**

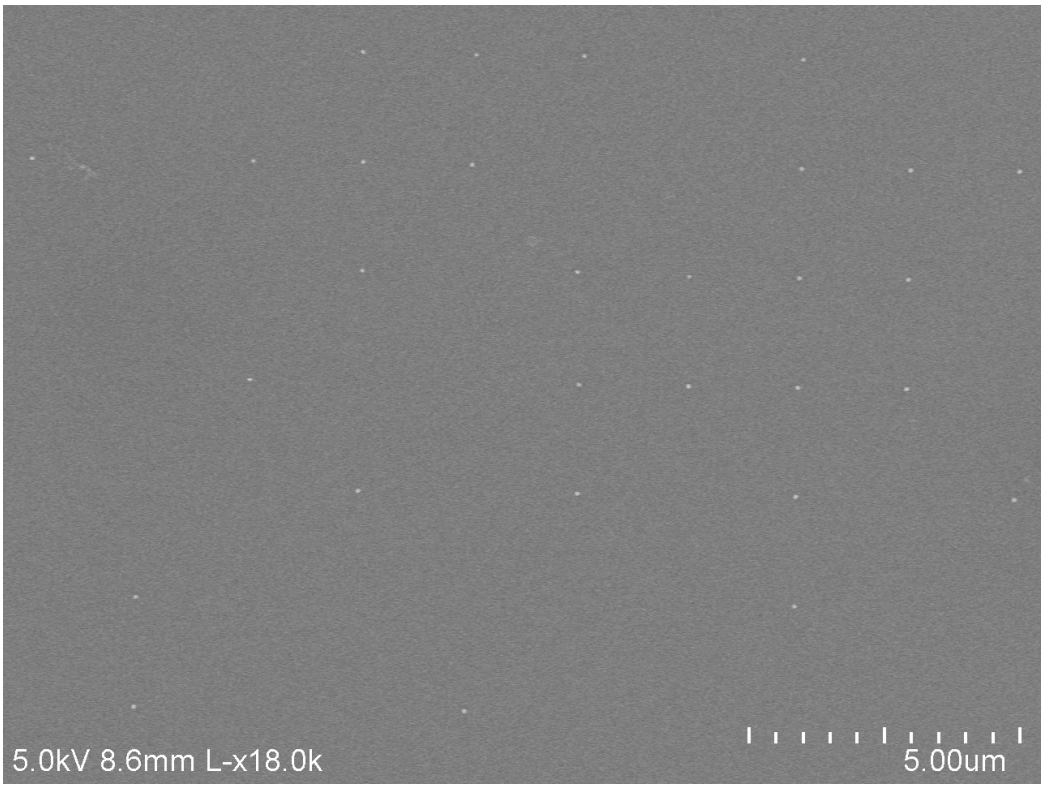

Figure 3.16: **SEM image of a 76-nm gold nanodisk array.**

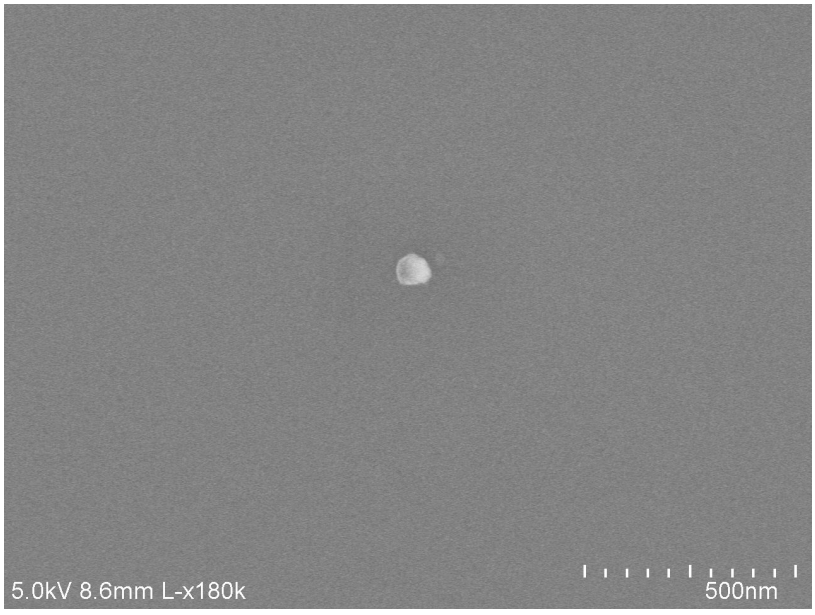

Figure 3.17: **SEM image of a 76-nm gold nanodisk.**

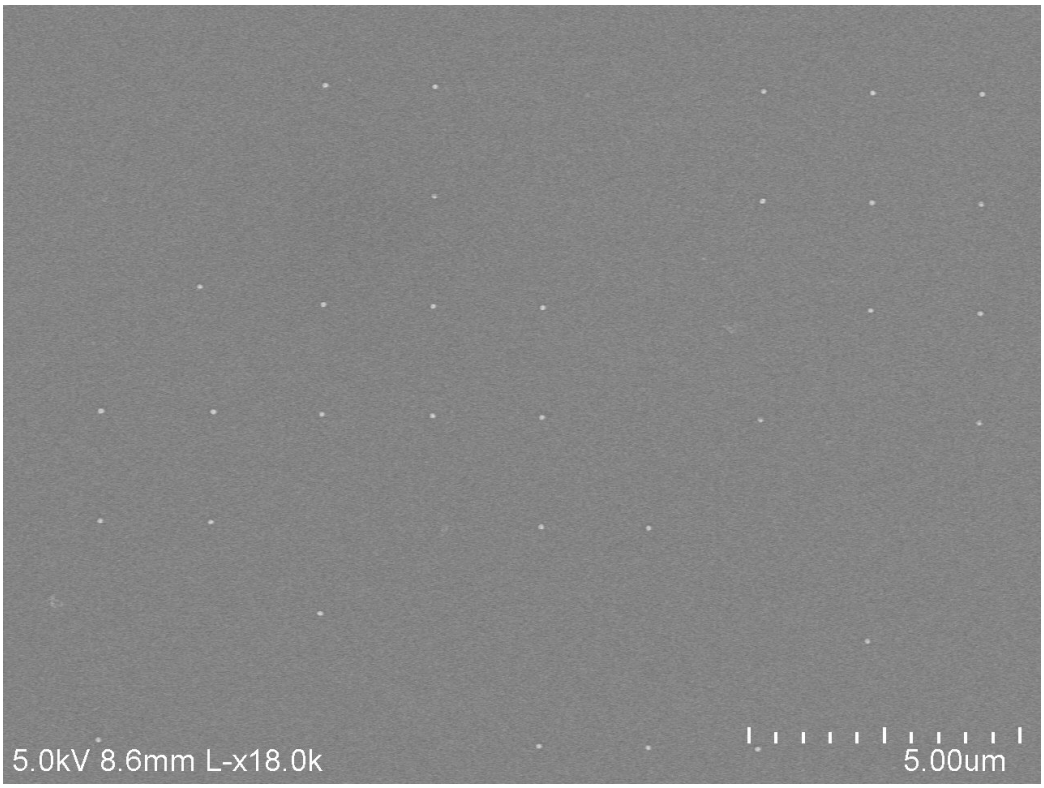

Figure 3.18: **SEM image of a 86-nm gold nanodisk array.**

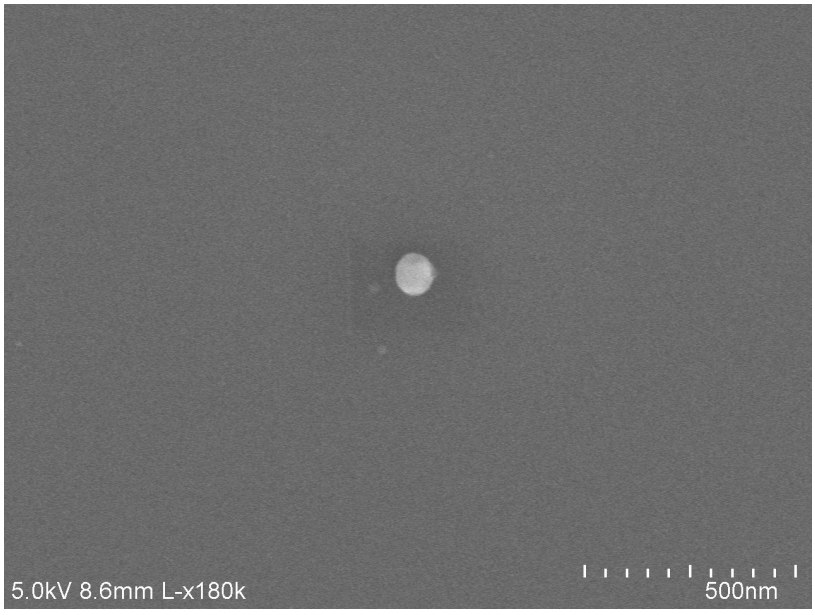

Figure 3.19: **SEM image of a 86-nm gold nanodisk.**

CHAPTER IV

Towards Plasmon Enhanced Quantum Dot Super-Resolution Imaging

4.1 Introduction

[1] Plasmon enhanced super-resolution is a great goal, however, the mislocalization that occurs upon emission coupling makes it problematic to achieve this goal. Plasmon-enhanced fluorescence can occur through a combination of plasmon-enhanced absorbance and plasmon-enhanced emission. Previously we found that mislocalization is due to the emission coupling, but that this mislocalization does not occur upon absorption coupling (Chapter III and [72]). Therefore, one way to avoid mislocalization is to decouple the emission enhancement from absorption enhancement. In other words, we aim to select the dye and plasmonic particle in such a way that the emission spectrum of the dye is strongly red shifted with respect to the localized surface plasmon resonance (LSPR) frequency to decouple the dye emission from the LSPR while the fluorescence can still be enhanced through absorption coupling [51, 75]. However, the linewidth of the LSPR is broad and the excitation and emission spectra of organic dye molecules are not very well separated which makes it hard to avoid the emission coupling.

Quantum dots (QDs), semiconductor nanoparticles, on the other hand, are a promising

[1] TZ and Kaitlyn Lhiva both designed and carried out the experiments, analyzed data with the guidance from JSB. All authors discussed the results and analysis, developed conclusions, and edited this chapter.

candidate from this decoupling purpose. One distinct feature of QDs is that they have a very sharp emission spectrum and a very broad absorption spectrum [115]. Fig. 4.1 shows the absorption and emission spectrum of water soluble CdSe/ZnS QDs purchased from NNCrystal USA. The narrow emission spectrum (red line) and broad absorption spectrum (purple line) enable absorption coupling with plasmonic particles that have LSPR in the bluer region such as 80-nm silver nanospheres (blue line). Another advantage of silver is that the LSPR strength should be higher than that of gold.

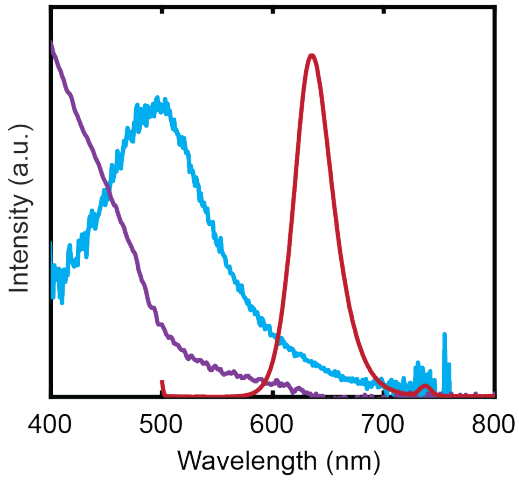

Figure 4.1: **Absorption and emission spectra of red QDs and silver particle dark-field scattering spectra.** The purple line and red line arethe absorption and emission spectrum of water soluble red emission CdSe/ZnS QD respectively. The blue line is the dark-field scattering spectrum of a 80-nm diameter silver nanosphere.

This chapter is aimed at exploring the methods of doing single-QD imaging in the presence of plasmonic nanoparticles. The discussion in this chapter lays down some groundwork for ultimately using QDs for mislocalization reduced plasmon enhanced super-resolution imaging.

4.2 Oxidation of silver nanoparticles

Silver nanoparticles can support plasmon resonances in the visible range. Compared to gold nanoparticles, they go to bluer wavelength (down to 350 nm [46]). However, silver nanoparticles get oxidized easily under light exposure which reduces their LSPR strength [116–119]. Fig. 4.2 shows the dark-field scattering spectra of a silver nanoparticle taken at different time points. To mimic the single-molecule imaging condition, the 488-nm laser was on with the same power as in a typical imaging experiment. It is clear in Fig. 4.2 that the scattering spectrum gets broader and weaker especially after an hour of illumination which agrees with the literature [119].

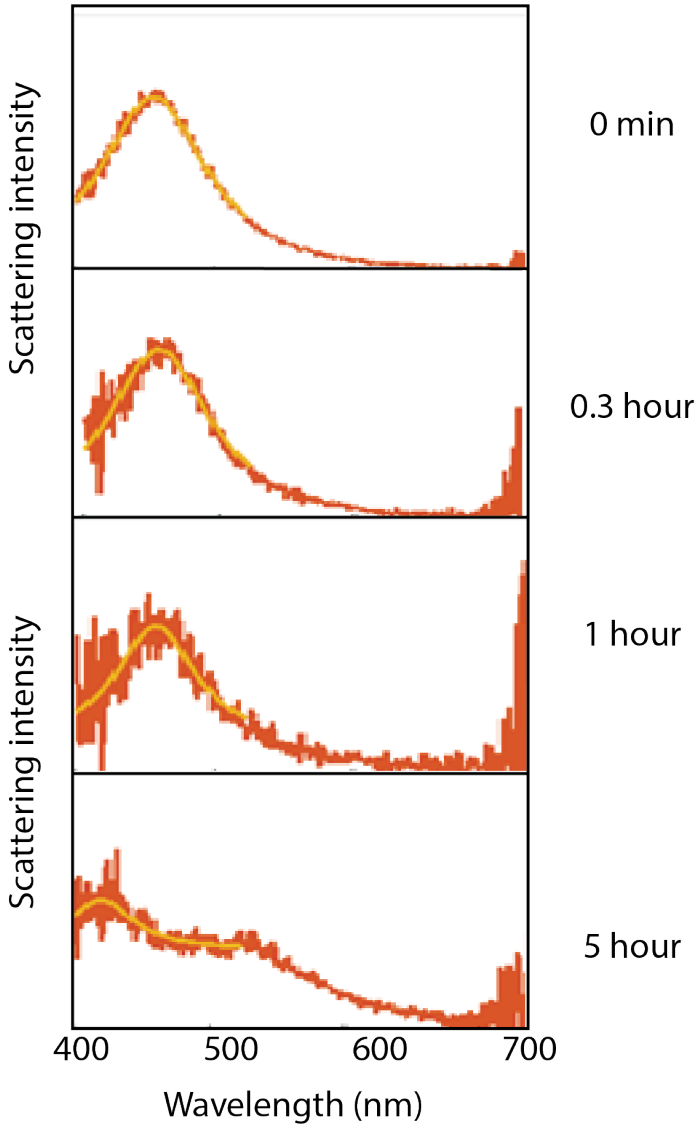

Figure 4.2: **Single silver particle dark-field scattering spectra.** Single silver particle dark-field scattering spectra taken at 0 hour, 0.3 hour, 1 hour and 5 hour of illumination, respectively. 488-nm laser was used with the power of 14 $\mu W/\mu m^2$. The yellow lines are a Lorentzian function fit to each spectrum.

To make silver nanoparticles robust candidates for fluorescence enhancement, silver oxidation needs to be prevented. One easy way suggested by the literature is that removing the ultraviolet and blue light (< 495 nm) in the illumination will significantly decrease the photo-oxidation [119]. In order to fully excite the plasmon resonance of a silver particle with redder illumination, we would need to select silver particles whose LSPR frequency is redder than 495 nm. But the goal of this experiment is to use bluer plasmonic nanoparticles. Therefore, the trade off of using redder silver particle will make it possible to overlap more with the QDs emission spectrum, which defeats the purpose. Some middle ground could be possibly achieved here by using dark red emission QDs (680 nm).

Using appropriate surfacants that protect the silver nanoparticles against photo-oxidation is another approach [119–121]. Polyvinylpyrrolidone (PVP) and citrate for example, can effectively slow down the photo-oxidation. However, even in the presence of these surfacants, the LSPR strength of silver still drops significantly within a couple hours [119]. Besides these two methods, another strategy is coating the silver surface with a protective passivating layer is another strategy such as a thin layer of SiO_2 [122] and a monolayer of graphene [123]. While SiO_2 coated silver nanoparticles are commercially available, the thin layer of SiO_2 offered in the market might still be too thick for optimal plasmon enhancement (>20 nm). A monolayer of graphene on the other hand, can be as thin as 1 nm. However, it requires a furnace for graphene deposition [123].

4.3 Different approach of single-QD imaging techniques

Compared to organic fluorescent probes, QDs are more photostable and have high quantum yields and therefore QDs have also been used an imaging probe for super-resolution over the past decade [124–126]. In this section, I introduce different methods that I have used to attempt to adapt our protocols for imaging QDs.

4.3.1 Single-QD imaging via PAINT

As I explained in Chapter II, points accumulation for points accumulation for imaging in nanoscale topography (PAINT) is a simple approach for doing single-molecule imaging. It relies on the non-specific binding between the substrate and the molecules. Fluorescence signal can be recorded when a molecule is adsorbed on the substrate (on time). Then the signal is off when the molecule photobleaches or desorbs from the substrate. The on time in single-molecule imaging mentioned in Chapter III is around 1 second. The surface chemistry alters the binding behaviors. The hypothesis is that a hydrophilic surface attracts polar molecules and a hydrophobic surface attracts non-polar molecules.

Consequently, I evaluated whether I can perform single-QD imaging by using PAINT. Nanomolar concentrations of QDs solution (100 μL) was dropped onto the coverslip with different surface chemistry for comparison. The O_2 plasma etched coverslip is very hydrophilic. After dropping QDs on the surface, the water soluble QDs tended to stick on the surface until they photobleached (around 10 seconds) because they can still be seen after bleached under microscope via dark-field imaging. This long sticking time makes the PAINT experiment less efficient. In other words, it takes much longer to collect enough data to appropriately sample. To make the surface less hydrophilic, instead of plasma etching, the coverslip was cleaned by sonicating in acetone and then water for 10 minutes. Fig. 4.3 shows one frame of the movie. At least 5 events can be seen in this 12 x 12 μm^2 frame. The on time for QDs adsorbing to this surface is much less than it was for QDs adsorbing on the plasma etched surfaces (0.5 seconds). However, the background signal is relatively high as cleaning with acetone is not as effective as plasma etching in terms of getting rid of the fluorescent background that was on the coverslip.

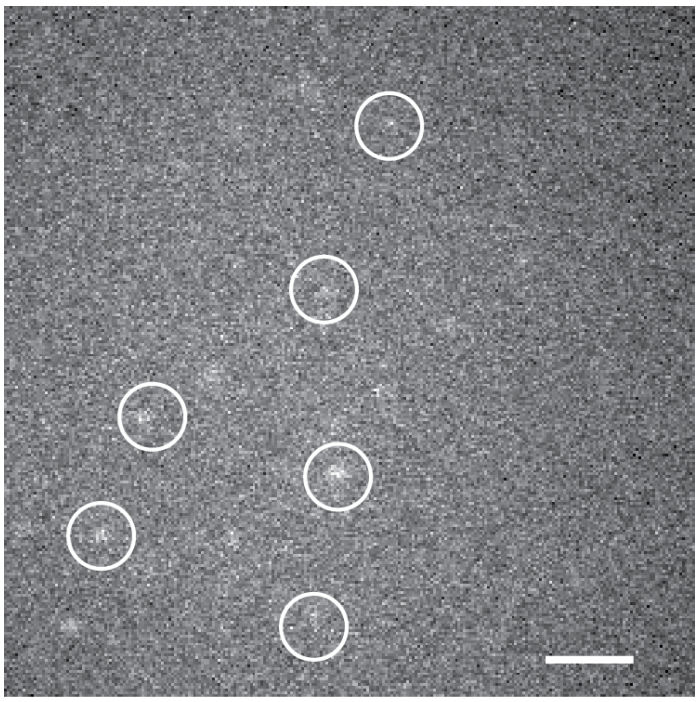

Figure 4.3: **A frame of a PAINT movie on an acetone washed coverslip.** The single-QD adsorption events are circled with white circles. A 488-nm laser was used with the power of 14 $\mu W/\mu m^2$. The scale bar is 2 μm.

The next thing I tried is functionalizing the coverslip with hexamethyldisilazane (HMDS) to make the slides more hydrophobic. Fig. 4.4a shows the water contact angle of a HMDS coated coverslip (left) compared to a plasma etched coverslip (right). The high water contact angle indicates that the HMDS was successfully coated onto the coverslip. Fig. 4.4b shows one frame of the movie recorded for QDs adsorbing on the HMDS coated coverslip. The PAINT experiment behavior is similar to the acetone washed case. One advantage of using this method is that the background noise is less than the acetone washed ones due to the fact that the HMDS coated coverslip was plasma etched before coating the HMDS (see Methods section).

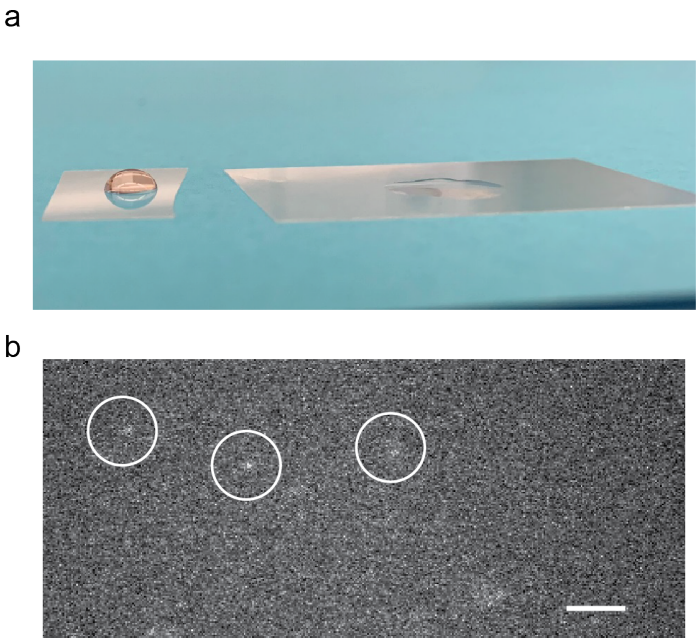

Figure 4.4: **A frame of a PAINT movie on a HMDS coated coverslip.** a shows a water droplet on a HMDS coated coverslip (left) and on a o_2 plasma etched coverslip (right). In b, the single-QD adsorption events are circled with white circles. 488-nm laser was used with the power of 14 $\mu W/\mu m^2$. The scale bar is 2 μm.

Overall, these surface treatments are able to yield the desired PAINT behavior to some extent. However, they are not very reproducible. I found that the brightness and the sticking behavior of the QDs was very different even when following the same protocol. One hypothesis is that the ion concentration in the solution plays a important role here. Increasing number of sticking events have been seen when 20 μL 2 M NaCl was added into the imaging solution. Adjusting the ion concentration and pH of the imaging solution might be a way to increase its reproduciblity in the future.

4.3.2 Single-QD imaging via blueing

Anther single-QD imaging methods is QD blueing method [127,128], which utilizes the blueing nature of the CdSe/ZnS QDs [129–131]. Upon excitation, the CdSe core is oxidized due to photooxidation [131–133]. The emission spectrum peak gradually shifts bluer as the size of the core shrinks (Fig. 4.5a). The blueing will keep happening until the quantum

dot gets photobleached. Assuming that 3 quantum dots locate within a diffraction-limited area (Fig. 4.5b) and they initially emit red light of the same wavelength, without blueing, the three QDs can not be resolved with optical microscope. However, as the blueing starts to happen stochastically, the signal from the QD which blues first can be captured with a yellow bandpass filter, which blocks the red light from the other two particles. The signal will not disappear until the first QD becomes too blue to pass the bandpass filter. Then the second QD to blue will be seen as it starts to blue. This blueing process is repeated until all the particles blue past the bandpass filter wavelength. The blueing speed can be controlled by the excitation intensity. With the right laser power and correct bandpass filter, single-QD super-resolution imaging can be achieved. In our experiments, we used laser powers of 15 $\mu W/\mu m^2$ and observed blueing rates of 0.6 nm/s. Additionally, the photoluminescence (PL) intensity of QDs fluctuates naturally [134] which is also known as blinking. This blinking results the signal in the intensity readout going up and down (Fig. 4.5b). While lots of efforts goes into making QDs less blinky, the blinking nature helps with single-QD imaging here. For example, if multiple QDs under the same diffraction-limited spot blue at the same time, it is possible to separate their emission temporarily as they turn on and off at different times.

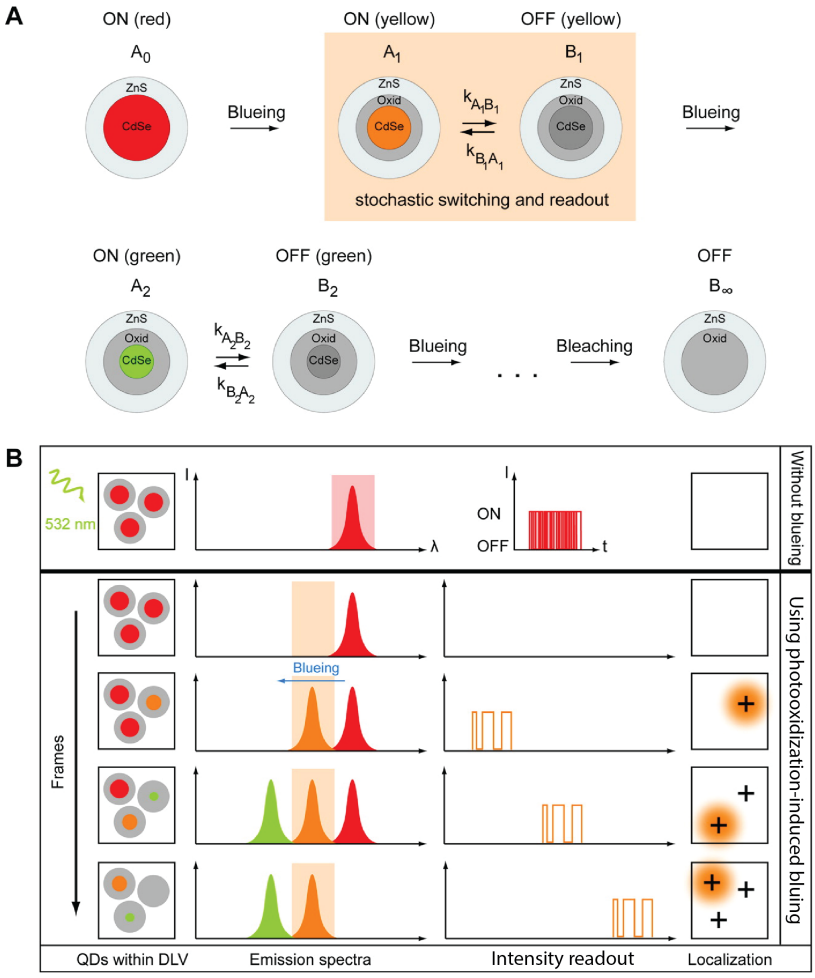

Figure 4.5: **Single-QD super-resolution imaging by blueing.** A is a cartoon illustrating the blueing of a red-emitting QD. B explains how single QD imaging is achieved. DLV stands for diffraction-limited volume. This figure is reproduced from Hell *et al.* [127].

In order to perform single-QD imaging via QD blueing, a single layer of QDs was functionalized onto silanized coverslip through 1-ethyl-3-(-3-dimethylaminopropyl) carbodiimide hydrochloride (EDC) and N-dicyclohexyl carbodiimide (NHS) coupling [135] (see Methods for details). Then the sample was imaged under 488-nm laser excitation (6 $\mu W/\mu m^2$) with a 560 nm longpass filter to characterize the uniformity of the single-layer. Fig. 4.6a shows the first frame of the single-QD imaging movie and Fig. 4.6b shows the frame after 10 seconds. It clearly shows that the QDs signals disappear in the center of the view. One possible explanation for this is that immobilized QDs desolved back into the water. To silanize the coverslip, we used (3-aminopropyl triethoxysilane (APTES) aqueous solution (see Method). However, it has been reported that the aminosilane desorps from the substrate significantly after 10 minutes in the water [136]. Consequently the second step, linking QDs to the silanized surface was less effective. In order to slow down the desorption rate, one might consider using APTES in toluene instead of in aqueous solution. It has been reported that the aminosilane layer can last up to 1 hour following toluene based APTES functionalization [136].

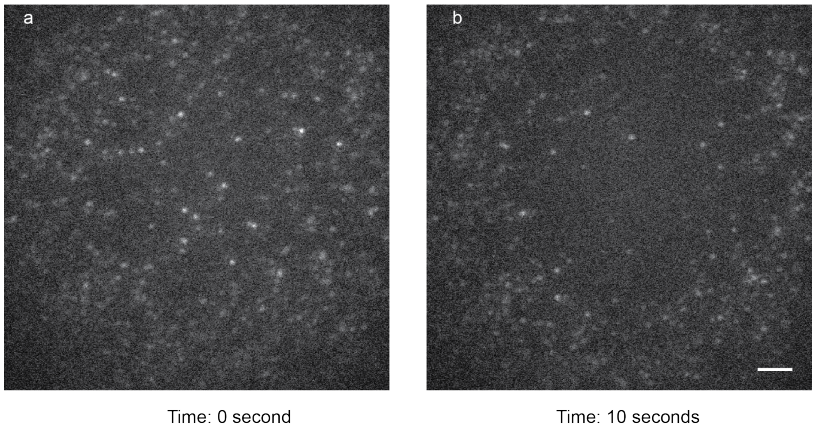

Figure 4.6: **Single-layer QD imaging.** a. The first frame of single-QD imaging. b. The frame of single-QD imaging after 10 seconds. The scale bar is 2 μm.

There are other approaches to coating a single layer of QDs onto the coverslip that worth exploring in the future such as mixing QDs into a polymer and then spin coating them it onto the coverslip [77].

4.4 2-channel single-QD imaging for QD blueing

Although the single layer coating procedure I established was not ideal, it is necessary to study how plasmonic particles can alter the QD blueing as a reference for people in the future who want to fine tune and design plasmon enhanced single QD imaging via QD blueing. 2-channel epifluorescence microscope was designed to study how the plasmonic nanoparticles affect QDs blueing. This A 2-channel setup is adapted from that described by a previous lab member Stephen Lee [137]. The excitation setup is an epifluorescence microscope, as described in the previous two chapters. At the emission end, a 70/30 beam splitter splits the beam into 2 channels (Fig. 4.7a). One goes to the camera for imaging and the other goes to the spectrometer so the single-QD spectrum and image can be collected simultaneously. In the imaging channel, the 30% reflected light was imaged on an electron multiplying charge-coupled device (EMCCD) detector (Andor iXon 897) with 100-ms exposure time. The other 70% of the signal was focused in the horizontal direction through a 350-nm slit and dispersed by a spectrometer (Princeton Instruments SP-2300i, 150/500 nm grating) onto a second EMCCD detector (Andor iXon 887). The camera in the spectrum channel is triggered by the imaging channel. 40-nm diameter and 80-nm length gold nanorod (nanopartz, Z12) was chosen as its LSPR peak is at 640 nm, matching well with the CdSe/ZnS QD (NNCrystal CWZ 650) emission (Fig. 4.7b). Fig. 4.7c shows a single frame of image and spectrum collected from the 2 channels simultaneously. The left is from the imaging channel and the right is from the spectrum channel. In the spectrum channel, the horizontal direction is the wavelength, centered at 630 nm and the vertical direction is the y position. Under 561-nm laser excitation, the gold nanorod can been in both channels due to its PL (Fig. 4.7c orange box).

Single-QD imaging is achieved by the PAINT method on plasma etched coverslips (see Method section for details). As I showed in the section above, QDs adsorb and don't desorb on the plasma etched coverslip, therefore I could observe them after adsorbing until photobleaching which is ideal for spectral characterization for blueing. Fig. 4.7d shows

another frame captured in the same position when two single QDs were adsorbed onto the coverslip surface. The blue box indicates a nanorod-coupled QD (localized within 100 nm of the gold); the green box indicates a QD that is too far from the nearest nanorod for coupling to occur. Over time, the QD spectrum information and intensity information can be collected and studied.

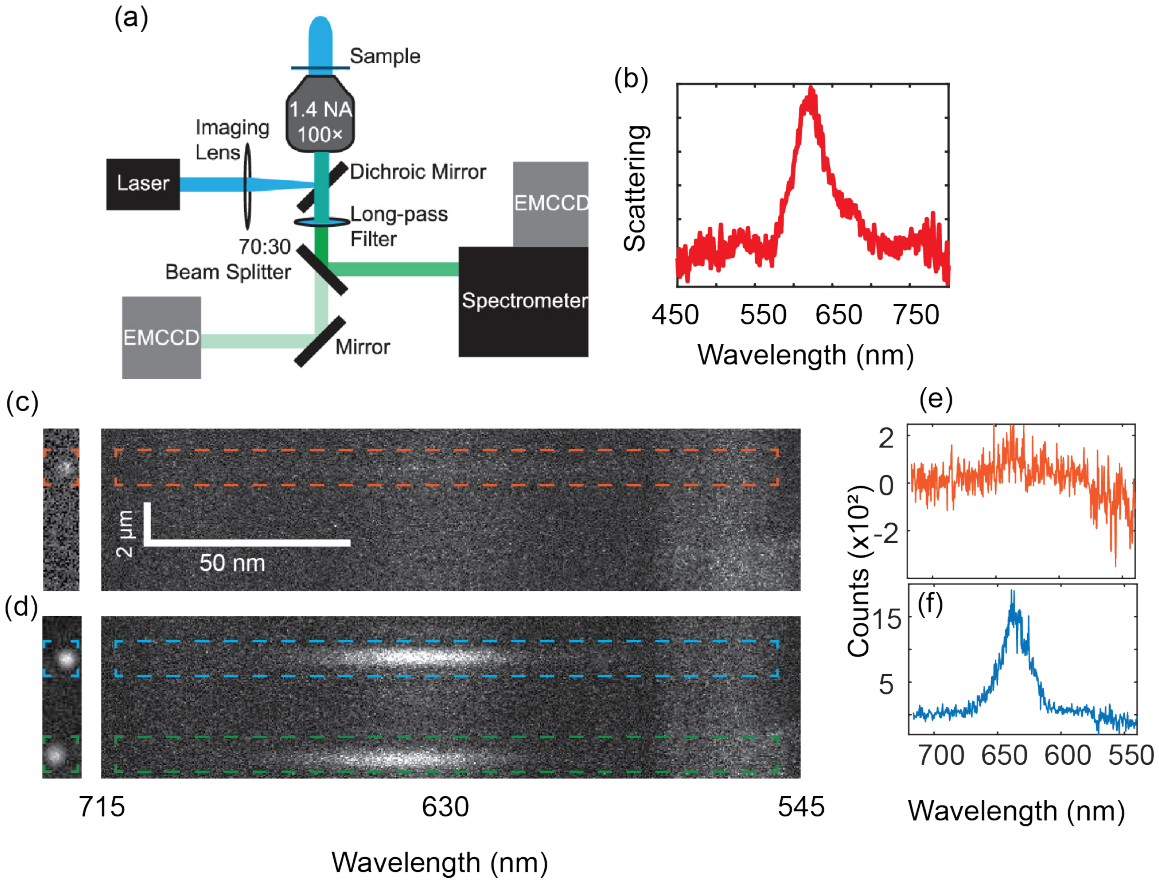

Figure 4.7: **2-channel single-QD imaging setup.** a. Schematic of the 2-channel epifluorescence microscope. b. dark-field scattering spectrum of a 40-nm diameter and 80-nm length gold nanorod. c. a frame of the 2-channel imaging. Au PL image and spectrum are showed in orange boxes. d. a frame of the 2-channel imaging. The images and spectra of the QDs are showed in blue and green boxes respectively. e is the background subtracted PL spectrum of the gold nanorod in the orange box. f is the background subtracted PL spectrum of the QD in the blue box. a is reproduced from Lee *et al.* [137].

As mentioned in the introduction, the core of a QD will get oxidized under laser excitation. Since the PL wavelength of the QD is proportional to its core size, this oxidation

process will cause the QD to become bluer. With the 2-channel setup, we characterized the blueing of the chosen red CdSe/ZnS QDs. Fig. 4.8 shows the spectral shift of a QD as a function of time. Specifically, Fig. 4.8a shows the colormap of the spectral change with x direction being the spectrum wavelength and y direction being the time. The colorbar indicates the emission intensity. The QD PL lasted ~6 seconds before it photobleached Fig. 4.8a. Fig. 4.8b plots the emission peak of this QD as a function of time in which we can see that the QD emission spectrum shifted ~17 nm before it photobleached. In the first 3 seconds, the QD blued slowly, changing peak wavelength at a rate of 1 nm/sec. In the last 3 seconds, this QD blued much faster, at a rate of 5 nm/sec. This two-step blueing occurs pretty consistently for all the QDs. Fig. 4.8c shows some representative spectra of the same QD at various times during the 6-second on time.

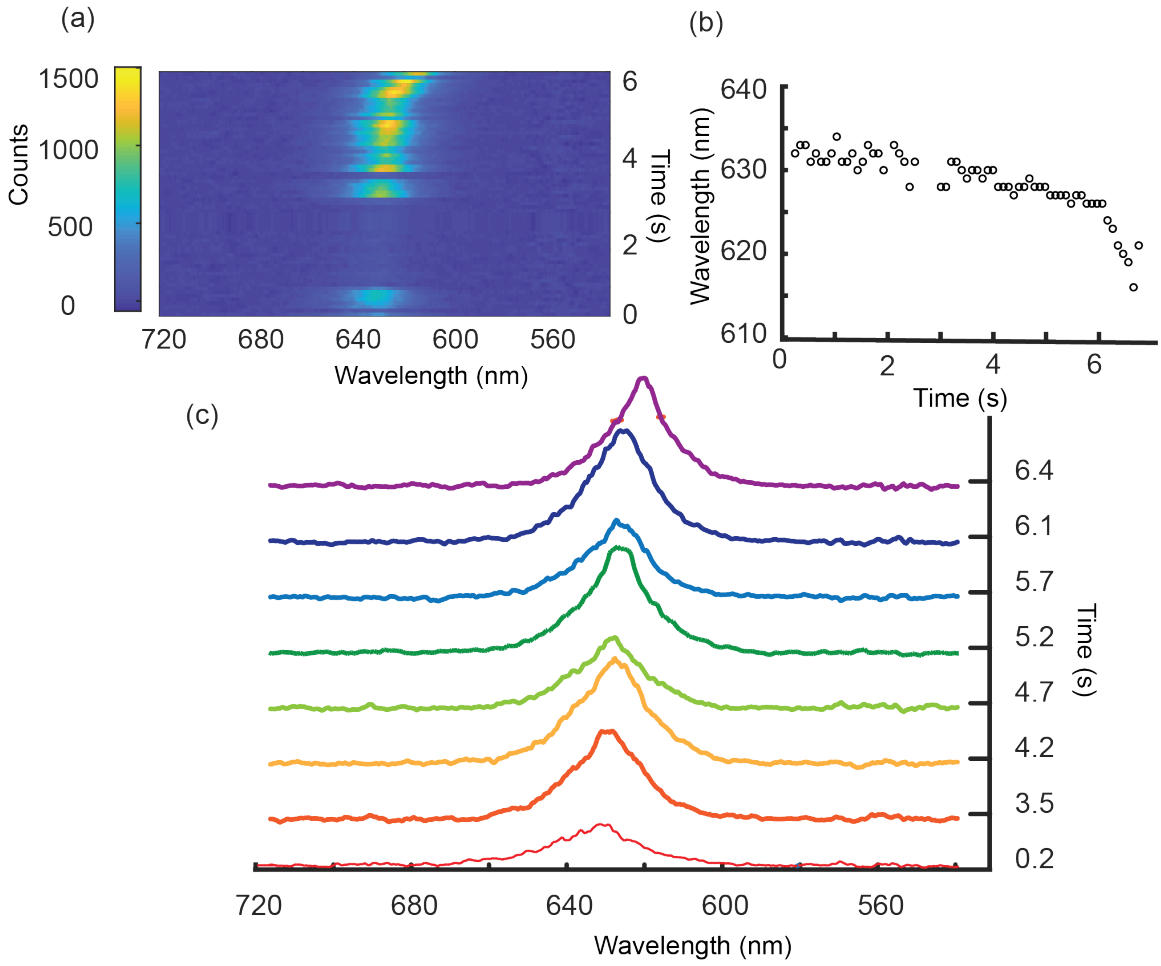

Figure 4.8: **Single-QD blueing spectra.** a shows the single-QD spectral change as a function of time. x-axis is the spectrum wavelength. The colorbar indicates the emission intensity. b plots the emission peak as a function of time. c shows some representative single-QD spectra. y-axis indicates the time point at which each spectrum was acquired.

During the process of blueing, photobleaching and blinking affects the blueing time and rate [129–131]. Fig. 4.9 - Fig. 4.11 shows the single-QD spectral blueing as a function of time from 24 representative particles. There is some noise in the determination of the peak wavelength because we are doing a Lorentzian fit to low signal-to-noise ratio data. On the other hand, we still observe significant shifts in the wavelength. In general, the QDs observed here are getting bluer (see for example Fig. 4.9b), but sometimes they get redder (see for example Fig. 4.11b), sometimes there is no significant spectral change (see for example Fig. 4.10f), and sometimes there is spectral drift back and forth (see for example Fig. 4.10d). The average spectral shift in these 24 QDs is 11 nm which agrees with reported data in the literature [138]. The average emission time before bleaching is 15.5 s with a standard deviation of 14.3 s.

The net spectral change for each QD was calculated as the median peak emission wavelength of the last few frames minus the average peak emission wavelength of the first few frames. This determination was very qualitative and could be improved in future experiments, for instance by fitting the data.

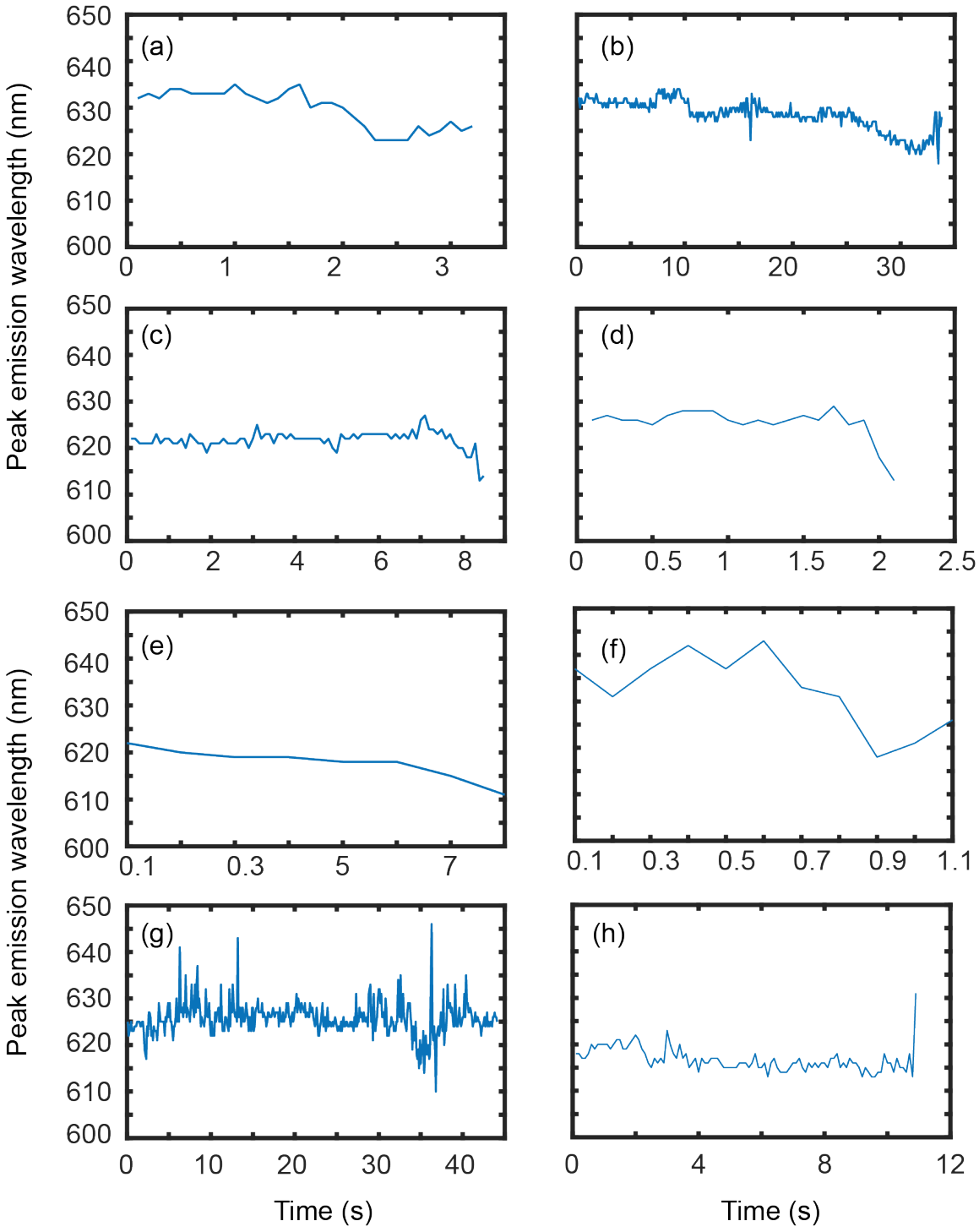

Figure 4.9: **Single-QD blueing of the first 8 QDs measured.** a-h shows single-QD emission peak wavelength as a function of time from 8 QDs.

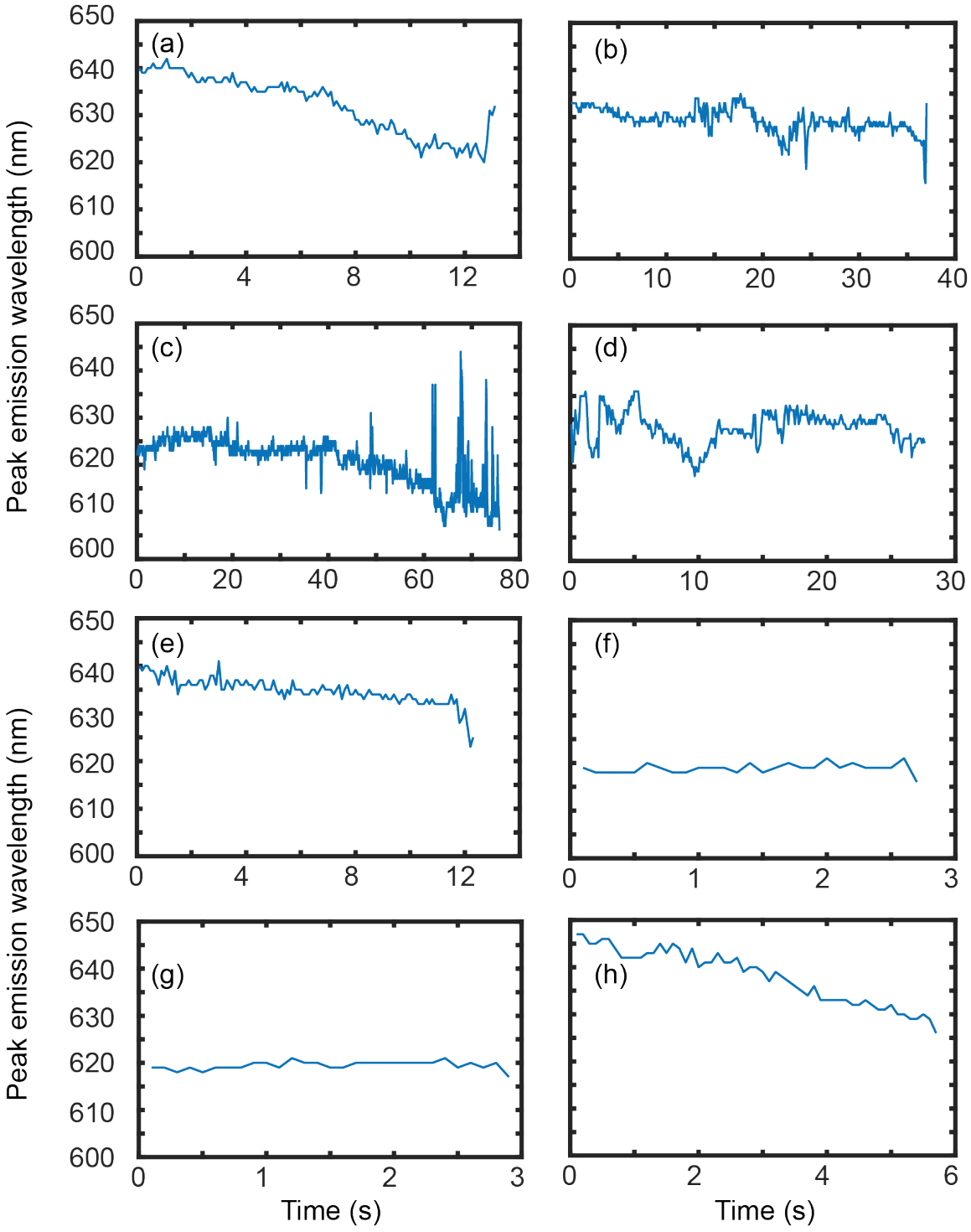

Figure 4.10: **Single-QD blueing of the next 8 QDs measured.** a-h shows single-QD emission peak wavelength as a function of time from 8 QDs.

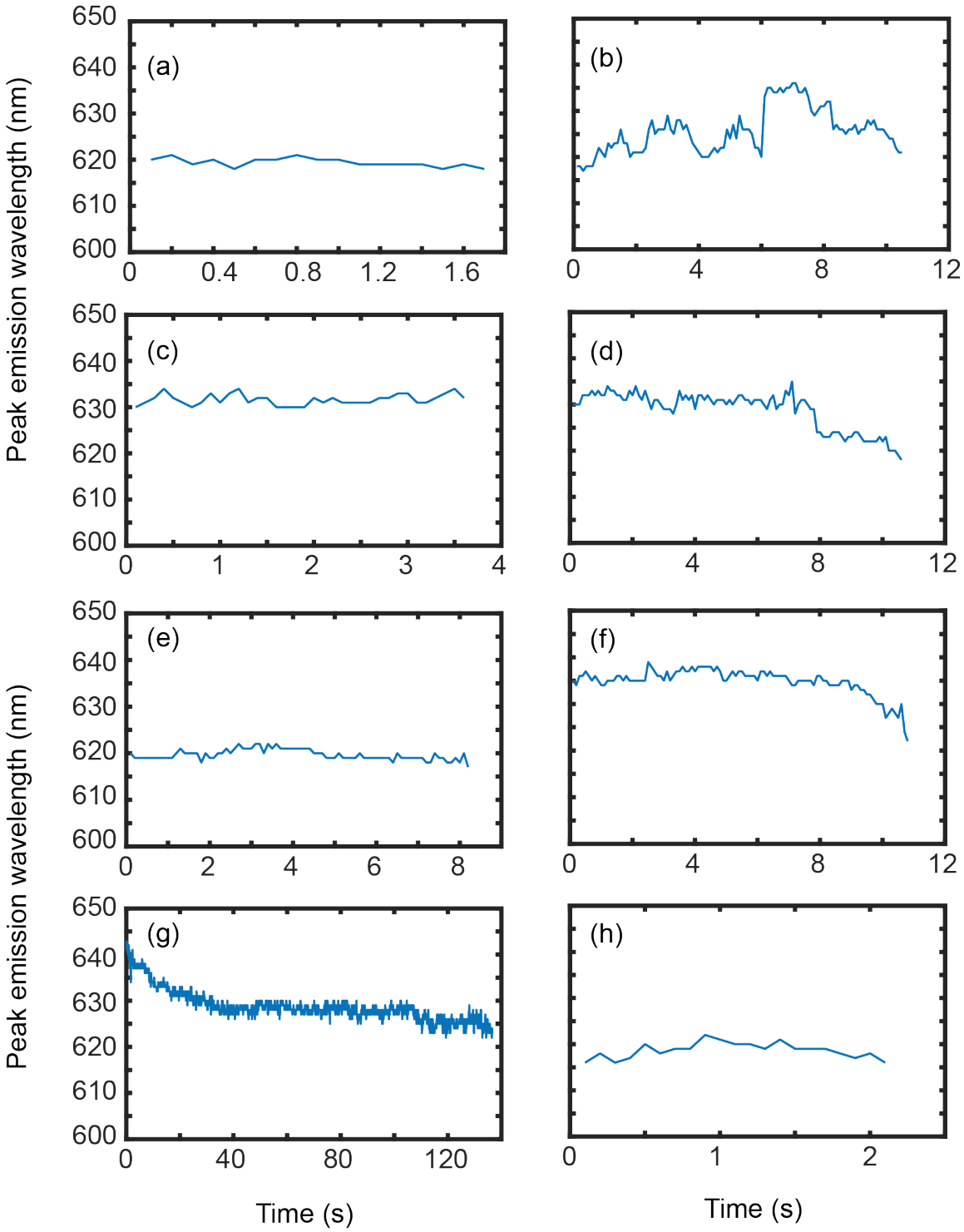

Figure 4.11: **Single-QD blueing of the last 8 QDs measured.** a-h single-QD emission peak wavelength as a function of time from 8 QDs.

We then examined the blueing of QDs localized within 100 nm of a gold nanorod, i.e., close enough for plasmon-enhanced PL to begin to be observed. We recorded the spectra for those 8 proximal QDs. The average emission time before bleaching is 12.7 seconds (standard deviation: 7.5 seconds). Although the emission time does not change significantly upon coupling, the standard deviation is reduced to half (Fig. 4.12). We were surprised that the nanparticle-coupled QDs didn't photo-oxidize faster because one hypothesis here is that upon coupling, the absorption and emission rate of the QD are both enhanced. We expected this enhanced PL rate to reduce the chance of the QD entering a triplet state in which the QDs get oxidized and photobleached [139]. To further examine this hypothesis, more data needs to be taken to make sure the difference in the standard deviation does not come from under-sampling. Additionally, it is possible that these QDs were not affected because, though close, they weren't close enough to truly couple to the nanoparticles. Therefore, we would need to verify that the emission intensity of the coupled QDs is enhanced.

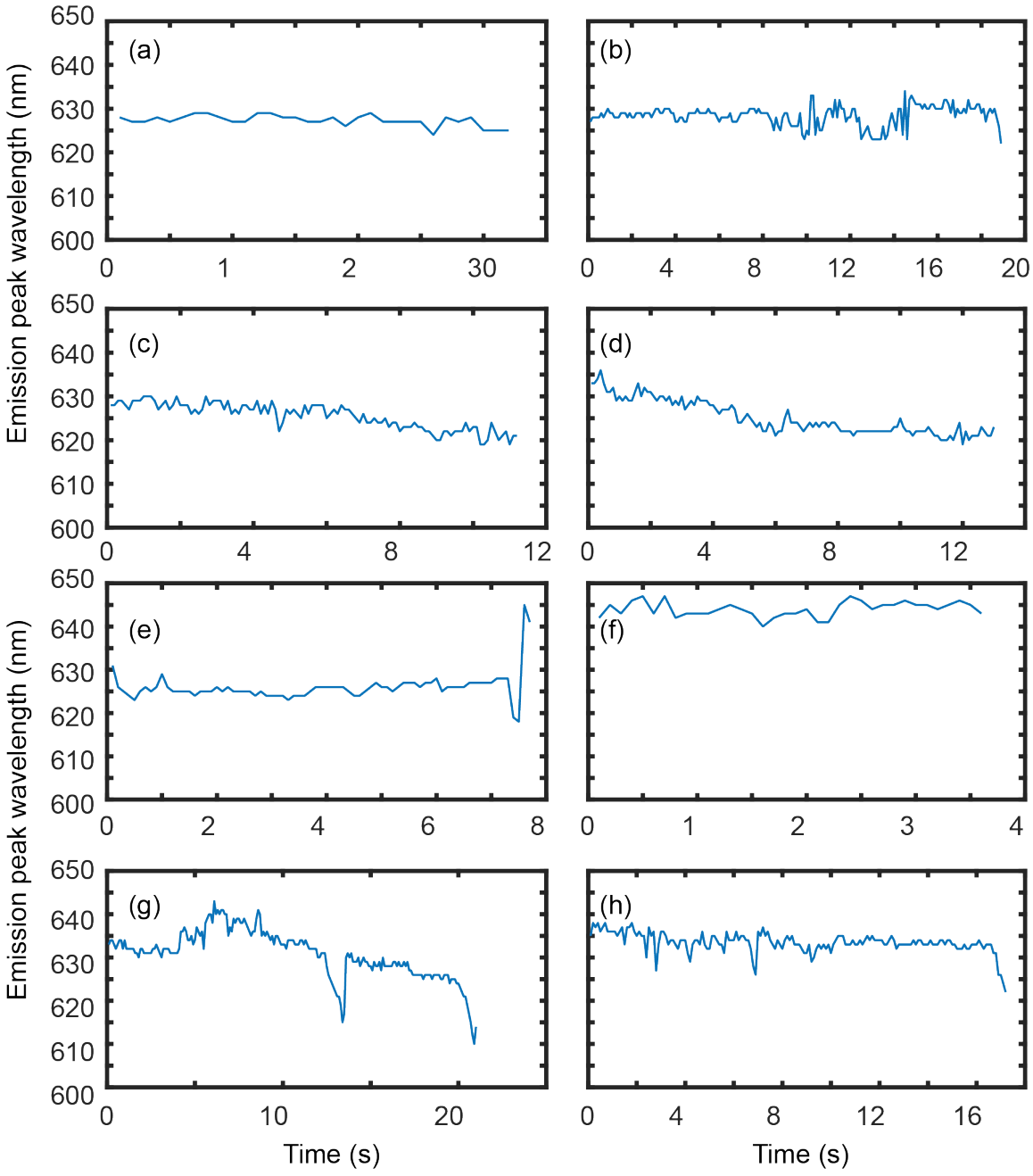

Figure 4.12: **Coupled QD blueing.** a-h shows 8 coupled QD emission peak shift as a function of time.

4.5 Methods

4.5.1 Gold nanosphere coverslip samples

The coverslips were cleaned with O_2 plasma (PE 50, PlasmaEtch Inc.) for 10 minutes. 80-nm length and 40-nm diameter nanorods (Nanopartz Inc.) were used as received. To prepare the substrate with nanorods, 10 μL of the stock solution was directly drop-casted on a microscope coverslip for 5 min. The sample was then sonicated in a beaker of deionized (DI) water for 5 minutes to wash away the nanorods that did not stick on the coverslip. The sample was then dried with nitrogen gas.

4.5.2 Dark-field scattering spectroscopy of nanoparticles

Nanorods were immobilized on glass coverslips as described. These nanorod substrates were immersed in water. A broadband halogen white light source excited the sample through a dark-field water-immersion condenser, and scattered light was collected in an Olympus IX71 inverted microscope equipped with a dark-field oil-immersion objective (NA = 0.6). The diffraction-limited image of a single nanorod was aligned to the entrance slit of an imaging spectrometer (Acton 2300, Princeton Instruments), and spectral data were collected on an electron multiplying charge-coupled device (EMCCD) (5 s integration time; Andor iXon). Background spectra collected from nearby positions with no nanorod on the spectrometer entrance slit were subtracted from measured spectra, and all data were divided by the broadband spectrum of the halogen light source and any additional neutral density filters to correct for the system spectral efficiency.

4.5.3 Single-QD 2-channel Microscopy

A 2-channel microscopy was performed with a 100x 1.30 NA oil-immersion objective in an Olympus IX71 microscope. A 75-100 μL volume of 500 nM QDs (650 nm emission wavelength, CdSe/ZnS water soluble, NNCrystal US) in water was placed on top of the

nanoparticle coated coverslip sample. The QDs were excited with a 561-nm laser light (Sapphire, Coherent) with a power of 15 $\mu W/\mu m^2$. The emission was filtered through a dichroic mirror and long pass filter set (Semrock Di01-R561 and BLP01-561). The exposure time of the cameras for both channels was set to 100 ms and the frame transfer setting were switched off on both cameras. On the spectral channel, the light was focused in the horizontal direction through a 350-nm slit and dispersed through a spectrometer (Princeton Instruments SP-2300i, 150/500 nm grating) centered at 630 nm wavelength. Therefore, in the spectrum channel, the vertical direction carries the vertical position information.

4.5.4 Single-QD spectrum and intensity analysis

The start frame and end frame of each single-QD blueing event were manually identified by observing the movies frame by frame. The vertical location each QD was first roughly guessed by eye. At that initial guess location, a window of ± 5 pixels in the vertical direction and 512 pixels in the horizontal direction was selected. The 11-pixel window size was selected such that it was big enough to include all the intensities of a QD in a diffraction-limited spot but not too big to include the signal from QDs close by. The background signal was chosen as an area nearby with the same size (512x11 pixels) where there was no QD events. The final vertical position of each QD in spectrum channel was determined by summing the pixel intensities in each window (512x11 pixels) along the horizontal direction (512 pixels) and fitting the sum to a Lorentzian function. The single-QD spectrum in each window was collected by summing the pixel intensities along the vertical direction (11 pixels). The background subtracted spectrum was then fit to a Lorentzian function to obtain the peak wavelength.

4.5.5 Single layer QDs preparation

To coat QDs on the coverslip, the coverslip was first silanized by (3-Aminopropyl)triethoxysilane (APTES) solution-phase aminosilane deposition. This pro-

cedure was adapted from refs [135, 140, 141]. The coverslip was cleaned in 100 mL Hellmanex®III and washed with water thoroughly. It was then cleaned with O_2 plasma (PE 50, PlasmaEtch Inc.). Then 2% by volume of APTES (Sigmaaldrich) in methanol was made and the coverslip was incubated in this solution at room temperature for 10 minutes. The coverslip was thoroughly rinsed with methanol several times, dried under a stream of nitrogen and baked at 110°C for 30 min.

The QDs with -COOH functional group were linked to the surface through 1-ethyl-3-(-3-dimethylaminopropyl) carbodiimide hydrochloride (EDC) and N-dicyclohexyl carbodiimide (NHS) coupling [135]. 6.38 mg EDC (ThermoFisher) in 1000 uL PBS was prepared for use (33.4 mM). 15.24 mg NHS in 1000 uL phosphate-buffered saline was prepared as stock solution (70.9 mM). 25 μL EDC stock, 15 μL NHS stock and 30 μL QD (CZW red NNCrystal US) straight from the original container without dilution were dropped on the coverslip in a beaker. The sample was incubated with gentle shaking for 1 hour in the dark. The coverslip was then rinsed with water thoroughly.

4.5.6 Making HMDS coated slides

The protocol was adapted from ref [142]. The coverslip was cleaned with O_2 plasma (PE 50, PlasmaEtch Inc.) for 10 minutes. 2 mL of HMDS (Sigmaaldrich) was added into a 500 mL glass beaker. The coverslip was taped onto a piece of aluminium foil and placed on top of the beaker with HMDS. The beaker was placed in an oven at 70°overnight. The beaker was opened in a fume-hood and the slide were removed.

CHAPTER V

Conclusions and Future Directions

5.1 Conclusions

Plasmon enhanced single-molecule imaging has a large potential to improve super-resolution imaging. In order to better control and utilize the plasmon enhancement, the light-matter interaction between plasmonic nanoparticles and single emitters needs to be understood. In Chapter II, single-molecule polarization resolved microscopy was used to understand the emission polarization change of single emitters upon coupling to gold nanorods. I performed a single-molecule experiments that showed a change in the polarization direction from dye molecules coupled to anisotropic plasmonic nanoantennas. I complemented these experiments with simulations that I showed that the coupled emission polarization is indeed predicted to rotate toward the direction of the dominant nanoantenna localized surface plasmon mode. My experimental data also informed a reduced-order analytical model, based on which I attribute this emission polarization distribution to both far-field interference and resonant coupling between the molecular dipole and the nanorod plasmon modes.

In Chapter III, I used the single-molecule imaging method of direct stochastic optical reconstruction microscopy (dSTORM) to evaluate the emission localization modification (mislocalization effect) of a single emitter coupled to a gold nanodisk made by electron-beam lithography (EBL). I demonstrated that mislocalization is the result of emission cou-

pling whereas fluorescence enhancement is the result of both absorption and emission coupling. Additionally, I applied the analytical model to recover the orientation and the localization of a single emitter in my simulations. The result from the model fitting significantly outperforms the standard Gaussian fitting.

Last but not least, in Chapter IV, I explored the application of QDs in single-particle imaging. 2-channel single-particle microscopy was performed to characterize the single particle spectral shift (bluing) upon excitation and how a gold nanoparticle affects the bluing. I indicated how it will be possible to couple QDs to silver nanoparticles to achieve plasmon enhanced fluorescence without emission coupling.

5.2 Impact

The results from the experiments and model in this thesis will make significant impact in connecting the fields between single-molecule imaging and plasmonic nanoantennas.

Single-molecule polarization-resolved microscopy enables us to understand the emission coupling between dye molecules and plasmonic nanoantennas at the single-molecule level. Experiments in a bulk scale only allow people to measure the average emission polarization, whereas the single-molecule experiments make it possible to access the details buried in the ensemble average. For instance, it allows us to study the fluorescence intensity enhancement as a function of emission polarization. We found that the most enhanced molecules are the ones that have emission polarizations aligned with the dominant mode of the nanorods. This single-molecule level polarization microscopy inspires the study the effect of nanoparticle on single-molecule emission in many ways. On one hand, it inspires us to relate the emission polarization with other properties and allows us to answer many questions such as what is the relationship between emission polarization and mislocalization and can we use use filter out those most mislocalized molecules by their emission polarization. On the other hand, it also inspires people to design many other single-molecule multi-readout experiments such as hyperspectral imaging [137].

Additionally, this type of single-molecule multi-readout experiments can be extremely useful to the development of an analytical model which aims to understand the physics behind the plasmon and fluorescence coupling. The reduced-order analytical model that my experimental data informed, provides physical insights into the emission coupling mechanism. The model will make it possible to recover the true position and orientation of the molecules in the dye/nanoparticle coupled system, making plasmon enhanced super-resolution imaging more practical. Besides recovering the true position and orientation, the model can also be used to predict the fluorescence enhancement, which will provide guidance for how to achieve optimal plasmon-enhanced fluorescence in different plasmon enhanced super-resolution imaging designs. Additionally, compared to simulations, the model is a much faster way to predict the electromagnetic properties of a coupled system, largely improving the efficiency of designing plasmonic nanoantenna related applications.

Last but not least, I also introduced a high throughput single-molecule experiment. This single-molecule experiment that allows fine tuning of the localized surface plasmon resonance (LSPR) frequency of plasmonic particles via EBL, control of the coupling distance by double stranded DNA (ssDNA) spacers and efficient single-molecule imaging through dSTORM. This high efficiency and versatile design promises to improve high-sensitivity single-molecule fluorescence imaging and biosensing.

5.3 Future directions

In Chapter III, I introduced a single-molecule imaging method which allows the scientists to control the distance between a plasmonic nanodisk and a single emitter. However, the dye molecules still have some degree of freedom in terms of rotational movement due to the single covalent bond between the dye and the dsDNA. This rotational movement can be constrained by incorporating the dye molecule into the backbone of the dsDNA [143]. For example, Fig. 5.1a from ref [143] shows that a Cy3 molecule can be covalently bound to the backbone of a single stranded DNA. The dsDNA can be formed by adding a comple-

mentary single stranded DNA (Fig. 5.1b). The movement of the Cy3 molecules is largely reduced because both ends of the Cy3 molecule are covalently linked to the phosphate backbone of the DNA.

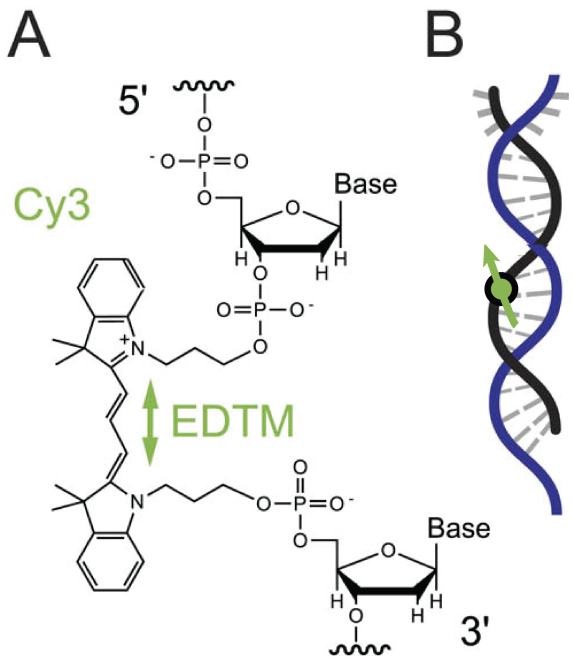

Figure 5.1: **Dye in DNA.** A shows the strutural formula of a part of single stranded DNA with a Cy3 molecule in its backbone. B is a cartoon showing the structure of a ssDNA internally labeled by Cy3. The green arrow indicates the orientation of the electric dipole transition moment (EDTM). Adapted from ref [143].

In Chapter IV, I suggested the idea of reducing mislocalization by doing plasmon enhanced super-resolution imaging with quantum dots. Following up with this idea, here, I propose a method to couple QDs to aluminum nanoparticles.

The challenge of decoupling the QD emission from the plasmon resonance is that the LSPR frequency of the nanoparticle needs to be blue enough to decouple from the emission spectrum of the QDs. Because the minimum LSPR wavelength for a gold nanoparticle is ~550 nm [47, 144], gold is it not an ideal material for this purpose. The resonance frequency of silver nanoparticles can be tuned to blue wavelengths, however, silver is easily oxidized which makes these nanoparticles unstable over the course of a typical experiment. Aluminum nanoparticles on the other hand, support plasmon resonance across

the visible range and also into the ultraviolet region [144–146]. Although aluminum also suffers from oxidization, this oxidation is self-terminating [144]. Additionally, the LSPR frequency of aluminum oxide still falls in the ultraviolet region [144]. Fig. 5.2a shows the scattering intensity of Al nanodisks with different diameters. Based on this figure, Al nanodisks with diameters from 70 nm to 100 nm would be suitable to couple to the absorption spectrum of a 590-nm emission InP/ZnS QD without significantly coupling to the QD emission spectrum (Fig. 5.2b).

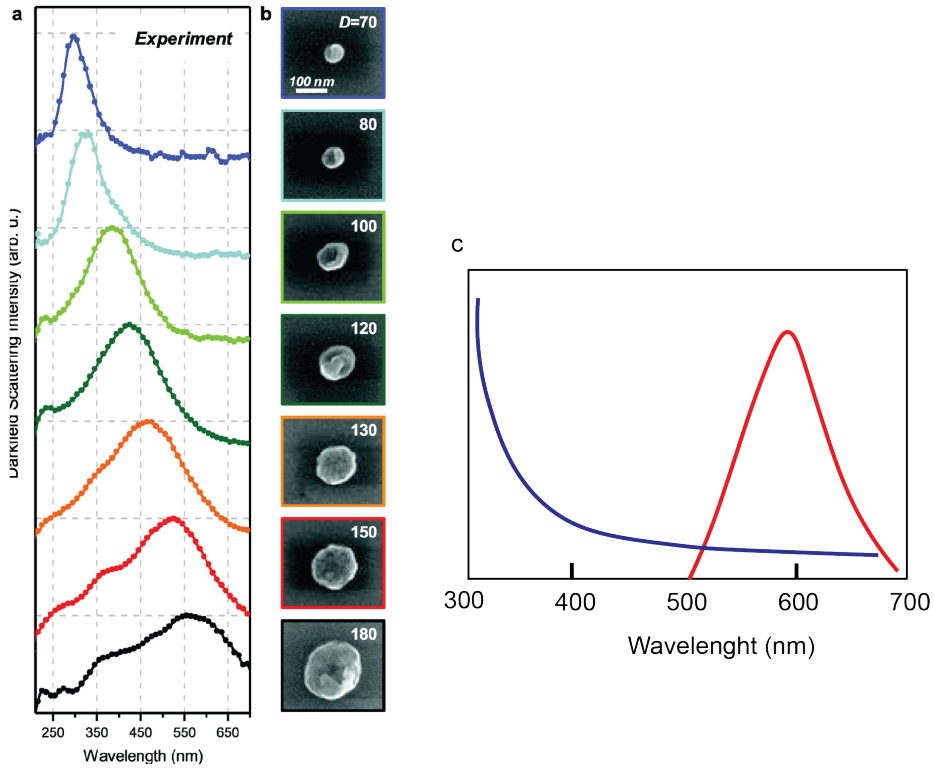

Figure 5.2: **Aluminum nanodisks and QD spectra.** a. Experimental dark-field scattering spectra of aluminum nanodisks. b. SEM images of the corresponding nanodisks. a and b are reproduced from Halas *et al* [144]. c. Absorption and emission spectra of InP/ZnS QD. Data is taken from NNCrystal USA.

Although the spectral design for this experiment is straightforward, single-QD imaging can be challenging. The points accumulation for imaging in nanoscale topography (PAINT) technique that we use in Chapter II does not work well with QDs due to the fact that QDs are much larger and heavier compared to organic dye molecules which

makes it difficult achieve the required binding and unbinding kinetics. Other common single-molecule techniques such as photoactivated localization microscopy (PALM) and stochastic optical reconstruction microscopy (STORM) are also impossible to apply to QDs as QDs are not photoswitchable. DNA-PAINT on the other hand, is a possible approach. DNA-PAINT is similar to PAINT technique except that it enables specific binding between the substrate and the target molecules by functionalizing the substrate with a single stranded oligo DNA(ssDNA) and the target molecules with a complementary strand [96]. Unlike the gold nanodisk experiment described in Chapter IV, the ssDNA used in DNA-PAINT is much shorter (<5 base pairs), so the hybridized dsDNA can also be unbound thermally. Therefore, this stochastic binding and unbinding behavior enables single-molecule imaging.

To attach ssDNA to QDs and aluminum nanodisks, one possible way is through 1-ethyl-3-(-3-dimethylaminopropyl) carbodiimide hydrochloride (EDC)-mediated crosslinking [147]. The process is described in Fig. 5.3. Firstly, the -COOH functionalized aluminum nanodisk is reacted with EDC to form an active O-acylisourea intermediate. This intermediate can then be easily displaced by an amino group modified ssDNA. Thus, the ssDNA-Al hybrid can be formed (Fig. 5.3a). The ssDNA-QD hybrid can be formed in the same fashion with -COOH functionalized QDs and the complementary ssDNAs (Fig. 5.3b). The amine modified ssDNAs are commercially available. Aluminum nanoparticles with carboxylic acid group functionalization has also been reported [148].

Just like in the PAINT experiment, under the epifluorescence setup, only when a ssDNA-QD links with the Al-ssDNA will its photoluminescence be captured by the detector. Other ssDNA-QDs diffusing in the solution will simply appear as out-of-focus signals (Fig. 5.3c).

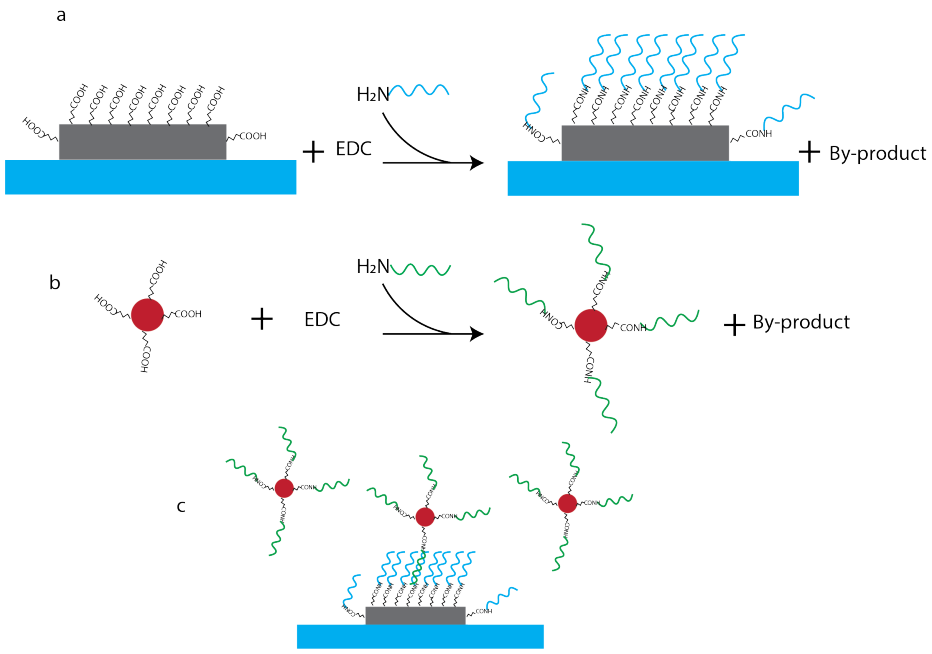

Figure 5.3: **DNA linking via EDC crosslinking.** a shows the process of linking a aluminum nanodisk with ssDNAs via EDC crosslinking. The grey slab is an aluminum nanodisk. The blue slab is a glass coverslip. The blue curly lines are ssDNAs. b shows the process of linking a QD with ssDNAs via EDC crosslinking. The red circle is a QD. The green curly lines are the complementary ssDNAs. c shows the situation when a QD binds to the aluminum nanodisk in the solution.

Challenges of this method include aligning the ultraviolet laser as it is not visible and the long photoluminescence time of QDs which reduces the rate of single-QD events on each nanodisk. Additionally, the relatively low transmittance of ultraviolet light when passing through optics also needs to be considered. Using aluminum nanoparticles for plasmonic applications also offers other advantages such as the facts that aluminum is low cost and highly abundant. This proposed method will push forward the development of plasmon enhanced super-resolution imaging.

BIBLIOGRAPHY

BIBLIOGRAPHY

[1] T. Zuo, H. Goldwyn, B. Isaacoff, D. Masiello, J. Biteen, "Rotation of Single-Molecule Emission Polarization by Plasmonic Nanorods", *Journal of Physical Chemistry Letters* **10** (2019).

[2] J. R. Lakowicz, *Principles of Fluorescence Spectroscopy Principles of Fluorescence Spectroscopy* (Springer, 2006), third ed.

[3] S. Kéna-Cohen, *Strong exciton-photon coupling in organic semiconductor microcavities* (Princeton University, 2010).

[4] M. Mandina, "Design, fabrication, and testing; sources and detectors; radiometry and photometry", *Handbook of Optics, M. Bass, Editor* (2009).

[5] J. R. Lakowicz, editor., *Fluorescence Anisotropy* (Springer US, Boston, MA, 2006), pp. 353–382.

[6] I. H. Van Stokkum, D. S. Larsen, R. Van Grondelle, "Global and target analysis of time-resolved spectra", *Biochimica et Biophysica Acta (BBA)-Bioenergetics* **1657**, 82 (2004).

[7] W. Lang, *Nomarski differential interference-contrast microscopy* (Carl Zeiss, 1982).

[8] G. Wang, W. Sun, Y. Luo, N. Fang, "Resolving rotational motions of nano-objects in engineered environments and live cells with gold nanorods and differential interference contrast microscopy", *Journal of the American Chemical Society* **132**, 16417 (2010).

[9] D. H. M. Dam, *et al.*, "Direct observation of nanoparticle–cancer cell nucleus interactions", *ACS nano* **6**, 3318 (2012).

[10] D. Brewster, A. D. Bache, *A Treatise on Optics...: First American Edition, with an Appendix, Containing an Elementary View of the Application of Analysis to Reflexion and Refraction* (Carey, Lea, & Blanchard, 1833).

[11] G. B. Airy, "On the diffraction of an object-glass with circular aperture", *Transactions of the Cambridge Philosophical Society* **5**, 283 (1835).

[12] H. H. Tuson, J. S. Biteen, "Unveiling the inner workings of live bacteria using super-resolution microscopy", *Analytical Chemistry* **87**, 42 (2015).

[13] E. J. Peterman, G. J. Wuite, *Single Molecule Analysis* (Springer, 2018).

[14] S. W. Paddock, *Confocal microscopy: methods and protocols*, vol. 122 (Springer Science & Business Media, 1999).

[15] M. Tokunaga, N. Imamoto, K. Sakata-Sogawa, "Highly inclined thin illumination enables clear single-molecule imaging in cells", *Nature methods* **5**, 159 (2008).

[16] K. König, "Multiphoton microscopy in life sciences", *Journal of microscopy* **200**, 83 (2000).

[17] P. A. Santi, "Light sheet fluorescence microscopy: a review", *Journal of Histochemistry & Cytochemistry* **59**, 129 (2011).

[18] R. M. Power, J. Huisken, "A guide to light-sheet fluorescence microscopy for multiscale imaging", *Nature methods* **14**, 360 (2017).

[19] A.-K. Gustavsson, P. N. Petrov, M. Y. Lee, Y. Shechtman, W. Moerner, "3d single-molecule super-resolution microscopy with a tilted light sheet", *Nature communications* **9**, 1 (2018).

[20] K. Xu, H. P. Babcock, X. Zhuang, "Dual-objective storm reveals three-dimensional filament organization in the actin cytoskeleton", *Nature methods* **9**, 185 (2012).

[21] P. D. Dahlberg, *et al.*, "Identification of pamkate as a red photoactivatable fluorescent protein for cryogenic super-resolution imaging", *Journal of the American Chemical Society* **140**, 12310 (2018).

[22] S. Weisenburger, B. Jing, A. Renn, V. Sandoghdar, *Nanoimaging and Nanospectroscopy* (International Society for Optics and Photonics, 2013), vol. 8815, p. 88150D.

[23] R. E. Thompson, D. R. Larson, W. W. Webb, "Precise nanometer localization analysis for individual fluorescent probes", *Biophysical Journal* **82**, 2775 (2002).

[24] S. R. P. Pavani, *et al.*, "Three-dimensional, single-molecule fluorescence imaging beyond the diffraction limit by using a double-helix point spread function", *Proceedings of the National Academy of Sciences* **106**, 2995 (2009).

[25] A. Sharonov, R. M. Hochstrasser, "Wide-field subdiffraction imaging by accumulated binding of diffusing probes", *Proceedings of the National Academy of Sciences* **103**, 18911 (2006).

[26] M. J. Rust, M. Bates, X. Zhuang, "Sub-diffraction-limit imaging by stochastic optical reconstruction microscopy (STORM)", *Nature Methods* **3**, 793 (2006).

[27] J. Vogelsang, T. Cordes, C. Forthmann, C. Steinhauer, P. Tinnefeid, "Controlling the fluorescence of ordinary oxazine dyes for single-molecule switching and superresolution microscopy", *Proceedings of the National Academy of Sciences of the United States of America* **106**, 8107 (2009).

[28] E. Betzig, *et al.*, "Imaging intracellular fluorescent proteins at nanometer resolution", *Science* **313**, 1642 (2006).

[29] S. T. Hess, T. P. Girirajan, M. D. Mason, "Ultra-high resolution imaging by fluorescence photoactivation localization microscopy", *Biophysical Journal* **91**, 4258 (2006).

[30] S. W. Hell, M. Kroug, "Ground-state-depletion fluorscence microscopy: A concept for breaking the diffraction resolution limit", *Applied Physics B* **60**, 495 (1995).

[31] T. Dertinger, R. Colyer, G. Iyer, S. Weiss, J. Enderlein, "Fast, background-free, 3D super-resolution optical fluctuation imaging (SOFI)", *Proceedings of the National Academy of Sciences* **106**, 22287 (2009).

[32] P. Bharadwaj, B. Deutsch, L. Novotny, "Optical Antennas", *Advances in Optics and Photonics* **1**, 438 (2009).

[33] J. N. Anker, *et al.*, "Biosensing with plasmonic nanosensors", *Nature Materials* **7**, 442 (2008).

[34] L. Novotny, N. Van Hulst, "Antennas for light", *Nature Photonics* **5**, 83 (2011).

[35] M. Agio, "Optical antennas as nanoscale resonators", *Nanoscale* **4**, 692 (2012).

[36] J. Alda, J. M. Rico-García, J. M. López-Alonso, G. Boreman, "Optical antennas for nano-photonic applications", *Nanotechnology* **16**, S230 (2005).

[37] M. I. Stockman, "Nanoplasmonics: past, present, and glimpse into future", *Optics Express* **19**, 22029 (2011).

[38] K. A. Willets, R. P. Van Duyne, "Localized Surface Plasmon Resonance Spectroscopy and Sensing", *Annual Review of Physical Chemistry* **58**, 267 (2007).

[39] X. Fan, W. Zheng, D. J. Singh, "Light scattering and surface plasmons on small spherical particles", *Light: Science & Applications* **3**, e179 (2014).

[40] M. Pelton, J. Aizpurua, G. Bryant, "Metal-nanoparticle plasmonics", *Laser and Photonics Reviews* **2**, 136 (2008).

[41] H. Yuan, S. Khatua, P. Zijlstra, M. Yorulmaz, M. Orrit, "Thousand-fold enhancement of single-molecule fluorescence near a single gold nanorod", *Angewandte Chemie - International Edition* **52**, 1217 (2013).

[42] G. M. Akselrod, *et al.*, "Probing the mechanisms of large Purcell enhancement in plasmonic nanoantennas", *Nature Photonics* **8**, 835 (2014).

[43] K. A. Willets, A. J. Wilson, V. Sundaresan, P. B. Joshi, "Super-Resolution Imaging and Plasmonics", *Chemical Reviews* **117**, 7538 (2017).

[44] J. D. Jackson, *Classical electrodynamics* (John Wiley & Sons, 2007).

[45] M. Fox, *Optical Properties of Solids* (Oxford University Press, 2010), second ed.

[46] S. A. Maier, "Plasmonic field enhancement and SERS in the effective mode volume picture", *Optics Express* **14**, 1957 (2006).

[47] S. A. Maier, *Plasmonics: Fundamentals and applications* (Springer US, Boston, MA, 2007).

[48] S. Lal, S. Link, N. J. Halas, "Nano-optics from sensing to waveguiding", *Nature Photonics* **1**, 641 (2007).

[49] S. Khatua, M. Orrit, "Probing, sensing, and fluorescence enhancement with single gold nanorods", *Journal of Physical Chemistry Letters* **5**, 3000 (2014).

[50] K. M. Mayer, J. H. Hafner, "Localized surface plasmon resonance sensors", *Chemical Reviews* **111**, 3828 (2011).

[51] A. B. Taylor, P. Zijlstra, "Single-Molecule Plasmon Sensing: Current Status and Future Prospects", *ACS Sensors* **2**, 1103 (2017).

[52] G. Doria, *et al.*, "Noble metal nanoparticles for biosensing applications", *Sensors* **12**, 1657 (2012).

[53] E. Ozbay, "Plasmonics: merging photonics and electronics at nanoscale dimensions", *Science* **311**, 189 (2006).

[54] A. G. Brolo, "Plasmonics for future biosensors", *Nature Photonics* **6**, 709 (2012).

[55] S. Nie, S. R. Emory, "Probing single molecules and single nanoparticles by surface-enhanced raman scattering", *Science* **275**, 1102 (1997).

[56] D. Cialla, *et al.*, "Surface-enhanced raman spectroscopy (sers): progress and trends", *Analytical and bioanalytical chemistry* **403**, 27 (2012).

[57] J. Biteen, K. A. Willets, "Introduction: Super-Resolution and Single-Molecule Imaging", *Chemical Reviews* **117**, 7241 (2017).

[58] A. Kinkhabwala, *et al.*, "Large single-molecule fluorescence enhancements produced by a bowtie nanoantenna", *Nature Photonics* **3**, 654 (2009).

[59] P. Bharadwaj, L. Novotny, "Spectral dependence of single molecule fluorescence enhancement", *Optics Express* **15**, 14266 (2007).

[60] M. Ringler, *et al.*, "Shaping emission spectra of fluorescent molecules with single plasmonic nanoresonators", *Physical Review Letters* **100**, 203002 (2008).

[61] C. Ayala-Orozco, *et al.*, "Fluorescence Enhancement of Molecules Inside a Gold Nanomatryoshka", *Nano Letters* **14**, 2926 (2014).

[62] M. Pelton, "Modified spontaneous emission in nanophotonic structures", *Nature Photonics* **9**, 427 (2015).

[63] P. Anger, P. Bharadwaj, L. Novotny, "Enhancement and quenching of single-molecule fluorescence", *Physical Review Letters* **96**, 113002 (2006).

[64] R. C. Boutelle, D. Neuhauser, S. Weiss, "Far-Field Super-resolution Detection of Plasmonic Near-Fields", *ACS Nano* **10**, 7955 (2016).

[65] C. Ropp, *et al.*, "Nanoscale probing of image-dipole interactions in a metallic nanostructure", *Nature Communications* **6**, 6558 (2015).

[66] R. J. Moerland, T. H. Taminiau, L. Novotny, N. F. Van Hulst, L. Kuipers, "Reversible polarization control of single photon emission", *Nano letters* **8**, 606 (2008).

[67] T. H. Taminiau, F. D. Stefani, N. F. van Hulst, "Enhanced directional excitation and emission of single emitters by a nano-optical yagi-uda antenna", *Optics express* **16**, 10858 (2008).

[68] T. Taminiau, F. Stefani, F. B. Segerink, N. Van Hulst, "Optical antennas direct single-molecule emission", *Nature photonics* **2**, 234 (2008).

[69] T. Shegai, *et al.*, "Managing light polarization via plasmon–molecule interactions within an asymmetric metal nanoparticle trimer", *Proceedings of the National Academy of Sciences* **105**, 16448 (2008).

[70] A. G. Curto, *et al.*, "Unidirectional emission of a quantum dot coupled to a nanoantenna", *Science* **329**, 930 (2010).

[71] M. Ren, *et al.*, "Linearly polarized light emission from quantum dots with plasmonic nanoantenna arrays", *Nano letters* **15**, 2951 (2015).

[72] E. A. Wertz, B. P. Isaacoff, J. S. Biteen, "Wavelength-Dependent Super-resolution Images of Dye Molecules Coupled to Plasmonic Nanotriangles", *ACS Photonics* **3**, 1733 (2016).

[73] H. J. Goldwyn, K. C. Smith, J. A. Busche, D. J. Masiello, "Mislocalization in plasmon-enhanced single-molecule fluorescence microscopy as a dynamical young's interferometer", *ACS Photonics* **5**, 3141 (2018).

[74] S. Khatua, *et al.*, "Resonant plasmonic enhancement of single-molecule fluorescence by individual gold nanorods", *ACS Nano* **8**, 4440 (2014).

[75] D. L. Mack, *et al.*, "Decoupling absorption and emission processes in super-resolution localization of emitters in a plasmonic hotspot", *Nature Communications* **8**, 14513 (2017).

[76] B. Fu, B. P. Isaacoff, J. S. Biteen, "Super-Resolving the Actual Position of Single Fluorescent Molecules Coupled to a Plasmonic Nanoantenna", *ACS Nano* **11**, 8978 (2017).

[77] B. Fu, J. D. Flynn, B. P. Isaacoff, D. J. Rowland, J. S. Biteen, "Super-Resolving the Distance-Dependent Plasmon-Enhanced Fluorescence of Single Dye and Fluorescent Protein Molecules", *Journal of Physical Chemistry C* **119**, 19350 (2015).

[78] B. P. Isaacoff, Y. Li, S. A. Lee, J. S. Biteen, "Small-labs: Measuring single-molecule intensity and position in obscuring backgrounds", *Biophysical Journal* **116**, 975 (2019).

[79] C. Sönnichsen, B. M. Reinhard, J. Liphardt, A. P. Alivisatos, "A molecular ruler based on plasmon coupling of single gold and silver nanoparticles", *Nature Biotechnology* **23**, 741 (2005).

[80] C. Sönnichsen, *et al.*, "Drastic reduction of plasmon damping in gold nanorods", *Physical Review Letters* **88**, 077402 (2002).

[81] Y. Fang, *et al.*, "Plasmon emission quantum yield of single gold nanorods as a function of aspect ratio", *Acs Nano* **6**, 7177 (2012).

[82] Y.-Y. Cai, *et al.*, "Photoluminescence of gold nanorods: Purcell effect enhanced emission from hot carriers", *Acs Nano* **12**, 976 (2018).

[83] L. Novotny, B. Hecht, *Principles of nano-optics*, vol. 9781107005 (Cambridge University Press, 2009).

[84] C. F. Bohren, D. R. Huffman, *Absorption and scattering of light by small particles* (John Wiley & Sons, 2008).

[85] P. B. Johnson, R.-W. Christy, "Optical constants of the noble metals", *Physical Review B* **6**, 4370 (1972).

[86] U. Hohenester, A. Trügler, "Mnpbem–a matlab toolbox for the simulation of plasmonic nanoparticles", *Computer Physics Communications* **183**, 370 (2012).

[87] E. Wolf, "Electromagnetic diffraction in optical systems-i. an integral representation of the image field", *Proceedings of the Royal Society of London. Series A. Mathematical and Physical Sciences* **253**, 349 (1959).

[88] V. Dhayalan, J. J. Stamnes, "Focusing of electric-dipole waves in the debye and kirchhoff approximations", *Pure and Applied Optics: Journal of the European Optical Society Part A* **6**, 347 (1997).

[89] T. X. Hoang, Y. Duan, X. Chen, G. Barbastathis, "Focusing and imaging in microsphere-based microscopy", *Optics Express* **23**, 12337 (2015).

[90] C. W. Heaps, G. C. Schatz, "Modeling super-resolution sers using a t-matrix method to elucidate molecule-nanoparticle coupling and the origins of localization errors", *The Journal of Chemical Physics* **146**, 224201 (2017).

[91] S. A. Lee, J. S. Biteen, "Interplay of Nanoparticle Resonance Frequency and Array Surface Coverage in Live-Cell Plasmon-Enhanced Single-Molecule Imaging", *The Journal of Physical Chemistry C* **122**, 5705 (2018).

[92] C. Steuwe, *et al.*, "Visualizing electromagnetic fields at the nanoscale by single molecule localization", *Nano Letters* **15**, 3217 (2015).

[93] E. C. Cho, Q. Zhang, Y. Xia, "The effect of sedimentation and diffusion on cellular uptake of gold nanoparticles", *Nature Nanotechnology* **6**, 385 (2011).

[94] M. A. Thompson, M. D. Lew, W. Moerner, "Extending Microscopic Resolution with Single-Molecule Imaging and Active Control", *Annual Review of Biophysics* **41**, 321 (2012).

[95] K. Lim, *et al.*, "Nanostructure-Induced Distortion in Single-Emitter Microscopy", *Nano Letters* **16**, 5415 (2016).

[96] M. Raab, C. Vietz, F. D. Stefani, G. P. Acuna, P. Tinnefeld, "Shifting molecular localization by plasmonic coupling in a single-molecule mirage", *Nature Communications* **8**, 13966 (2017).

[97] K. L. Blythe, K. A. Willets, "Super-resolution imaging of fluorophore-labeled dna bound to gold nanoparticles: a single-molecule, single-particle approach", *The Journal of Physical Chemistry C* **120**, 803 (2016).

[98] R. Baiyasi, *et al.*, "Psf distortion in dye–plasmonic nanomaterial interactions: Friend or foe?", *Acs Photonics* **6**, 699 (2019).

[99] G. Blanquer, *et al.*, "Relocating single-molecules in super-resolved fluorescence lifetime images near a plasmonic nanostructure", *ACS Photonics* (2020).

[100] K. L. Blythe, E. J. Titus, K. A. Willets, "Comparing the Accuracy of Reconstructed Image Size in Super-Resolution Imaging of Fluorophore-Labeled Gold Nanorods Using Different Fit Models", *The Journal of Physical Chemistry C* **119**, 19333 (2015).

[101] N. Kongsuwan, *et al.*, "Suppressed quenching and strong-coupling of purcell-enhanced single-molecule emission in plasmonic nanocavities", *Acs Photonics* **5**, 186 (2018).

[102] A. Taylor, R. Verhoef, M. Beuwer, Y. Wang, P. Zijlstra, "All-Optical Imaging of Gold Nanoparticle Geometry Using Super-Resolution Microscopy", *The Journal of Physical Chemistry C* **122**, 2336 (2018).

[103] R. Chikkaraddy, *et al.*, "Mapping nanoscale hotspots with single-molecule emitters assembled into plasmonic nanocavities using dna origami", *Nano letters* **18**, 405 (2018).

[104] R. Chikkaraddy, *et al.*, "Single-molecule strong coupling at room temperature in plasmonic nanocavities", *Nature* **535**, 127 (2016).

[105] S. Van De Linde, *et al.*, "Direct stochastic optical reconstruction microscopy with standard fluorescent probes", *Nature Protocols* **6**, 991 (2011).

[106] I. Lieberman, G. Shemer, T. Fried, E. M. Kosower, G. Markovich, "Plasmon-resonance-enhanced absorption and circular dichroism", *Angewandte Chemie International Edition* **47**, 4855 (2008).

[107] A. Gaiduk, M. Yorulmaz, M. Orrit, "Correlated absorption and photoluminescence of single gold nanoparticles", *ChemPhysChem* **12**, 1536 (2011).

[108] M. A. van Dijk, *et al.*, "Absorption and scattering microscopy of single metal nanoparticles", *Physical Chemistry Chemical Physics* **8**, 3486 (2006).

[109] M. Yorulmaz, *et al.*, "Single-particle absorption spectroscopy by photothermal contrast", *Nano Letters* **15**, 3041 (2015).

[110] S. Link, M. A. El-Sayed, "Shape and size dependence of radiative, non-radiative and photothermal properties of gold nanocrystals", *International Reviews in Physical Chemistry* **19**, 409 (2000).

[111] S. J. Hurst, A. K. Lytton-Jean, C. A. Mirkin, "Maximizing DNA loading on a range of gold nanoparticle sizes", *Analytical Chemistry* **78**, 8313 (2006).

[112] J.-H. Oh, D. H. Park, J. H. Joo, J.-S. Lee, "Recent advances in chemical functionalization of nanoparticles with biomolecules for analytical applications", *Analytical and Bioanalytical Chemistry* **407**, 8627 (2015).

[113] M. Heilemann, S. van de Linde, A. Mukherjee, M. Sauer, "Super-Resolution Imaging with Small Organic Fluorophores", *Angewandte Chemie International Edition* **48**, 6903 (2009).

[114] M. Heilemann, *et al.*, "Subdiffraction-Resolution Fluorescence Imaging with Conventional Fluorescent Probes", *Angewandte Chemie International Edition* **47**, 6172 (2008).

[115] A. P. Alivisatos, W. Gu, C. Larabell, "Quantum dots as cellular probes", *Annual Review of Biomedical Engineering* **7**, 55 (2005).

[116] V. V. Pinto, *et al.*, "Long time effect on the stability of silver nanoparticles in aqueous medium: effect of the synthesis and storage conditions", *Colloids and Surfaces A: Physicochemical and Engineering Aspects* **364**, 19 (2010).

[117] K. Chatterjee, S. Banerjee, D. Chakravorty, "Plasmon resonance shifts in oxide-coated silver nanoparticles", *Physical Review B* **66**, 085421 (2002).

[118] Y. Han, *et al.*, "Effect of oxidation on surface-enhanced raman scattering activity of silver nanoparticles: a quantitative correlation", *Analytical Chemistry* **83**, 5873 (2011).

[119] N. Grillet, *et al.*, "Photo-oxidation of individual silver nanoparticles: a real-time tracking of optical and morphological changes", *The Journal of Physical Chemistry C* **117**, 2274 (2013).

[120] L. Kvítek, *et al.*, "Effect of surfactants and polymers on stability and antibacterial activity of silver nanoparticles (nps)", *The Journal of Physical Chemistry C* **112**, 5825 (2008).

[121] A. Ashkarran, M. Ahadian, M. H. Nezhad, *et al.*, "Stability, size and optical properties of colloidal silver nanoparticles prepared by electrical arc discharge in water", *The European Physical Journal-Applied Physics* **48** (2009).

[122] H. Baida, *et al.*, "Quantitative determination of the size dependence of surface plasmon resonance damping in single Ag@SiO_2 nanoparticles", *Nano Letters* **9**, 3463 (2009).

[123] X. Li, *et al.*, "Silver nanoparticles protected by monolayer graphene as a stabilized substrate for surface enhanced raman spectroscopy", *Carbon* **66**, 713 (2014).

[124] B. Huang, H. Babcock, X. Zhuang, "Breaking the diffraction barrier: super-resolution imaging of cells", *Cell* **143**, 1047 (2010).

[125] M. Fernández-Suárez, A. Y. Ting, "Fluorescent probes for super-resolution imaging in living cells", *Nature Reviews Molecular Cell Biology* **9**, 929 (2008).

[126] K. A. Lidke, B. Rieger, T. M. Jovin, R. Heintzmann, "Superresolution by localization of quantum dots using blinking statistics", *Optics Express* **13**, 7052 (2005).

[127] P. Hoyer, T. Staudt, J. Engelhardt, S. W. Hell, "Quantum dot blueing and blinking enables fluorescence nanoscopy", *Nano Letters* **11**, 245 (2011).

[128] X. Yang, *et al.*, "Versatile application of fluorescent quantum dot labels in super-resolution fluorescence microscopy", *ACS Photonics* **3**, 1611 (2016).

[129] H. Chen, H. Gai, E. S. Yeung, "Inhibition of photobleaching and blue shift in quantum dots", *Chemical Communications* pp. 1676–1678 (2009).

[130] X. Shi, *et al.*, "Observing photophysical properties of quantum dots in air at the single molecule level: advantages in microarray applications", *Lab on a Chip* **10**, 2844 (2010).

[131] W. G. van Sark, P. L. Frederix, A. A. Bol, H. C. Gerritsen, A. Meijerink, "Blueing, bleaching, and blinking of single CdSe/ZnS quantum dots", *ChemPhysChem* **3**, 871 (2002).

[132] M. Nirmal, *et al.*, "Fluorescence intermittency in single cadmium selenide nanocrystals", *Nature* **383**, 802 (1996).

[133] W. G. Van Sark, *et al.*, "Photooxidation and photobleaching of single cdse/zns quantum dots probed by room-temperature time-resolved spectroscopy", *The Journal of Physical Chemistry B* **105**, 8281 (2001).

[134] W. E. Moerner, M. Orrit, "Illuminating single molecules in condensed matter", *Science* **283**, 1670 (1999).

[135] M. Hu, *et al.*, "Ultrasensitive, multiplexed detection of cancer biomarkers directly in serum by using a quantum dot-based microfluidic protein chip", *ACS nano* **4**, 488 (2010).

[136] A. R. Yadav, R. Sriram, J. A. Carter, B. L. Miller, "Comparative study of solution–phase and vapor–phase deposition of aminosilanes on silicon dioxide surfaces", *Materials Science and Engineering: C* **35**, 283 (2014).

[137] S. A. Lee, J. S. Biteen, "Spectral reshaping of single dye molecules coupled to single plasmonic nanoparticles", *The Journal of Physical Chemistry Letters* **10**, 5764 (2019).

[138] H. Chen, H. Gai, E. S. Yeung, "Inhibition of photobleaching and blue shift in quantum dots", *Chemical Communications* pp. 1676–1678 (2009).

[139] K. Pechstedt, T. Whittle, J. Baumberg, T. Melvin, "Photoluminescence of colloidal CdSe/ZnS quantum dots: The critical effect of water molecules", *Journal of Physical Chemistry C* **114**, 12069 (2010).

[140] M. P. Nicholas, L. Rao, A. Gennerich, *Covalent immobilization of microtubules on glass surfaces for molecular motor force measurements and other single-molecule assays* (Springer, 2014).

[141] S. D. Chandradoss, *et al.*, "Surface passivation for single-molecule protein studies", *Journal of Visualized Experiments* p. e50549 (2014).

[142] P. Beauregard, "Making Slides Hydrophobic and Dust Repellent", https://laboratoryresource.com/?navaction=getitemid=66, (Accessed: 2020-04-04).

[143] L. Kringle, *et al.*, "Temperature-dependent conformations of exciton-coupled cy3 dimers in double-stranded dna", *The Journal of Chemical Physics* **148**, 085101 (2018).

[144] B. Y. Zheng, Y. Wang, P. Nordlander, N. J. Halas, "Color-selective and cmos-compatible photodetection based on aluminum plasmonics", *Advanced Materials* **26**, 6318 (2014).

[145] A. Ono, M. Kikawada, R. Akimoto, W. Inami, Y. Kawata, "Fluorescence enhancement with deep-ultraviolet surface plasmon excitation", *Optics Express* **21**, 17447 (2013).

[146] I. Zoric, M. Zach, B. Kasemo, C. Langhammer, "Gold, platinum, and aluminum nanodisk plasmons: material independence, subradiance, and damping mechanisms", *ACS Nano* **5**, 2535 (2011).

[147] G. T. Hermanson, *Bioconjugate techniques* (Academic press, 2013).

[148] W. Al-Shatty, A. M. Lord, S. Alexander, A. R. Barron, "Tunable surface properties of aluminum oxide nanoparticles from highly hydrophobic to highly hydrophilic", *ACS Omega* **2**, 2507 (2017).